LRP 795/04 August 2004

Papers presented at the
31st EPS CONFERENCE ON PLASMA PHYSICS

Imperial College, London, U.K.
June-July 2004

Available in colour on the web at
crppwww.epfl.ch/archives

ISSN 0458-5895

LIST OF CONTENTS Page

Page

First principles based simulations of instabilities and turbulence

L Villard[1], P Angelino[1], A Bottino[1], S J Allfrey[1], R Hatzky[2], Y Idomura[3], O Sauter[1], and T M Tran[1]

[1] Centre de Recherches en Physique des Plasmas, Ecole Polytechnique Fédérale de Lausanne, Association Euratom-Suisse, Lausanne, Switzerland
[2] Rechenzentrum der Max-Planck Gesellschaft, Garching, Germany
[3] Japan Atomic Energy Research Institute, Naka, Japan

E-mail: laurent.villard@epfl.ch

PACS numbers: 52.30.Gz, 52.35.Qz, 52.35.Mw, 52.35.Ra

Abstract. It is now widely believed that low frequency turbulence developing from small scale instabilities is responsible for the phenomenon of anomalous transport generally observed in magnetic confinement fusion experiments. The micro-instabilities are driven by gradients of equilibrium density, ion and electron temperatures and magnetic field strength. Gyrokinetic theory is based on the Vlasov-Maxwell equations and, consistent with the ordering, averages out the fast particle gyromotion, reducing the phase space from 6 to 5 dimensions. Solving the resulting equations is a nontrivial task. Difficulties are associated with the magnetic confinement geometry, the strong disparities in space and time scales perpendicular and parallel to $\mathbf{B}$, the different time scales of ion and electron dynamics, and the complex nonlinear behaviour of the system. The main numerical methods are briefly presented together with some recent developments and improvements to the basic algorithms. Recent results are shown, with emphasis on the roles of zonal $E \times B$ flows, of parallel nonlinearity and of toroidal coupling on the saturation of ion temperature gradient (ITG) driven turbulence in tokamaks.

1. Introduction

Instabilities and turbulence are ubiquitous phenomena in plasmas. There is great interest in these phenomena, especially in the context of magnetic confinement fusion research, which has lasted for several decades and is still growing. The understanding of anomalous transport has greatly improved over the past years, thanks in good part to the role of large scale numerical simulations [1]-[16]. Predictions used for the design of the next generation of experimental fusion reactors have been largely made on extrapolations from a range of existing experiments worldwide and assumed semi-empirical scaling laws. However, a full comprehension of the basic physical processes underlying the confinement properties is still missing.

First principles based simulations of instabilities and turbulence

Instabilities can be divided into two types: the *macro*-instabilities, defined as MHD instabilities developing on a length scale comparable to the device size, and the *micro*-instabilities, which have a typical scale of the same order as the Larmor radius. Computational tools for MHD problems in tokamak (axisymmetric) geometry were developed more than 20 years ago and have been extremely useful in determining the operational limits in tokamaks. More sophisticated numerical tools are still being developed to tackle more difficult problems. Examples are: the instabilities in the presence of a magnetic separatrix [17]; the role of internal modes as triggers of sawtooth relaxations [18]; stability analysis and bootstrap current optimisation for more exotic shapes (low aspect ratio [19], fully 3D configurations [20]); and the linear and nonlinear threshold of Neoclassical Tearing Modes [21]. Also, an important class of modes has been shown to be destabilised in the presence of a fast (non thermal) ion population: the Alfvén Eigenmodes (AE), and in particular its toroidicity induced branch [22]-[25].

The present paper focuses on micro-instabilities and their nonlinear evolution. Equilibrium gradients of temperature, density or magnetic field strength are the driving source of these instabilities. Unstable modes lead to a nonlinear state with a finite fluctuation amplitude. This is accompanied by the generation of an anomalous heat and/or particle flux across magnetic field lines, typically much larger than the transport calculated from collisional behaviour (classical or neoclassical). Theory has focused in particular on low frequency modes (as compared to the cyclotron frequency of plasma species). Among the different types of micro-instabilities, the Ion Temperature Gradient mode (ITG) [26] has received particular attention. The computed growth rates, γ, and perpendicular wavenumbers, $k_\perp$, are such that a mixing length estimate of the diffusion coefficient, $\gamma/k_\perp^2$, typically gives values that are comparable to those needed to explain various confinement experiments. ITG modes (and other modes such as the Trapped Electron Mode, TEM [27], and the Electron Temperature Gradient mode, ETG [28, 29]) have a finite temperature gradient length threshold, above which the growth rate is seen to increase strongly: thus the system tends to react to an increased input power by only a slight increase in the temperature gradient while the heat flux is strongly increased. This is (at least qualitatively) in agreement with the degradation of confinement time with input power and the profile stiffness observed in many experiments. The low frequency character of the fluctuations under study is at the basis of the *gyrokinetic* ordering, in which the Vlasov-Maxwell equations are averaged over the particle gyromotion, thus reducing the phase space of the distribution function from 6 to 5 dimensions.

Linear behaviour alone is not enough to understand the many physical mechanisms involved. Research in the past decade has focused on the processes responsible for the saturation of fluctuations to a finite amplitude. In particular, the observation of "transport barriers" [30], regions in which the anomalous transport is substantially reduced, has stimulated the investigations. Three main nonlinear mechanisms have been invoked.

First, the interaction of sheared flows and in particular *zonal* $E \times B$ flows with turbulence. Zonal $E \times B$ flows are axisymmetric and poloidally symmetric potential

peturbations and their $E \times B$ drift velocity is purely within a magnetic surface. They are linearly neither stable nor unstable (at least in the collisionless limit). In toroidal geometry they may be partly damped because of their coupling to $m \neq 0$ poloidal components, but there remains a totally undamped component. It has been shown in several simulations [1, 3, 5, 6, 9] that turbulence nonlinearly generates zonal flows, and that in turn the zonal flows reduce the unstable mode amplitudes by shearing the turbulent eddies. Thus, the system appears to be self regulated, with the zonal flows playing the role of "organiser" of the turbulence. The resulting heat flux is reduced as compared to the case when the zonal component is artificially supressed. Models based on the coupling of turbulence to sheared flows have been proposed [31] to explain the transition from low to high confinement regimes (L-mode to H-mode transition) in the edge region of tokamaks.

Second, intermittency in fluctuations has been observed in some simulations based on fluid [32]-[37] or collisional gyrokinetic models [38]. This *self-organized bursty transport* is thought to characterise some regimes of nondiffusive turbulent behaviour. In the context of electron scale instabilities (ETG modes), the linear mixing length estimate for anomalous diffusion is far too low to explain the measured electron transport, essentially because of the very large $k_\perp$ of ETG modes. Nonlinear gyrokinetic flux-tube simulations [10] have shown the appearance of intermittent, radially elongated structures, called *streamers*, that drive (on a time average) much larger fluxes than can be inferred from the linear mixing length estimate. In other simulations, based on a fluid description and a prescribed edge heat flux (as opposed to flux-tube radial periodic boundary conditions), ETG fluctuations do not create the same high level of anomalous heat flux [12]. More investigations are needed in order to resolve this discrepancy. In recent gyrofluid ETG simulations [13] it was shown that zonal flows may be enhanced in weak magnetic shear regions thus leading to an enhanced electron confinement regime.

Third, the mechanism of *turbulence spreading* has been invoked to explain the saturation of turbulence [39]-[41]. Already noted in early nonlinear fluid models [42], turbulence is seen propagating radially beyond the region of linear instability. A model equation has been proposed [39] that describes how the turbulence radial spreading into the linearly stable zone reduces the turbulence intensity in the linearly unstable zone and introduces an additional dependence on the $\rho* = \rho/a$ transport scaling, in broad agreement with toroidal nonlinear gyrokinetic simulations [40]. Saturation occurs when the radial flux of fluctuation energy from the linearly unstable region is balanced by local dissipation in the linearly stable region. In Ref [42], two distinct mechanisms for radial propagation of turbulence are evident: toroidal coupling, acting through convection, and non-linear effects, inducing diffusion. In Ref [41] a model is described in which different drift wave couplings are mediated by zonal flows. In that model, the drift wave radial dispersive properties, which are affected by the toroidal geometry, are an essential feature: the authors expect that turbulence in a torus is qualitatively different from that in a cylinder.

While the above mentioned models are extremely useful in getting insight to the

physics involved in the nonlinear turbulent processes, it is also clear that a more quantitative and detailed description, based on first principles, is desirable. The task can be formulated in the most simple terms as directly solving the Maxwell-Vlasov system of equations (in the gyrokinetic limit). "Direct" means here that the first principles that the original system of equations satisfy should be maintained in their numerically discretised version. For example, the particle and energy conservation principles should be reflected in the solution as accurately as possible. Clearly, numerical methods are a necessity. The past decade has seen several major developments in this area [1]-[16]. Such large scale simulations have already given important physical results. To cite only a few: the importance of the zonal flows in determining the ITG turbulence level and the corresponding anomalous heat flux [9]; the Shafranov shift stabilisation of trapped electron modes in the core of tokamak discharges with internal transport barriers [43]; the scaling of anomalous heat diffusivity with system size [1]; the importance of considering equilibrium distribution functions of the true constants of motion in order to avoid the spurious excitation of geodesic acoustic modes [5, 44]; the importance of retaining the parallel nonlinearity for a correct zonal flow determination [6]; detailed comparisons with specific tokamak experiments have been made, e.g. with DIII-D [45] and Asdex-Upgrade [46]; the inclusion of non-adiabatic electron response and electromagnetic pertubations in linear [47] and nonlinear [2] global codes; the inclusion of realistic ideal MHD equilibrium geometry and truly global profiles in tokamak [50, 46, 6], and fully 3D stellarator geometry [51, 52] - the latter limited to electrostatic, linear perturbations.

The remainder of the paper is organised as follows. In Section 2, the basic features of the gyrokinetic model are introduced, and some of its important variants are mentioned, especially regarding the model used for the electron response. In Section 3, the main approaches to the problem are described in brief: Lagrangian versus Eulerian or semi-Lagrangian, global versus local, frozen gradients versus fixed edge flux and free profile evolution. In Section 4, we present global gyrokinetic collisionless simulations that are focused on the analysis of the roles of zonal $E \times B$ flows, toroidal geometry, and parallel nonlinearity in the development of ITG turbulence in tokamak plasmas. Section 5 presents the main conclusions and discusses possible future work.

2. Gyrokinetic model and its variations

We consider a neutral magnetized plasma in a symmetric configuration consisting of nested magnetic surfaces labeled by the variable ψ:

$$\mathbf{B} = F(\psi)\nabla\varphi + \nabla\psi \times \nabla\varphi \tag{1}$$

in which $F(\psi)$ is the poloidal current flux function, φ is the toroidal angle and ψ is the poloidal magnetic flux divided by 2π, solution of the Grad-Shafranov ideal MHD equilibrium equation [53]. We define the equilibrium scale length of an equilibrium quantity Q as $L_Q = |Q|/|\nabla Q|$. Equilibrium electric fields normal to the magnetic

surfaces, $\mathbf{E} = -\nabla\Phi_0(\psi)$, can be added to the description. Noting the cyclotron frequency of plasma species Ω_s and their Larmor radius ρ_{Ls}, we consider low frequency perturbations $\delta\phi$ with the following *gyro*-ordering in a small parameter ϵ_g:

$$\omega/\Omega_i \sim k_\parallel/k_\perp \sim e\delta\phi/k_B T_e \sim \rho_{Li}/L_n \sim \rho_{Li}/L_{Ti} \sim \epsilon_g \ , \tag{2}$$

where $k_\parallel$ and $k_\perp$ are the components of the wavevector in the directions parallel and perpendicular to the magnetic field $\mathbf{B}$. The inhomogeneity of the equilibrium magnetic field is described by another small parameter $\epsilon_B \sim \rho_{Li}/L_B$. The gyrokinetic ordering removes the fast cyclotron timescale and through averaging over the gyroangle reduces the phase space dimension from 6 to 5 [54] - [57]. The gyrocentre distribution function of species s is $f_s(\mathbf{R}, v_\parallel, \mu)$ with $\mathbf{R}$ the gyrocentre spatial coordinates, $v_\parallel$ the parallel component of the velocity and $\mu = m_s v_\perp^2/2B$ the magnetic moment. In collisionless systems we have

$$f_s = \text{const along characteristics} \tag{3}$$

which are solutions of the following evolution equations of motion

$$\frac{\mathrm{d}\mu}{\mathrm{d}t} = 0 \tag{4}$$

$$\frac{\mathrm{d}\mathbf{R}}{\mathrm{d}t} = \frac{\mathrm{d}\mathbf{R}}{\mathrm{d}t}\Big|_\parallel + \frac{\mathrm{d}\mathbf{R}}{\mathrm{d}t}\Big|_{\nabla B} + \frac{\mathrm{d}\mathbf{R}}{\mathrm{d}t}\Big|_E + \frac{\mathrm{d}\mathbf{R}}{\mathrm{d}t}\Big|_{\delta E} \tag{5}$$

$$\frac{\mathrm{d}v_\parallel}{\mathrm{d}t} = \frac{\mathrm{d}v_\parallel}{\mathrm{d}t}\Big|_{\nabla B} + \frac{\mathrm{d}v_\parallel}{\mathrm{d}t}\Big|_E + \frac{\mathrm{d}v_\parallel}{\mathrm{d}t}\Big|_{\delta E} \tag{6}$$

Explicit expressions for the terms appearing on the right hand side can be found in Ref.[57]. The subscripts $\parallel$, ∇B, E and δE denote parallel motion, perpendicular magnetic drifts, equilibrium $E \times B$ drifts and perturbed $\delta E \times B$ drifts, respectively. Due to the gyrokinetic ordering, the parallel time derivative is larger than the other terms. This is the origin of the strong anisotropy of the system of perturbations, which tend to form structures aligned with the equilibrium magnetic field lines. This strong anisotropy, and the associated separation of parallel and perpendicular time scales, are essential features of microinstabilities and turbulence in this frequency range. The system of equations is completed by Poisson's equation for $\delta\phi$, which reduces to the quasi-neutrality equation

$$\delta n_e - \delta n_{i,pol} = \langle \delta n_i \rangle \tag{7}$$

where $\delta n_{i,pol}$ is the perturbed ion polarisation density, $\langle \delta n_i \rangle$ is the perturbed gyro-averaged gyro-centre ion density and δn_e is the perturbed electron density.

The simplest model for electrons, applied to the study of ITG modes, assumes an adiabatic (or Boltzmann) electron response in the direction parallel to the magnetic field lines. The justification is that parallel electron motion is so fast that the electron population can establish a Boltzmann equilibrium at all times. This is equivalent to neglecting the electron inertia ($m_e \to 0$) for the parallel electron motion. We obtain then $e\nabla_\parallel\phi - (k_B T_e/n_e)\nabla_\parallel n_e = 0$, the solution of which is $n_e = \mathcal{N}(s)\exp[e\phi/k_B T_e]$, where s is a label of the magnetic field line. The normalisation constant $\mathcal{N}$ can be fixed

in configurations with nested flux surfaces by noting that the number of electrons should be conserved on flux surfaces. We obtain

$$\delta n_e = \frac{e n_0}{k_B T_e}\left(\delta\phi - \overline{\delta\phi}\right) \quad , \quad \overline{\delta\phi} = \frac{\int_\psi \delta\phi(s,\theta,\varphi) J(s,\theta) d\theta d\varphi}{\int_\psi J(s,\theta) d\theta d\varphi} \quad , \tag{8}$$

where $J = (\nabla s \cdot \nabla\theta \times \nabla\varphi)^{-1}$ is the Jacobian. The system of equations is (3)-(8). Note that the nonlinearity of the system appears in the last terms of Eq. (5), the *perpendicular nonlinearity*, and of Eq. (6), the *parallel nonlinearity*.

For the study of Trapped Electron Modes (TEM), it is appropriate to consider adiabatic passing electrons and drift-kinetic trapped electrons:

$$\delta n_e = \frac{e n_0}{k_B T_e}(1-\alpha_b)\left(\delta\phi - \overline{\delta\phi}\right) + \delta n_e|_{\text{trapped}} \tag{9}$$

where α_b is the fraction of trapped electrons.

For the study of electromagnetic perturbations, passing electrons must also be considered as non adiabatic, and the system of equations is to be completed by Ampère's law. In addition to the ITG and TEM modes, the model describes another branch of microinstabilities, named Alfvénic-ITG [58] or Kinetic Ballooning Mode [59]. For finite but small β, it is sufficient to consider a two potential approach $(\phi, A_\parallel)$ which neglects the perturbations of the magnetic field parallel to the equilibrium ($\delta B_\parallel \approx 0$). A full electromagnetic model in tokamak geometry taking into account finite $\delta B_\parallel$ formulated with a spectral approach can be found in [47].

Collisionality enters mainly in two different mechanisms. Electron-ion pitch angle collisions cause trapping / detrapping of electrons and therefore affect TEM. Ion-ion collisions cause damping of zonal flows and this results in an increase of the ITG turbulence level. This mechanism was studied in [48] with a 3D fluid model; results show an energy confinement time increase with decreasing collisionality and are interpreted as an increase in the effective critical temperature gradient due to the increased zonal flow amplitude, the so-called "upshift" first noticed in [3].

Finally, we should mention the gyro-Landau fluid equations which consist of a set of moments of the gyrokinetic equations that include models of the kinetic resonances such as Landau damping [60], linear and nonlinear finite Larmor radius effects [61] and toroidal drift [62]. An alternative non-dissipative closure model was introduced in [63]. Nonlinear gyrofluid simulations showed for the first time the importance of zonal flows in the saturation of ITG turbulence. Zonal flows have a linearly completely undamped component [64] and the closure of gyrofluid equations should reflect this property.

3. Numerical approaches

Two classes of approach have been used for the numerical resolution of gyrokinetic equations. The *Lagrangian* approach consists of a pseudo random sampling of f over phase space at points called "markers" or "tracers", an operation called "loading". Then their orbits are followed according to Eqs. (5-6), the so-called "pushing". One could assimilate this procedure to a completely unstructured, moving grid. At every

timestep the density in real space is reconstructed by a projection of the markers, an operation called "charge assignment". The field equations are then solved on a fixed grid in real space, e.g. with a finite element technique [50]. The advantages of this particle-in-cell (PIC) technique are its conceptual simplicity and the ability to integrate systems of high dimensionality. The main drawback is the problem of statistical noise inherent to this approach and the associated slow convergence rate $\sim 1/\sqrt{N}$ with the number of markers. Noise can build up and accumulate in nonlinear simulations to a point where basic physical properties of the system, such as charge and energy conservation, are violated. A method to reduce this problem was formulated some time ago, the δf approach, which statistically samples the perturbed part of the distribution function only [65]. A further improvement consists of choosing an appropriate distribution of the markers in phase space ("optimised loading"). It was shown in [4] that the application of this technique leads to a substantial improvement in the quality of the numerical simulation as measured by the verification of the energy conservation property. It was shown in [6] that this is crucial in order to obtain a physically correct level of zonal flows, turbulence and anomalous heat flux. A further simplification was achieved by showing that the integration of the time evolution equation for δf along the perturbed characteristics is actually redundant, and it is perfectly appropriate simply to take $\delta f = f(\mathbf{R}, v_\parallel, \mu)|_{t=0} - f_0(\mathbf{R}, v_\parallel, \mu)|_{t=t}$, where f_0 is a known distribution function [66]. Moreover, the time evolution equation for δf assumes that f_0 is a constant along the unperturbed orbits (in other words it is an equilibrium distribution function) therefore it should be a function of the constants of motion of the unperturbed orbits: particle energy $\mathcal{E}$, magnetic moment μ and conjugate toroidal momentum $\psi_0 = \psi + (m_s/q_s)(F/B)v_\parallel$. If a local approximation is chosen for f_0, i.e. a function of ψ instead of ψ_0, this can lead to a spurious drive of zonal flows [5].

The *Eulerian* approach (sometimes called "Vlasov" in the literature [67]) consists of discretising the phase space on a fixed grid. The time evolution equations for f are solved using finite difference or finite element techniques. The time integration can be performed using explicit or semi-implicit schemes. An advanced code using this approach in the context of gyrokinetic simulations is described in detail in Ref.[2]. An advantage of the Eulerian approach (as compared to Lagrangian) is that it is in principle easier to control the phase space gridding. In addition, the numerical convergence properties with mesh size should be free of statistical noise. The drawbacks are perhaps that this approach is technically more difficult to implement, and that the appearance of fine scale structures in phase space ("filamentation") requires very fine grid resolution in certain regions of phase space. An intermediate approach, called *semi-Lagrangian* or *semi-Eulerian*, consists of discretising the phase space on a fixed grid, as in the Eulerian scheme, and following orbits in phase space, as in the Lagrangian scheme, with f interpolated from the previous time step at the foot of the orbit [68].

Numerical approaches differ in the level of globality that the schemes can support. From local to global we find in increasing order: (a) the ballooning approximation, that solves along a field line and assumes large toroidal mode numbers; (b) the flux-tube

geometry that solves in a finite size domain in the vicinity of a field line and assumes periodic boundary conditions; (c) the toroidal ring in which a finite size radial slice of the plasma is simulated; (d) the full radius approach in which the equations are solved from the magnetic axis to the plasma boundary. The most global approach is of course highly desirable and even necessary when structures develop with a radial extent comparable to the system size. The flux tube and toroidal ring approaches certainly make sense when studying electron scale turbulence for which a full radius scheme would be prohibitive. The drawback of the flux tube approach is in its unphysical radial periodic boundary conditions. The toroidal ring approach allows for more physical boundary conditions such as fixed edge flux and evolving temperature profiles. There are more variations in the way the time evolution of plasma profiles is considered. In several codes a fixed temperature gradient profile is assumed, sources and sinks may be added, or a dissipative term is introduced that models relaxation to an initial Maxwellian. In other codes the temperature profiles are defined consistently with the temperature gradient profiles and, moreover, are left free to evolve in time.

The difficulty associated with the large parallel / perpendicular anisotropy in time and length scales has prompted the development of field-aligned meshes [1],[2]. Another approach is to define a magnetic straight-field line coordinate and apply a variable transformation to extract the fast poloidal phase variation: a gain in code performance of one or two orders of magnitude can be reached [50],[5].

The validation of numerical simulation codes is extremely important considering the complexity of the physics involved. This requires not only case comparisons with selected experiments [45],[46] but also a verification of the first principles these codes are based on [4], [6]. Another important element is to perform cross benchmarking of the different codes [3].

4. Toroidal coupling, zonal flows and parallel nonlinearity

Toroidal coupling enters at three different points in the gyrokinetic equations. First, the particle motion grad-B drifts have the effects of (a) driving a toroidally coupled mode (e.g. the toroidal-ITG) more unstable than its "slab" counterpart and (b) creating a trapped particle population in the minimum B regions which can cause other modes to become unstable (TEM and TIM). Second, the geometry appears explicitly in the field equations through the expressions of differential operators. Third, in the adiabatic electron response, the zonal component, $\overline{\delta\phi}$, contains a Jacobian of the toroidal magnetic coordinates, see Eq. (8).

We consider a tokamak configuration given by an ideal MHD equilibrium with the following parameters: aspect ratio $R/a = 2.2$, minor radius $a = 96\rho_s$, $q_0 = 1.7$, $q_a = 4.7$, T_i profile with $\max(R/L_T) = 7.9$ (which is about twice higher than the linear instability threshold for toroidal ITG modes), uniform density and T_e profiles. We solve the nonlinear electrostatic gyrokinetic equations (3-8) with the full radius code ORB5 [69] using $N = 33 \times 10^6$ markers, and cubic spline finite elements in (s, θ, φ) on a

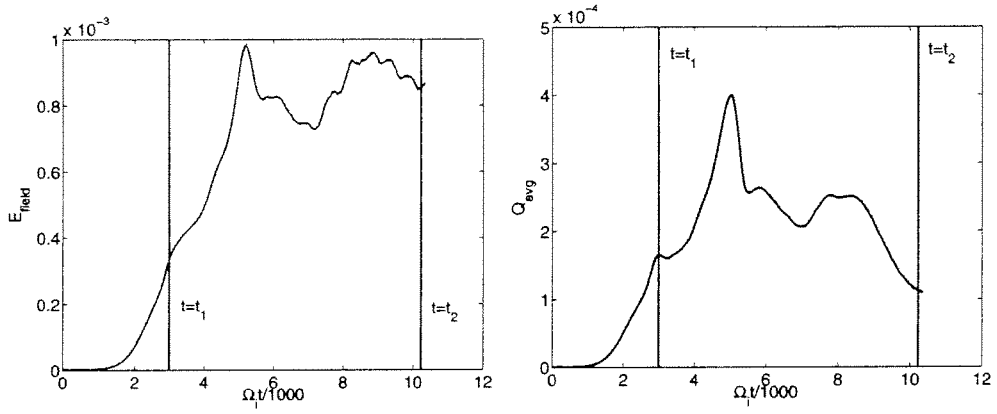

Figure 1. *Time evolution of field energy (left) and averaged heat flux (right) in a tokamak of aspect ratio 2.2. The simulation includes the toroidal coupling of zonal flows coming through the adiabatic electron response, Eq. (8).*

$32 \times 256 \times 128$ grid. All profiles are global and free to evolve. The model includes parallel nonlinearity and toroidal coupling in the zonal component, Eq. (8). The initial distribution function f is a canonical Maxwellian, i.e. function of the constants of motion of the unperturbed orbits. Figure 1 shows the time traces of field energy and heat flux and Figure 2 radial profiles of the zonal $E \times B$ velocity and effective temperature at different time slices. While in the early stage of the nonlinear process small scale zonal flows appear, at a later stage the radial structure of zonal flows expands radially to form finally two very broad radial zones. Global simulations in a cylinder [6, 70, 71] had shown a persistent radial structure of zonal flows with a much finer radial structure. The explanation for this different behaviour may lie in the evolution of the effective temperature profile (Fig.2): for the toroidal case the instability drive is much stronger and consequently the profile evolution occurs on a much shorter timescale as compared to the cylindrical case: the effective temperature profile evolves quickly to a profile which is closer to the marginal stability of the toroidal-ITG mode.

The above results have been obtained with the parallel nonlinearity retained (last term in Eq. (6)). A comparison between two simulations, with and without parallel nonlinearity, is shown in Fig.3, for the same toroidal case as in Figs 1-2, and in which the optimised loading scheme [4] has been applied in order to reduce the statistical noise accumulation at long simulation times. There is a visible effect on the zonal $E \times B$ flow pattern. Note that an effect of the parallel nonlinearity on zonal $E \times B$ flow structures was already found in cylindrical simulations [6, 70, 71].

The evolution of zonal flows towards broad radial structures is confirmed in computations using the nonlinear global gyrokinetic code GT3D [5] that includes, as for the ORB5 code, parallel nonlinearity and a canonical Maxwellian. The perturbed field is represented on 2D quadratic spline finite elements with 76 non-uniform radial intervals, 32 poloidal intervals with a quasi-ballooning representation [50] and 32 toroidal

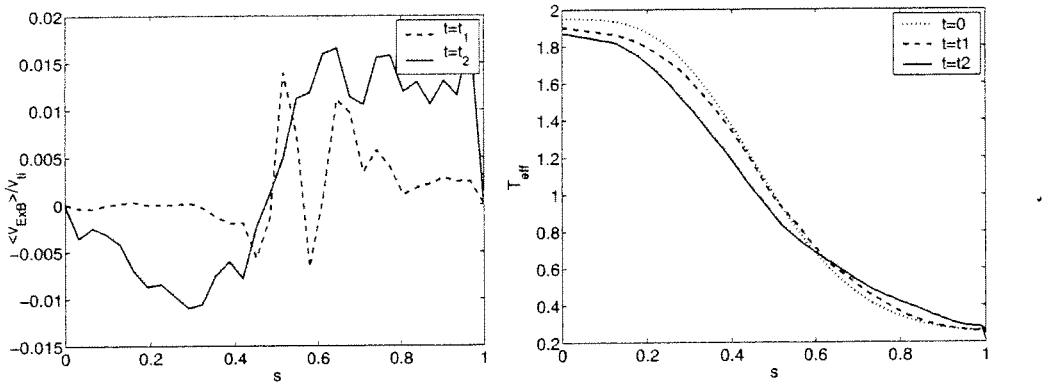

Figure 2. *Radial profiles of magnetic surface averaged zonal $E \times B$ velocity (left) and effective temperature profiles taken in the early (dashed line, $t = t_1$) and late (continuous line, $t = t_2$) nonlinear phases, for the simulation of Fig.1.*

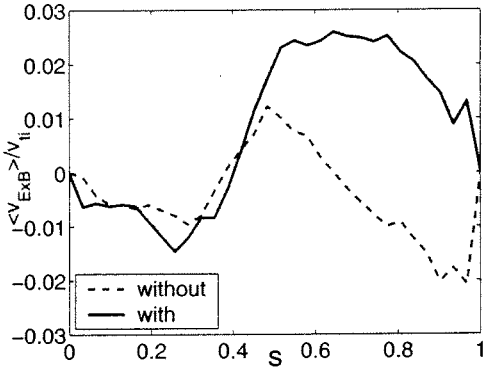

Figure 3. *Radial profiles of magnetic surface averaged zonal $E \times B$ velocity in the late nonlinear phase, for simulations with (-) and without(--) parallel nonlinearity. Same physical parameters as for Figs 1 and 2, optimised loading applied.*

Fourier components. We use parameters of the Cyclone base case [3]: $R/a = 2.7$, $a = 150\rho_{Li}$, $R/L_T = 6.9$. Two series of simulations are performed, one using the cylindrical approximation for the zonal component, $\overline{\delta\phi} \approx \delta\phi_{m=0,n=0}$, the other with the true toroidal Jacobian, Eq. (8). The optimized loading technique [4] is applied in order to reduce numerical noise and 160 million tracers are used. Energy conservation is better than 30 % of the perturbed field energy for the cases shown in the following figures. The time evolution of the field energy, Fig.4, shows remarkable differences: in the simulation with approximated zonal flows (left), the peak in field energy is about 30 % lower. After the peak, the decay time is much longer, resulting in a twice higher field energy in nonaxisymmetric modes at the end of the simulation, as compared to the case with true toroidal zonal flows (right). The remaining slow decay is due to a slow temperature gradient flattening (note that there are no sources in our simulations).

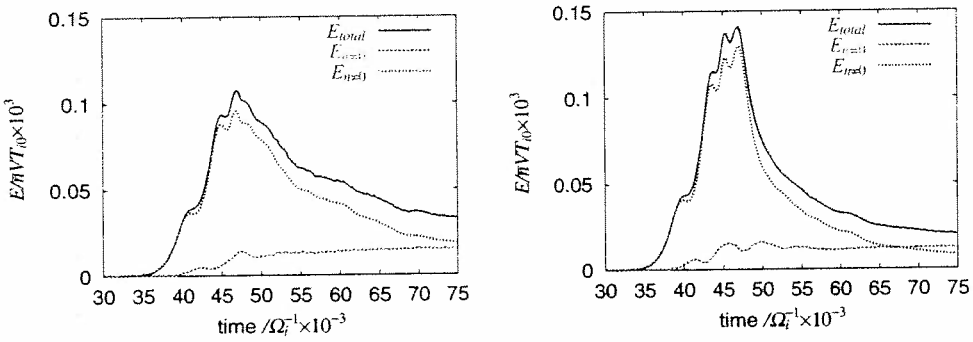

Figure 4. *Time evolution of perturbed field energy, total (red), in axisymmetric (green) and non axisymmetric (blue) modes; without (left) and with (right) toroidal coupling in the surface averaged zonal component $\overline{\delta\phi}$, Eq. (8). Cyclone base case parameters*

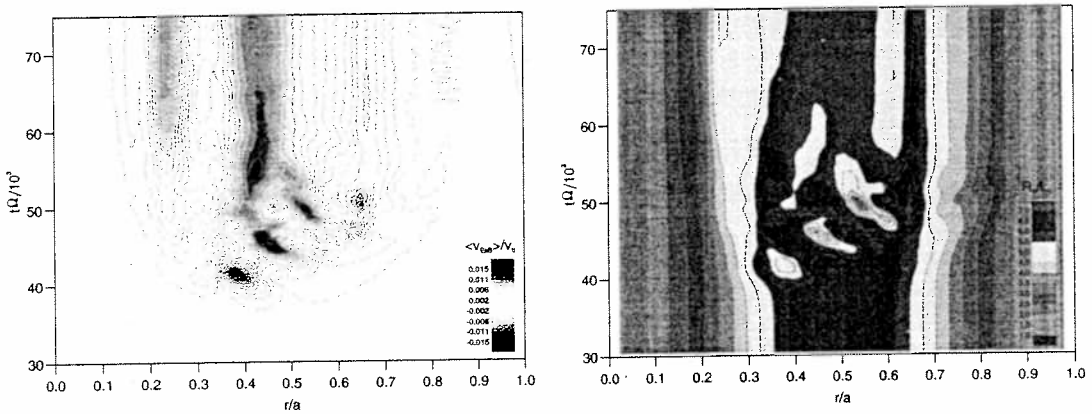

Figure 5. *Left: contours of flux averaged $E \times B$ drift velocity versus r/a and t. Colour scale: blue for negative, red for positive, min/max: $< v_E \times B >= \pm 0.018\, v_{ti}$. Right: contours of effective ion temperature gradient inverse scale length. Colour scale: max $R/L_T = 7$.*

We show in Figure 5 (left) a contour plot of the zonal $E \times B$ velocity versus minor radius and time, for the case with toroidal zonal flows. The apearance of broad zones (three in this case) at later stages is very clear. The small amplitude oscillations near the plasma edge are Geodesic Acoustic Modes (GAM) [44]. In the earlier stages, a series of peaks in the $E \times B$ velocity appears at increasing radial positions. These peaks immediately follow bursts in heat flux which in turn cause local and temporary flattenings of the temperature gradient (Fig.5, right) at the corresponding locations. The fast timescale radial turbulence spreading is thus caused by avalanche processes, with changes in temperature gradient due to bursts in heat flux and excitation of ITG fluctuations followed by zonal flow bursts. The temperature gradient long time evolution shows a visible flattening, bringing it closer to the linear marginal stability threshold of $R/L_T \approx 5$ (computed in the absence of $E \times B$ flows).

5. Conclusions and future developments

In both cylindrical ([6, 70, 71]) and toroidal simulations presented here, radial turbulence spreading is observed. For both cases zonal flows organise the turbulence and the system evolves to a quasi-steady state with a regular pattern of zonal $E \times B$ flows. For both cases it is important to retain the parallel nonlinearity in order to obtain a correct zonal $E \times B$ flow structure. In a torus, the stronger instability drive is such that the nonlinearity due to profile evolution becomes important. Toroidal coupling of zonal flows is affecting their interaction with ITG driven perturbations. This has a measurable effect on their development and saturation. In a torus, fast radial turbulence spreading is caused by sequences of avalanches in which bursts of ITG turbulence are accompanied by temperature gradient local flattening and followed by zonal $E \times B$ bursts. The system evolves in the long term to a state characterised by quasi-steady zonal structures of a much larger width $(30 - 50\rho_{Li})$ than in a cylinder $(\sim 10\rho_{Li})$. This difference may be related to the radially more extended structures of the toroidal ITG mode as compared to the "slab" ITG mode, although more extensive studies are needed to confirm this.

There are still challenges for future numerical simulations. Generally speaking, electron transport and density transport are much less well understood. Another feature observed in experiments, namely the relation of rational $q_{\min}$ values in reversed shear discharges with the appearance of internal transport barriers, has not been fully understood as yet. Another open question is the finite β dependence of anomalous transport. All these questions will require consideration of non-adiabatic electron response and even electromagnetic perturbations. While numerical tools have recently been developed for these purposes, there remains considerable work in order to answer these questions with sufficiently accurate first-principles based simulations.

Acknowledgments

We wish to thank J. Nührenberg, Y. Kishimoto, P.H. Diamond, T.S. Hahm, Z. Lin for stimulating discussions. Work partly supported by the Swiss National Science Foundation. Computations were performed on the JAERI Origin 3800 system and on the EPFL Pleiades cluster.

References

[1] Lin Z, Hahm T S, Lee W W, Tang W M and White R B 1998 *Science* **281** 1835
[2] Candy J and Waltz R E, 2003 *J Comput Phys* **186** 545
[3] Dimits A M *et al* 2000 *Phys. Plasmas* **7** 969
[4] Hatzky R *et al* 2002 *Phys. Plasmas* **9** 898
[5] Idomura Y, Tokuda S and Kishimoto Y 2003 *Nucl. Fusion* **43** 234
[6] Villard L *et al* 2004 *Nucl. Fusion* **44** 172
[7] Parker S E, Chen Y, Wan W, Cohen B I and Nevins W M 2004 *Phys. Plasmas* **11** 2594;
[8] Scott B D 2002 *New J Physics* **4** 52
[9] Sydora R D , Decyck V K, Dawson J M 1996 *Plasma Phys. Controlled Fusion* **38** A281

First principles based simulations of instabilities and turbulence

[10] Jenko F, Dorland W, Kotschenreuther M and Rogers B N 2000 *Phys. Plasmas* **7** 1904
[11] Dorland W, Jenko F, Kotschenreuther M and Rogers B N 2000 *Phys. Rev. Lett* **85** 5579
[12] Labit B and Ottaviani M 2003 *Phys. Plasmas* **10** 126
[13] Li J Q and Kishimoto Y 2004 *Phys. Plasmas* **11** 1493
[14] Dimits A M and Lee W W 1993 *J Comput Phys* **107** 309
[15] Manuilskiy I and Lee W W 2000 *Phys. Plasmas* **7** 1381
[16] Watanabe T H and Sugama H 2004 *Phys. Plasmas* **11** 1476
[17] Degtyarev L *et al* 1997 *Comput Phys Commun* **103** 10
[18] Angioni C, Goodman T P, Henderson M A and Sauter O 2003 *Nucl Fusion* **43** 455
[19] Miller R L *et al* 1997 *Phys. Plasmas* **4** 1062
[20] Cooper W A *et al* 2002 *Plasma Phys. Controlled Fusion* **44** B357
[21] Lütjens H and Luciani J F 2002 *Phys Plasmas* **9** 4837
[22] Fu G Y and Van Dam J W 1989 *Phys Fluids B* **1** 1949
[23] Cheng C Z 1991 *Phys Fluids B* **3** 2463
[24] Villard L, Brunner S and Vaclavik J 1995 *Nucl. Fusion* **35** 1173
[25] Jaun A, Fasoli A, Vaclavik J and Villard L 2000 *Nucl. Fusion* **40** 1343
[26] Guzdar P N, Chen L, Tang W M and Rutheford P H 1983 *Phys. Fluids* **26** 673
[27] Adam J C, Tang W M and Rutheford P H 1976 *Phys. Fluids* **19** 561
[28] Horton W, Hong B G and Tang W M 1988 *Phys. Fluids* **31** 2971
[29] Gladd N T, Drake J F, Chang C L and Lin C S 1980 *Phys. Fluids* **23** 1182
[30] Connor J W, Fukuda T, Garbet X, Gormezano C, Mukhovatov V and Wakatani M 2004 *Nucl. Fusion* **44** R1.
[31] Diamond P H, Liang Y-M, Carreras B A and Terry P W 1994 *Phys. Rev. Lett.* **72** 2565
[32] Garbet X *et al* 1999 *Nucl. Fusion* **39** 2063
[33] Sarazin Y, Garbet X, Ghendrih P and Benkadda S 2000 *Phys. Plasmas* **7** 1085
[34] Benkadda S *et al* 2001 *Nucl. Fusion* **41** 995
[35] Graves J P, Dendy R O, Hopcraft K I and Jakeman E 2002 *Phys. Plasmas* **9** 1596
[36] Tangri V, Das A, Kaw P and Singh R 2003 *Phys. Rev. Lett.* **91** 025001
[37] Li Jiquan and Kishimoto Y 2002 *Phys. Rev. Lett.* **89** 115002
[38] Lin Z, Hahm T S, Lee W W, Tang W M and White R B 2000 *Phys. Plasmas* **7** 1857
[39] Hahm T S , *et al* 2004 *Plasma Phys. Controlled Fusion* **46** A323
[40] Lin Z and Hahm T S 2004 *Phys. Plasmas* **11** 1099
[41] Zonca F, White R B and Chen L 2004 *Phys. Plasmas* **11** 2488
[42] Garbet X, Laurent L, Samain A and Chinardet J 1994 *Nucl. Fusion* **34** 963
[43] Beer M A, *et al* 1997 *Phys. Plasmas* **4** 1792
[44] Winsor N, Johnson J L and Dawson J M 1968 *Phys. Fluids* **11** 2448
[45] Candy J and Waltz R E 2003 *Phys. Rev. Lett.* **91** 045001
[46] Bottino A, Peeters A G, Sauter O, Vaclavik J and Villard L 2004 *Phys. Plasmas* **11** 198
[47] Ganesh R , Angelino P , Vaclavik J and Villard L 2004 *Phys. Plasmas* **11** 3106
[48] Falchetto G L and Ottaviani M 2004 *Phys. Rev. Lett.* **92** 025002
[49] Chen Y and Parker S E 2003 *J. Comput. Phys.* **189** 463
[50] Fivaz M *et al* 1998 *Comput. Phys. Commun.* **111** 27
[51] Jost G, Tran TM, Cooper WA, Villard L and Appert K 2001 *Phys. Plasmas* **8** 3321
[52] Kornilov V, Kleiber R, Hatzky R, Villard L and Jost G 2004 *Phys. Plasmas* **11** 3196
[53] Freidberg J P 1987 *Ideal Magnetohydrodynamics*, Plenum Press, New York and London
[54] Dubin D H E, Krommes J A, Oberman C and Lee W W 1983 *Phys Fluids* **26** 3524
[55] Hahm T S 1988 *Phys. Fluids* **31** 2670
[56] Brizard A 1989 *J. Plasma Phys.* **41** 541
[57] Hahm T S 1996 *Phys. Plasmas* **3** 4658
[58] Zonca F, Chen L, Dong J Q, Santoro R A, 1999 *Phys. Plasmas* **6** 1917
[59] Kim J Y, Horton W, Dong J Q, 1993 *Phys. Fluids B* **5** 4030

First principles based simulations of instabilities and turbulence

[60] Hammett G W and Perkins F W 1990 *Phys Rev Lett* **64** 3019
[61] Dorland W and Hammett G W 1993 *Phys. Fluids B* **5** 812
[62] Waltz R E, Dominguez R R and Hammett G W 1992 *Phys. Fluids B* **4** 3138
[63] Sugama H, Watanabe T H and Horton W 2003 *Phys. Plasmas* **10** 726
[64] Rosenbluth M N and Hinton F L 1998 *Phys. Rev. Lett.* **80** 724
[65] Parker S E and Lee W W 1993 *Phys. Fluids B* **5** 77
[66] Allfrey S J and Hatzky R 2003 *Comput. Phys. Commun.* **154** 98
[67] Manfredi G, Shoucri M, Dendy R O, Ghizzo A and Bertrand P 1996 *Phys. Plasmas* **3** 202
[68] Sonnendrucker E, Roche J, Bertrand P, Ghizzo A 1999 *J. Comput. Phys.* **149** 201
[69] Tran T M *et al* 1998 *Proc. Int. Workshop, Varenna, Theory of Fusion Plasmas* (Editrice Compositori, Bologna, Italy) 45
[70] Allfrey S J *et al* 2002 *New J. Phys.* **4** art.no.29
[71] Allfrey S J *et al* 2002 *Proc. Int. Workshop, Varenna, Theory of Fusion Plasmas* (Società Italiana di Fisica, Bologna, Italy) p.171

Generalised evolving background f_0 for plasma δf Particle-in-cell simulations

S.J. Allfrey, S. Brunner

Centre de Recherches en Physique des Plasmas, Association EURATOM-Confédération Suisse, EPFL, 1015 Lausanne, Switzerland

1. Introduction

The noise in electrostatic PIC simulation is the error inherent in calculating the charge density with a Monte Carlo (statistical) technique using a finite number of sampling points (markers).

The δf scheme aims to reduce the noise in the PIC method by splitting the full distribution function as $f = f_0 + \delta f$, with f_0 referred to as the background. The charge density is calculated analytically from f_0 and statistically from δf. If δf is small compared to f_0 the error in the resultant charge density is smaller than for a full-f scheme [1], *i.e.* the noise is reduced. Such a procedure requires the specification of an f_0 close to the true value of the distribution function f. It is through this additional information that the simulation wins.

The importance of a good choice of the background has been demonstrated both theoretically [2][1] and practically [3]. However, it is clear that if f_0 is fixed and f evolves far from its initial value, δf is not going to remain small. Hence one seeks methods by which f_0 may be evolved in time in order to avoid this.

For collisional dominated simulations the obvious choice of f_0 is a Maxwellian distribution, f_M. Brunner *et.al.* [4] showed the practicality of such a scheme which evolved the three parameters of a Maxwellian f_0 with fluid equations, closed using information from the markers. Valeo [5] also considered an evolving Maxwellian background for modelling of electron plasma waves.

When the system is not collision dominated a Maxwellian f_0 is not necessarily appropriate. We seek therefore to develop methods which use a more general representation of the evolving background.

Our current project is to examine the properties of one such generalised scheme which represents f_0 on a fixed phase space grid thus allowing for an arbitrary number of free parameters. We investigate the feasibility of this approach for solving the Vlasov-Poisson system in a 2 dimensional (x,v) phase space.

2. The model

We solve the Vlasov equation,

$$\partial_t f_s + v\,\partial_x f_s + \frac{q_s E}{m_s}\,\partial_v f_s = 0. \tag{1}$$

Where $f_s(x,v)$ may be the electron or ion distribution function. In the former case $s = e$ the eclectic field E is calculated using Poisson's equation with the ions assumed to provide a fixed neutralising background.

$$\partial_x E = -\frac{e}{\epsilon_0}\int f_e\,dv + \frac{eN_0}{\epsilon_0} \tag{2}$$

here

$$N_0 L \stackrel{\text{def}}{=} \int f\,dx\,dv \qquad\qquad L \stackrel{\text{def}}{=} \int dx \tag{3}$$

. In the latter case $s = i$ the electric field is calculated using the quasineutrality condition $N_i = N_e$ together with an adiabatic electron response,

$$\int f_i \, dv = N_0 \, e^{\frac{e\phi}{T_e}} \tag{4}$$

$$\frac{e\phi}{T_e} = \log \frac{N_i}{N_0} \tag{5}$$

. In the PIC method the markers, distributed as $p(x, v)$, represent f as

$$\sum_i^N f_i \delta(x - x_i)\delta(v - v_i) \tag{6}$$

and solution of discretised forms of Eqs (2) or (4) will require evaluation of

$$\int f(x, v)\Lambda_j(x) \, dx \, dv \tag{7}$$

where the Λ_j are the functions used to discretise the density. The δf method corresponds to calculating this as

$$\int f_0(x, v)\Lambda_j(x) \, dx \, dv + \frac{1}{N} \sum_i^N \frac{\delta f_i \Lambda_j(x_i)}{p_i} \tag{8}$$

.

3. Adaptive f_0 for the electron plasma wave

The Landau Damping of an electron plasma wave was chosen as the test scenario for the scheme. Two adaptation algorithms have been looked at

$$(i) \quad f_0(t) \simeq f_0(t - \Delta t) \qquad (ii) \quad f_0(t) \simeq \langle f \rangle_{x,t}$$

. In the first case

$$f_0(x, v) = f_M(v) + \alpha_{ij}(t) S_{ij}(x, v) \tag{9}$$

With the S_{ij} cubic splines in x (corresponding to the functions used to represent the density) and piecewise constant in v. The coefficients α_{ij} were calculated using a marker deposition in phase space at the previous time step and a mass lumping approximation for the spline inversion problem. Under this scheme the background may contribute to the charge density.

In the second case the adaptive part of the background was taken to be a time and space-averaged departure from the initial Maxwellian, represented by piecewise constant functions.

$$f_0(v) = f_M(v) + \alpha_i(t) C_i(v) \tag{10}$$

Here a running average in time was used,

$$\alpha_i(t^{j+1}) = \beta \frac{1}{L} \int f(x, v, t^{j+1}) C_i(v) \, dv \, dx + (1 - \beta)\alpha_i(t^j) \tag{11}$$

representing a decaying time average weighted as $\exp -\frac{\beta}{\Delta t} t$, in the limit of small β. For this scheme, f_0 does not contribute directly to the charge density.

4. Preliminary results and conclusions

A population of 128,000 markers with $p \propto f$ was used. f_0 was gridded with 23 points in x

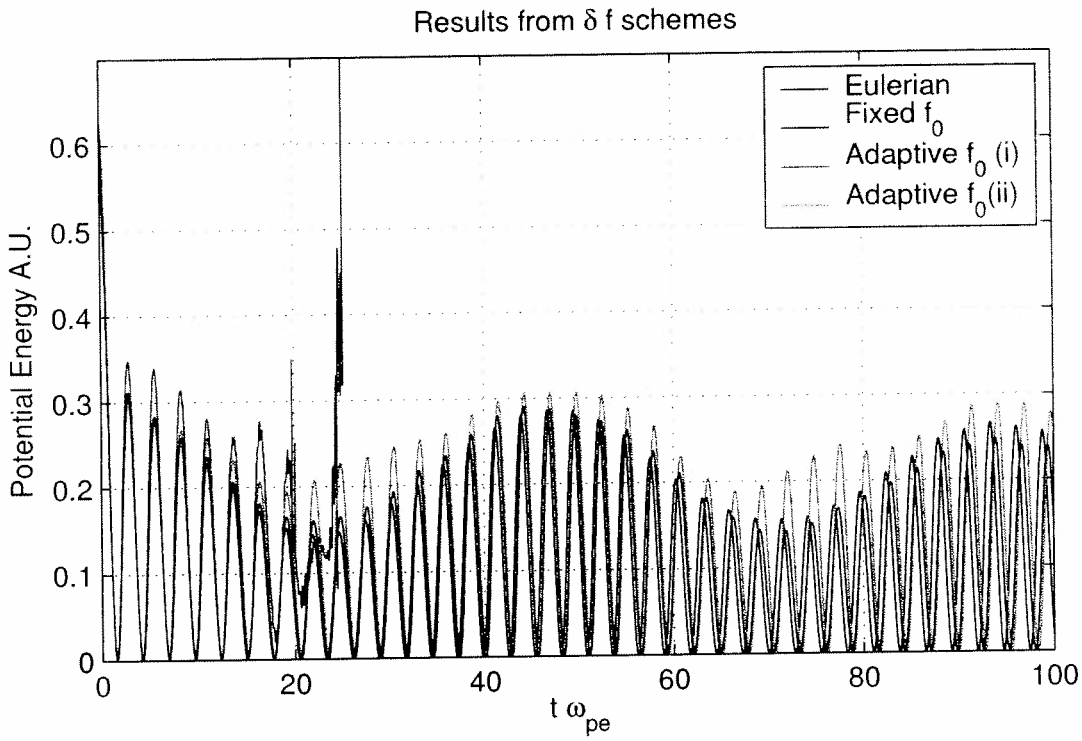

Figure 1: A comparison of the total electrostatic potential energy as a function of time for the Eulerian, fixed f_0 PIC and the two adaptive f_0 PIC variant codes. Algorithm (i) becomes unstable around $t\omega_{pe} \simeq 23$.

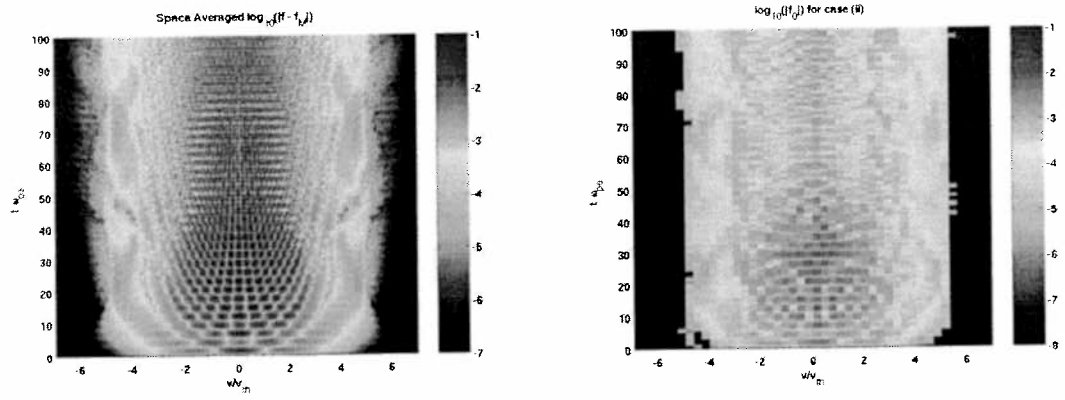

Figure 2: Left: The time evolution of the departure of the space averaged distribution function from the Maxwellian (Eulerian code). Right: The time evolution of f_0 for algorithm (ii). The adaptation captures some of the behaviour in the trapping region $v_\phi \simeq 3.8 v_{th}$.

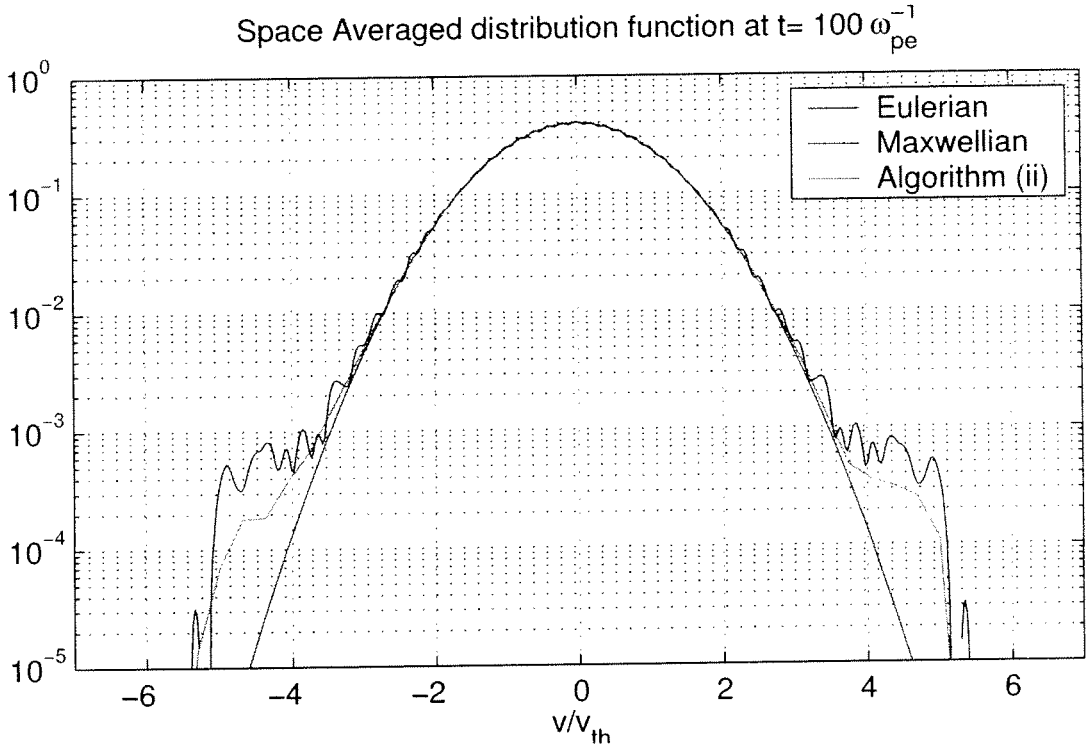

Figure 3: The spaced averaged distribution function at the end of the simulation $t\omega_{pe} = 100$, flattening in the trapping region is reflected in the adaption of f_0 (green line) for algorithm (ii)

and 64 points in v and a time step of $0.01/\omega_{pe}$. An Eulerian code was used to benchmark the PIC methods. Results are plotted in figure 1. A fixed $f_0 = f_M$ scheme was able to reasonably match the Eulerian result. Adaptation algorithm (i) was subject to an as yet unidentified numerical instability. A formal evaluation of the relative error in the density due to f_0 and that due to δf is required for this case. For algorithm (ii), $\beta = 0.05$, the background was able to capture some of the secular effects, the flattening in the trapping region (around $v_\phi = 3.8 v_{th}$), see figures 2 and 3. The representation of such secular terms, in particular profile flattening, is of great interest in *e.g.* gyrokinetic turbulence simulation.

[1] S. J. Allfrey and R. Hatzky. A revised delta-f algorithm for nonlinear pic simulation. *Comput. Phys. Commun.*, 154:98, 2003.

[2] A. Y. Aydemir. A unified monte carlo interpretation of particle simulations and applications to non-neutral plasmas. *Phys. Plasmas*, 1:822, 1994.

[3] R. Hatzky, T. M. Tran, A. Könies, R. Kleiber, and S. J. Allfrey. Energy conservation in a nonlinear gyrokinetic particle-in-cell code for ion-temperature-gradient-driven modes in θ-pinch geometry. *Phys. Plasmas*, 31:898, 2002.

[4] S. Brunner, E. Valeo, and J. A. Krommes. Collisional delta-f scheme with evolving background for transport times scale simulations. *Phys. Plasmas*, 6(12):4504, 1999.

[5] E. J. Valeo and S. Brunner. A kinetic δf model of plasma and acoustic waves which includes an evolving background distribution. APS DPP 2001.

BOOTSTRAP CURRENT AND MHD STABILITY IN A 4-PERIOD HELIAS REACTOR CONFIGURATION

W. A. Cooper [1], T. Andreeva [2], C. Beidler [2], Y. Igithkhanov [2], J. Kisslinger [3], H. Wobig [3], M. Yu. Isaev [1,4]

[1] *Centre de Recherches en Physique des Plasmas, Association Euratom-Confédération Suisse, Ecole Polytechnique Fédérale de Lausanne, Lausanne, Switzerland*

[2] *Max-Plank-Institut für Plasmaphysik, IPP-EURATOM Association, Greifswald, FRG*

[3] *Max-Plank-Institut für Plasmaphysik, IPP-EURATOM Association, Garching, FRG*

[4] *Russian Research Centre "Kurchatov Institute", Moscow, Russia*

The bootstrap current (BC) that results from the difference in frictional and viscous forces between trapped and circulating ions and electrons in magnetic confinement systems can impact the equilibrium and magnetohydrodynamic (MHD) stability properties of stellarator systems. We investigate the equilibrium and ideal MHD stability of a 4-field period Helias reactor configuration with aspect ratio 8.4 and plasma volume $1500m^3$ [1] using the three dimensional (3D) free boundary version of the VMEC code [2] and the 3D TERPSICHORE code [3] with a converged selfconsistent bootstrap current in the collisionless $1/\nu$ regime [4]. We also examine equilibria with analytic toroidal current profiles that model the behaviour of the BC that is in part or totally suppressed by counter electron cyclotron current drive (ECCD).

Converged profiles for the BC are obtained up to volume averaged $< \beta > \simeq 4.6\%$. Under free boundary conditions, the BC causes a slight outward shift and elongation of the plasma column. The pressure profile is prescribed as $p(s) = p(0)[1 - s - 0.1(1 - s^{10})]/0.9$, where $0 \leq s \leq 1$ is the radial variable roughly proportional to the volume enclosed. Thus, the pressure profile is nearly parabolic but with a vanishing gradient at the edge of the plasma to avoid current profile discontinuities at the plasma-vacuum interface (PVI) generated by finite BC. With this profile, the BC is hollow and peaks just outside midvolume between $s = 0.5$ and $s = 0.6$. The BC peak shifts weakly inwards with increasing $< \beta >$ as shown in Fig. 1. The BC increases the rotational transform ι at the edge from 0.96 in vacuum to almost unity without surpassing this value at relatively modest values of $< \beta >$. At $< \beta > \simeq 2.5\%$, the ι-profile is flat and close to unity in the outer 20% of the plasma volume and this extends to the outer 40% when $< \beta > \simeq 4.5\%$. The ι-profiles for the vacuum state and at finite β due to the action of the BC are displayed in Fig. 2. The toroidal component of the BC reaches $-300kA$ at $< \beta > \simeq 4.5\%$. This behaviour can have adverse implications for ideal MHD stability. Not only is the Mercier criterion destabilised, but global external modes are also predicted. Furthermore, if we artificially suppress the BC, the configuration remains unstable, but the eigenvalue is an order of magnitude smaller as shown in Fig. 3. The internal plasma potential energy δW_P can be separated into three terms, namely $\delta W_P = \delta W_{C^2} + \delta W_D + \delta W_J$ [5]. The stabilising component is δW_{C^2}, while δW_D denotes the ballooning/interchange instability driving mechanism and δW_J denotes the parallel current density $\boldsymbol{j} \cdot \boldsymbol{B}/B^2$ driving mechanism associated with global kink modes. The global mode structure that is destabilised at $< \beta > \simeq 4.5\%$ is dominantly driven by $\boldsymbol{j} \cdot \boldsymbol{B}/B^2$ as $|\delta W_J| >> |\delta W_D|$. We have found that the flux surface averaged contribution of $\boldsymbol{j} \cdot \boldsymbol{B}/B^2$ to δW_J is weak indicating that the direct contribution of the BC to the kink destabilising mechanism is

small. However, the BC alters the Pfirsch-Schlüter current significantly and this provides the main driving energy for the global mode observed. The radial profiles of δW_{C^2}, δW_D, δW_P and δW_J are displayed for the full selfconsistent BC case at $< \beta > \simeq 4.5\%$ in Fig. 4. The main point that can be extracted from these results is the probable requirement of some external means for rotational transform control like ECCD in a Helias reactor.

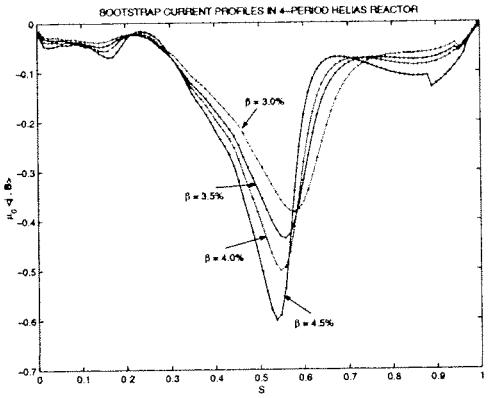

Fig. 1. The converged selfconsistent bootstrap current profiles in the collisionless $1/\nu$ regime in a 4-period Helias reactor at $< \beta > \simeq 3\%$, 3.5%, 4% and 4.5%.

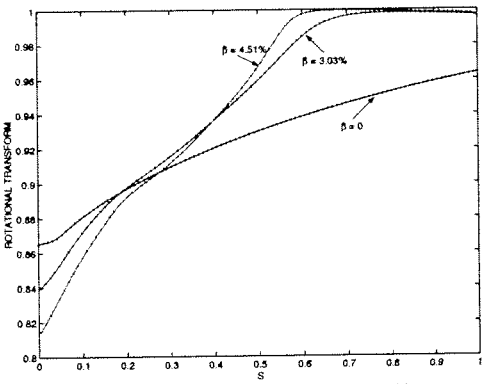

Fig. 2. The rotational transform ι-profiles in vacuum, at $< \beta > \simeq 3\%$ and at $< \beta > \simeq 4.5\%$ obtained with converged selfconsistent bootstrap currents in the collisionless $1/\nu$ regime in a 4-period Helias reactor.

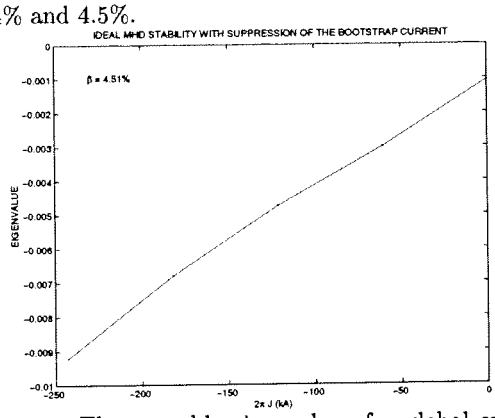

Fig. 3. The unstable eigenvalue of a global external kink mode dominated by the $m/n = 1/1$ component as function of the toroidal current as the magnitude of the BC is artificially suppressed while keeping its profile fixed.

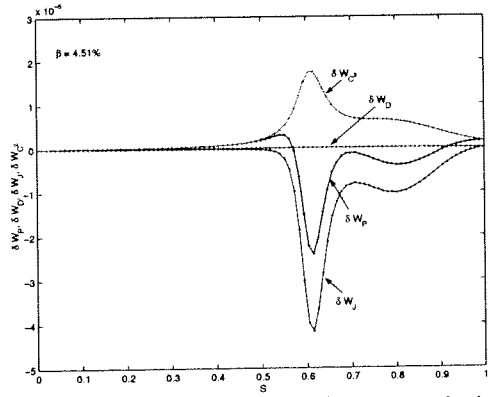

Fig. 4. The radial profiles of energy principle components δW_{C^2}, δW_D, δW_P and δW_J for the full $(-303kA)$ selfconsistent BC case at $< \beta > \simeq 4.5\%$ in a 4-period Helias reactor.

To model the combined effects of the BC with counter ECCD, we consider an analytic polynomial input toroidal current profile of the form

$$2\pi J'(s) = \frac{2310}{(1-22\alpha)} s^2(s^4-\alpha)(1-s)^4 2\pi J(1) \qquad (1)$$

where $2\pi J(s)$ corresponds to the toroidal plasma current enclosed within s and prime ($'$) denotes the derivative with respect to s. We vary both the total toroidal current $2\pi J(1)$ and α simultaneously to obtain a sequence of equilibria for which the ECCD balances the BC. Typically, $2\pi J(1) = -285, -150, -45. - 15, +15, +45kA$ for $\alpha = 0.0023, 0.0227, 0.0386, 0.0432.0.0477, 0.0523$, respectively. Note that the ECCD contribution to the current profile is not chosen to cancel the BC everywhere, but peaks

at 1/4 to 1/3 of the plasma volume which can be seen in Fig. 5. This precludes parasitic edge heating. The ι-profiles corresponding to the different currents are displayed in Fig. 6. At $< \beta > \simeq 4.5\%$, the ι-profile near the edge remains close to unity for weak counter ECCD ($2\pi J(1) = -285kA$). When the ECCD globally compensates the BC, the edge-ι drops below 0.95 and for the case of overcompensation ($2\pi J(1) = +45kA$) the edge-$\iota \simeq 0.93$.

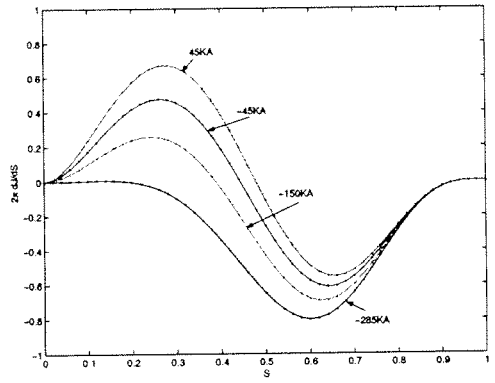

Fig. 5. Analytic toroidal current profiles that model the combination of BC and counter ECCD.

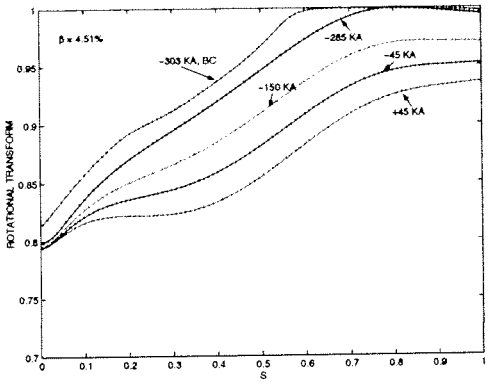

Fig. 6. The ι-profiles corresponding to the toroidal current and current profiles of Fig. 5 at $< \beta > \simeq 4.5\%$. For reference, the profile of the selfconsistent BC ($-303kA$) case is also shown.

The global external kink mode dominated by the $m/n = 1/1$ component is stabilised by the counter ECCD and the corresponding reduction in the edge rotational transform such that marginal stability conditions are achieved when the total current $2\pi J(1) \sim +40kA$. The unstable eigenvalue as a function of the toroidal current is shown in Fig. 7. The perturbed energy associated with $\boldsymbol{j} \cdot \boldsymbol{B}/B^2$ that drives the global kink mode decreases in magnitude (in absolute terms) with increasing counter ECCD (Fig. 8).

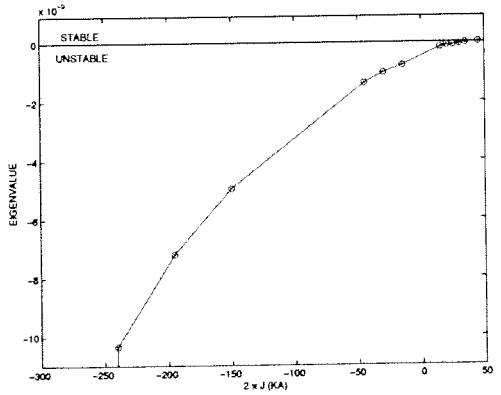

Fig. 7. The unstable global ideal MHD eigenvalue as a function of the toroidal current in a 4-period Helias reactor at $< \beta > \simeq 4.5\%$ for a model current profile that combine the vbootstrap current with counter ECCD.

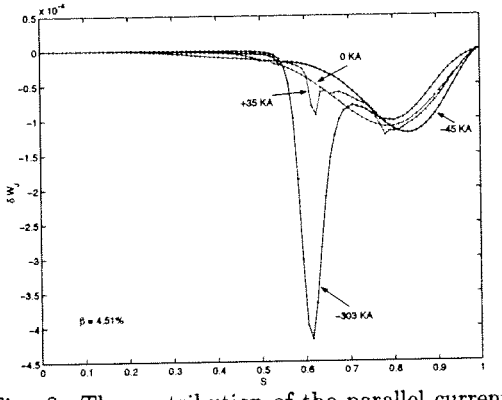

Fig. 8. The contribution of the parallel current drive δW_J to the perturbed energy at $< \beta > \simeq 4.5\%$ for model current profiles of $-45kA$ and $+35kA$, for the selfconsistent BC case ($-303kA$) and for vanishing current.

Wall stabilisation of the global kink modes has been investigated with a closely fitting conducting shell in which the average wall radius can approach the plasma within 1% (Fig. 9). For the equilibrium with selfconsistent BC at $< \beta > \simeq 4.5\%$, the unstable

eigenvalue can be reduced by a factor of three with the closely fitting shell without achieving stability. For the model toroidal current profile of BC partially compensated by ECCD with $2\pi J(1) = -150kA$, a wall to plasma diameter ratio of about 1.09 is required to achieve marginality, as shown in Fig. 10.

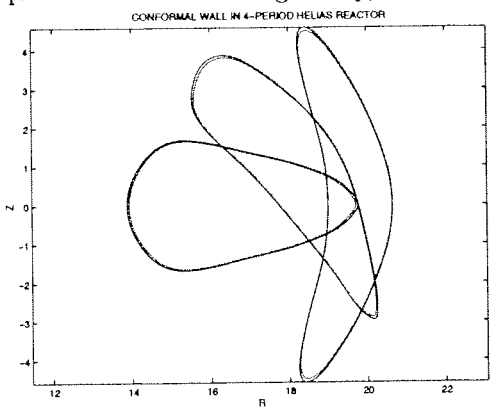

Fig. 9. The plasma-vacuum interface of a free boundary 4-period Helias reactor equilibrium at $< \beta > \simeq 4.5\%$ (in red) and a nearly conformal model conducting shell (in blue).

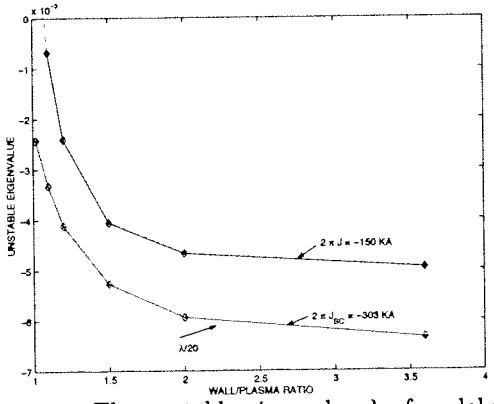

Fig. 10. The unstable eigenvalue λ of a global external kink mode in 4-period Helias reactor equilibria at $< \beta > \simeq 4.5\%$ with a selfconsistent bootstrap current ($-303kA$) and with a model toroidal current of $-150kA$.

In summary, converged selfconsistent bootstrap current profiles computed in the collisionless $1/\nu$ regime in a 4-period Helias reactor cause a slight outward shift and elongation of the plasma column as $< \beta >$ is raised from 0 to 4.5%. The most significant impact of the BC is on the rotational transform profiles which becomes flat and approaches unity in the outer 20% of the plasma volume at $< \beta > \simeq 2.5\%$ and extends to the outer 40% at $< \beta > \simeq 4.5\%$. This destabilises the Mercier criterion and global external $m/n = 1/1$ kink modes and underscores the relevance of rotational transform profile control. Thus, a sequence of equilibria with a polynomial toroidal current profile that models the combination of BC and ECCD demonstrates that with mild ECCD overcompensation (toroidal current varied from $-300kA$ to $45kA$), the edge rotational transform is decreased from unity to about 0.93 at $< \beta > \simeq 4.5\%$ to stabilise the external kink mode. The analysis of the various contributions to the energy principle reveals that 1) the parallel current density dominates the $m/n = 1/1$ energy perturbation, 2) the direct effects of the BC and the ballooning/interchange perturbed energy are weak and 3) the BC alteration of the Pfirsch-Schlüter current constitutes the dominant driving mechanism. A closely fitting shell decreases the growth rate of the external mode by a factor of 3 for the selfconsistent BC case at $< \beta > \simeq 4.5\%$. For the model $-150kA$ toroidal current case that combines BC and counter ECCD, a wall to plasma ratio ~ 1.09 suffices to stabilise the mode.

Acknowledgments Computations in this work have been performed on the NEC-SX5 platform at the Centro Svizzero di Calcolo Scientifico. We thank Dr. S. P. Hirshman for use of the VMEC code. This work was partly supported by Euratom and the Fonds National Suisse pour la Recherche Scientifique.

References

[1] C. D. Beidler, E. Harmeyer, F. Herrnegger, Yu. Igitkhanov et al., Nucl. Fusion **41**, 1759 (2001).
[2] S. P. Hirshman, W. I. Van Rij, P. Merkel, Comput. Phys. Commun. **43**, 143 (1986).
[3] D. V. Anderson, W.A. Cooper, R. Gruber, S. Merazzi, U. Schwenn, Int. J. Supercomp. Appl. **4**, 34 (1990).
[4] J. L. Johnson, K. Ichiguchi, Y. Nakamura, M. Okamoto et al., Phys. Plasmas **6**, 2513 (1999).
[5] W. A. Cooper, Y. Narushima, K. Y. Watanabe, K. Yamazaki, C. Suzuki, S. Okamura, JPFR SERIES **6** (2004) in press.

Inductive Current Perturbations to Steady-State eITBs

T.P. Goodman, R. Behn, A. Bottino, S. Coda, E. Fable, M.A. Henderson, P. Nikkola O. Sauter, C. Zucca

Centre de Recherches en Physique des Plasmas,

Association EURATOM-Confédération Suisse, EPFL, CH-1015 Lausanne, Switzerland

Abstract

Dedicated experiments in which co- or counter- inductive-current *perturbations* were added to an electron internal transport barrier (eITB), created in a plasma fully sustained by non-inductive electron cyclotron current drive (ECCD), show that the barrier location remains stationary while the barrier strength can be either decreased or increased, respectively, at constant EC power input and fixed aiming. There is negligible power and momentum input from the inductive perturbation. GLF23 simulations show that the growth rate of trapped electron modes can be greatly reduced in the core region near the minimum of the weakly reversed q profile used to describe the eITBs. These results show that eITBs can be formed by changing the current profile alone

Introduction

In TCV eITBs are created during the current flat top of a plasma discharge. Target plasmas are created at t=0s and formed during ~100ms to a shape with $\kappa \sim 1.5$, $\delta \sim 0.2$, $I_p \sim 100$kA and $q_{95} \sim 5$-6 and $n_e \sim 10^{19} m^{-3}$. The L/R time of these low temperature plasma (Te ~ 1keV) is ~ 0.23s with roughly 35% of the total inductance coming from the internal inductance of the plasma. At t=0.4s, 70kA of co-ECCD is driven at $\rho \sim 0.4$; 20ms later, the current in the Ohmic transformer is feedback controlled to a constant value thereby removing the external inductive EMF. Although the power is absorbed off-axis, cross-field diffusion of the heated electrons transports co-current to the center of the plasma column [1]. The measured driven current $I_{cd} = I_p - I_{bootstrap}$ is 1 to 3 times the value calculated with the (linear) TORAY-GA ray-tracing code. EC power is then injected into the plasma and absorbed at a location closer to the plasma center than that of the off-axis EC beams. This is referred to here as "central" deposition even though it is not necessarily near the magnetic axis. The beam(s) can be injected with a toroidal angle to produce Doppler-shifted absorption, thus ECCD. The driven current can be either in the same (co-) or opposite (cnt-) direction as the initial inductive current.

With this methodology we routinely produce eITBs in TCV which last up to 2000 times longer than the electron energy confinement time τ_{Ee} [2] even when τ_{Ee} is already ~3-5 times longer that expected from TCV L-mode scaling (Rebut-Lallia-Watkins scaling). We quantify the improved confinement using an $H_{RLW} \equiv \tau_{Ee} / \tau_{RLW}$ factor. An $H_{RLW} = 4$ ($H_{ITER\text{-}98.L} \sim 1.6$) has been obtained in steady-state [3, and references therein].

In this contribution we discuss the confinement and barrier properties in a series of experiments in which perturbative inductive current is added to pre-existing eITBs in either the co- or counter- direction.

Background

In eITBs the barrier is characterized quantitatively using the maximum in $\rho^*_T \equiv \rho/L_T$, the same quantity used for ITB detection on JET [4], where ρ is the ion Larmor radius calculated at the sound speed and L_T is the electron temperature-profile scale length.

The three basic parameters of the EC system which control the current profile, thus the barrier, in non-inductive steady-state discharges are the injected powers P, the toroidal injection angles ϕ, and the deposition locations of the individual EC beams in minor radius $\rho_{co,cnt}$. The electron density n_e can also be changed thereby altering the current drive efficiency. Previous experiments have shown [5] that increasing ρ_{co} at constant input powers and toroidal angles causes the barrier to expand, encompassing more plasma volume. At the same time, the strength of the barrier increases (i.e. the maximum value of ρ^*_T, proportional to the temperature gradient, increases). On the other hand, increasing the central counter-ECCD by means of the toroidal injection angle, increases the barrier strength while increasing the central co-ECCD reduces the barrier strength. In both cases the barrier location remains roughly unchanged. Combining these 2 control parameters, ρ_{co} and ϕ, allows independent control of both the barrier location and strength.

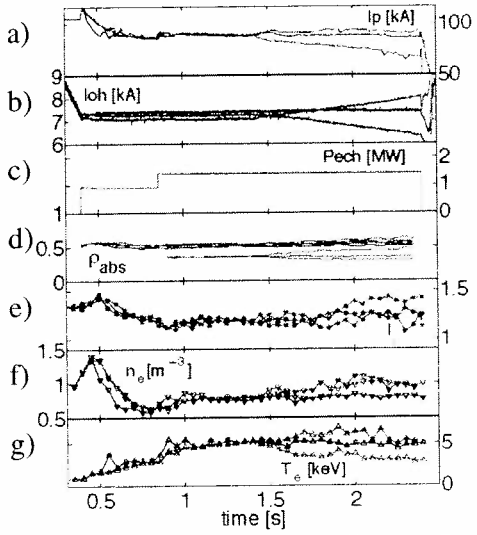

Fig. 1 Time traces of (top to bottom) plasma current, transformer current, EC Power, EC deposition radius, internal inductance, electron density and electron temperature, for 3 shots in which co- (green), zero (blue), and counter- (red) current is driven by very small loop voltage in an established non-inductive eITB discharge (see text).

Experiment

Feedback control of the tokamak transformer current ramp-rate $\Delta I_{OH}/\Delta t$ (i.e. the source of the external loop voltage) provides an additional actuator. In TCV, negative (positive) transformer current ramp rates produce co- (counter-) current, defined as for ECCD. During normal I_p feedback, this ramp-rate is adjusted by the feedback loop to produce a desired I_p regardless of changes in conductivity. In the experiments described here the transformer current I_{OH} is feedback controlled to a given value or ramp-rate and the I_p evolves according to the imposed EMF, plasma conductivity, internal ECCD sources, and the

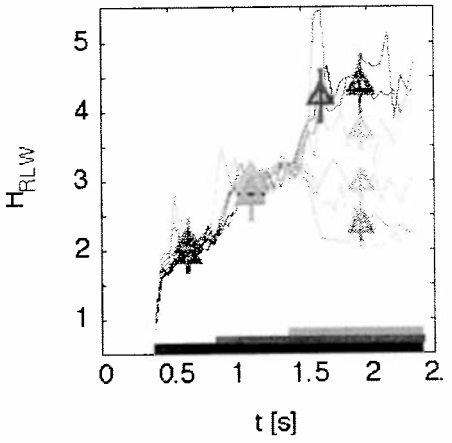

Fig. 2 H_{RLW} factors for a series of shots in which inductive current perturbations are added at 1.4s. Confinement degrades with co-inductive current and improves with counter-inductive current relative to the heated eITB level of $H_{RLW} \sim 3$.

bootstrap current generated by the confinement-dependent pressure gradient. The ramp rates are fixed at values up to an order of magnitude smaller than those resulting from typical *Ip* feedback. The additional power input to the plasma by the EMF source is negligible (a few kW) while the driven current can be significant. This is therefore a perturbative current drive method from the point of view of power input; whereas, adding central ECCD always implies adding significant EC power simultaneously (typically 500kW).

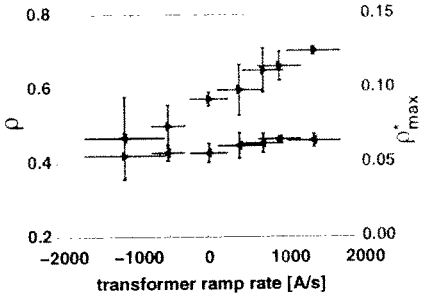

Fig. 3 The barrier strength (green) and location (blue) for a the same 7 shots as figure 2. A ramp rate of 1000A/s corresponds to a loop voltage of 64.5mV in steady-state. These results are very similar to previous scans of the ECCD launch angle. Thus, the H_{RLW} increases due to an increase in the barrier strength resulting from a decrease in the central current density and an increase in the bootstrap current off-axis near the barrier. The barrier location remains roughly constant.

Three shots from a scan with inductive current perturbations are shown in Fig. 1. A standard 100kA (1a) non-inductive eITB is formed by off-axis co-ECCD at 0.4s followed by central EC heating at 0.85s. An inductive current perturbation is added 0.55s later at 1.4s (1b). The absorption locations (1c) are also seen to move in ρ even though the launch angles are fixed. Furthermore the internal inductance l_i (1d) is altered indicating a change in current profile. The central n_e (1f) increases for both co- or counter- induced currents whereas T_e (1g) increases with counter- and decreases with co-current, as the confinement changes. Although the EC actuators are fixed, the changes in temperature, density and absorption location can affect the co-ECCD.

A scan of the transformer current ramp rates has been made from –2000A/s to +1000A/s, corresponding to a steady-state loop voltage, V_{loop}, scan from –129mV to 64.5mV. The H_{RLW} factors for a series of 7 shots are shown in figure 2. Co- inductive current degrades confinement while counter- inductive current improves confinement and the H_{RLW} factor. Figure 3 shows that with more counter inductive current it is mainly the barrier strength that increases, while the location remains fixed. We conclude that this is due to the current profile becoming more hollow on-axis. This effect on the barrier is the same as found for central ECCD scans and confirms that the confinement improvement seen in those earlier scans is due primarily to the modification of the current profile caused by the ECCD rather than the slight changes in deposition location due to differences in the Doppler-shifted absorption.

As the EMF interacts strongly with the entire electron distribution function, whereas the ECCD interacts mainly in a restricted region of velocity space, the inductive current drive efficiency is high. With co- induced current I_p is maintained but, as the current profile peaks l_i increases. Driving counter-inductive current, the plasma current slowly drops and q_{95} is increasing during the shot. The inductive current contribution can be readily calculated from the loop voltage and conductivity profile assuming flat *Zeff* and steady-state conditions (i.e. flat V_{loop} profile) using quantities averaged from 1.95s to 2.35s (i.e. 0.55s to 0.95s after the start of the applied *EMF)*. However, as I_p is slowly changing, especially for counter inductive currents, a back *EMF* is still present. The database of shots indicates an inductive contribution to I_p of approximately ~0.54kA/mV for co-

inductive current and ~1.0kA/mV for counter-inductive current; clearly the inductive current is particularly overestimated in the counter case and a more detailed analysis is required.

Using a χ_e profile calculated from the measured T_e profile and TORAY-GA EC power deposition profiles taken at 1.4s to define the transport, preliminary ASTRA simulations have been made. An abrupt change in V_{loop} causes a current perturbation which penetrates quickly to the barrier location then more slowly to the plasma center with a characteristic exponential time constant of ~0.26s. After 0.55s the V_{loop} at the plasma center has attained only 2/3 of the steady-state value but the current profile is nevertheless centrally peaked. Future work will include the associated modifications of the transport in the simulations to better follow the experimental situation.

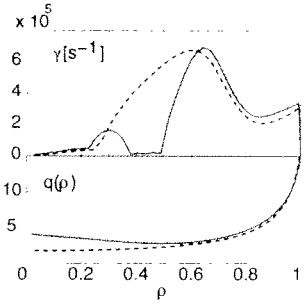

Fig. 4 GLF23 simulations of the growth rate of the most unstable mode as a function of the minor radius for a monotonic (black dashed) and reversed-q (red-solid) profile. Changing only the current profile is sufficient to stongly reduce the growth rate in the plasma core (ρ<0.6) near the q_{min}.

The eITB forms due to the non-monotonic current profile generated by the current profile tailoring. Linear gyrokinetic simulations with the in-house LORB5 code show that the TEM is the most unstable mode. They confirm that there is little influence by the ions. In addition, they show that changing only the q profile can change significantly the TEM growth rate, reverse shear being strongly stabilizing in the region of q_{min} and of the reverse shear.

Figure 4 shows the results of simulations using the GLF23 transport model to calculate the linear growth rates for 2 current profiles – one producing a monotonic q-profile and the other a reversed-q profile. The TEM mode is found to be stabilized for the reversed-q case with a growth rate more than an order of magnitude lower than the monotonic case in the plasma core.

TCV results show that eITBs can result merely from a change in the current profile. In the absence of momentum injection or additional power input, the barriers can be strengthened or weakened while maintaining their position by current profile tailoring alone.

This research was partially funded by the Swiss National Science Foundation.

References

[1] Harvey, R.W. *et al.*, Phys Rev. Lett. **88** (2002) 205001.
[2] O. Sauter, *et al.*, 29th EPS, ECA Vol. **26B**, (2002) P-2.087.
[3] T.P. Goodman, *et al.* Nucl. Fusion **43** (2003) 1619.
[4] G. Tresset, *et al.* Nucl. Fusion **42** (2002) 520.
[5] M.A.Henderson *et al.* PPCF **46** (2004) A275.

Recovery of Ion Parameters from NPA Measurements on TCV

A.N.Karpushov[1], B.P.Duval[1], B.LaBombard[2]

[1] *Centre de Recherches en Physique des Plasmas,*

Association EURATOM-Confédération Suisse, EPFL, 1015 Lausanne, Switzerland

[2] *Massachusetts Institute of Technology, Cambridge, USA*

Introduction. A method to recover the ion temperature profile of TCV plasmas has been developed by modelling the measured energy spectra of the neutral deuterium fluxes varying the parameters of the T_i profile. A Neutral Particle Analyser (NPA) [1,5] is used on the TCV tokamak [2] to measure the energy spectrum of hydrogen and deuterium neutrals escaping the plasma. A Kinetic Transport Algorithm, (KN1D) [3], was applied to obtain neutral density profiles in the bulk plasma. The response of Charge eXchange energy spectra to plasma parameters was examined with a model prediction. Ion temperature profiles, evaluated by this method, were compared with the classical logarithmic CX-spectrum slope evaluation. Results based on analysis of NPA data were also compared with measurements from charge exchange recombination spectroscopy (CXRS) [4].

TCV [2] is a medium-sized tokamak (R=0.88 m, a=0.25 m, $I_p < 1$ MA, $B_T < 1.54$ T, plasma elongation 1-2.8) able to produce a plasma with the central electron density $0.5\text{-}15\times10^{19}$ m^{-3}, an electron temperature over 10 keV with bulk central ion temperatures 0.3-1 keV. A 5-channel NPA, with electrostatic energy separation [1], measures the ion parameters [5-7]. The NPA voltage sweeps the energy channels to measure neutral particle energies in the range of (0.6→6.5 keV), with a time resolution of ≥13 ms viewing the plasma along a vertical chord (fig.1).

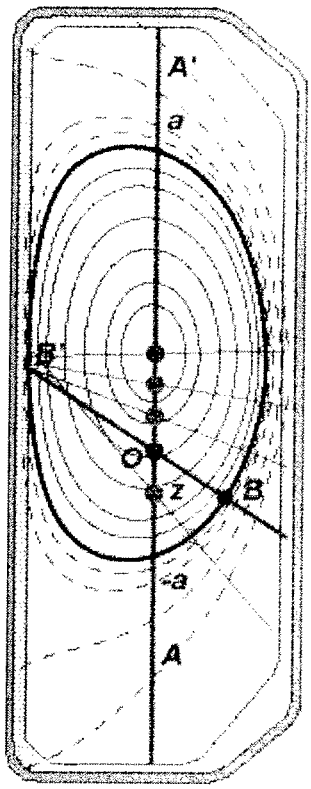

Fig.1: NPA observation geometry. AA' – NPA view line; BB' – chord for 1-D modelling; B – nearest point on plasma boundary for neutral particles calculation in point O.

CX spectrum and ion temperature. The energy spectrum of passive atomic flux ***J(E)*** traversing the plasma surface and entering the external instrument (NPA) is the sum of fluxes in the plasma column along the view line of the analyser [8]

$$J(E) = \Omega \cdot S \cdot \int_{-a}^{a} n_a \cdot n_i \cdot f_i(E) \cdot \left\langle \sigma_{cx}(v_{ia}) \cdot v_{ia} \right\rangle \cdot \exp\left[- \int_{-a}^{z} n_e(z') \cdot \sigma_{abs}(E, z') \cdot dz' \right] \cdot dz , \qquad (1)$$

where $\boldsymbol{\Omega S}$ is the acceptance of the analyser, $\boldsymbol{n_a(z)}$ and $\boldsymbol{n_i(z)}$ are the densities of the atoms and ions, $\boldsymbol{f_i(E,z)}$ energy distribution function of the ions, $\boldsymbol{\langle \sigma_{cx}(v_{ia}) \times v_{ia} \rangle(z)}$ is the rate coefficient for the charge exchange (z is a coordinate along NPA view line).

$\exp\left[- \int_{-a}^{z} n_e(z') \cdot \sigma_{abs}(E, z') \cdot dz' \right] = \gamma_{att}(E, z)$ is an attenuation factor, where $\boldsymbol{\sigma_{abs}}$ is the sum of cross-sections for processes ionising the neutrals as they move from the birth point to the spectrometer.

In our analysis it is assumed that the ion energy distribution is Maxwellian. In this case, for 0-dimensional model (T_i and T_e are constants along NPA view line) and low attenuation (γ_{att}=1), the ion temperature T_i is proportional to the logarithm of the slope of "Charge eXchange spectrum":

$$\frac{E}{T_i}+\frac{3}{2}\ln(T_i) \sim -\ln\left(\frac{J(E)}{\sigma_{cx}(E)\cdot E}\right)=-\ln(F_{dc}) \qquad (2)$$

where the "CX spectrum" (F_{dc}) is defined as $\frac{J(E)}{\sigma_{cx}(E)\cdot E}$.

In most situations, the plasma does not exhibit a single ion temperature and the attenuation factor may not be neglected so the ion temperature, inferred from the slope of (F_{dc}), depends on the energy:

$$\frac{1}{T_i^{NPA}(E)}=-\frac{d\ln(F_{dc})}{dE} \qquad (3).$$

In this work, the ion temperature profile is parameterised by the functional form:

$$T_i(\rho)=(T_i(0)-T_i(1))\cdot(1-\rho^2)^{kTi}+T_i(1) \qquad (4)$$

to minimise the difference between measured $\ln(F_{dc}{}^{NPA})$ and expected $\ln(F_{dc}{}^{calc})$ based on equations (1) and (2). The fitted parameters are on-axis ($T_i(\rho=0)$) and edge ($T_i(\rho=1)$) ion temperatures and ion temperature profile peaking (kTi).

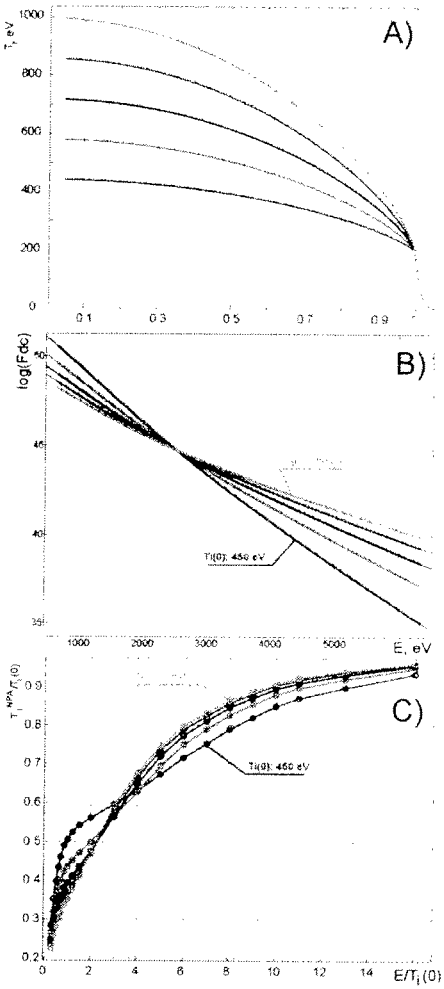

Fig.2: Central ion temperature scan (quasi-experiment). A) input ion temperature profiles; B) "CX-spectrums"; C) $T_i^{NPA}/T_i(0)$ ratios.

Model for neutral density. Energy spectra of neutral fluxes escaping plasma along an observation chord and measured by an NPA depend on the temperature and density profiles of the ions and electrons as well as on the density profile of the neutrals (1). Electron density and temperature profiles are available on TCV from Thomson scattering. A 1-D Space, 2-D Velocity, Kinetic Transport Algorithm for Atomic and Molecular Hydrogen in an Ionising Plasma (KN1D) [3], adapted for TCV, was applied to obtain a neutral density profiles in the plasma. This code offers a numerically rapid access to a neutral density profile as compared with Monte-Carlo codes (like EIRENE [9]) that are not routinely available on TCV, and thus permits an examination of the expected NPA behaviour for a wide range of plasma parameters.

The mean free path of "wall" neutrals in TCV plasmas is significantly smaller than a plasma minor radius ("optically thick plasma"). Thus, the main contribution to the neutral density comes from the neutrals moving over the shortest distance to the plasma boundary (BO line in fig.1). This justifies the use of a one-dimensional slab model for the calculation of the neutral density along the diagnostic chord (AA') in the plasma. We use a constant neutral molecular density outside the plasma as a boundary condition for the neutral density profile calculation. An example of atomic hydrogen neutral density profile calculation along NPA view line is shown in fig.3(B).

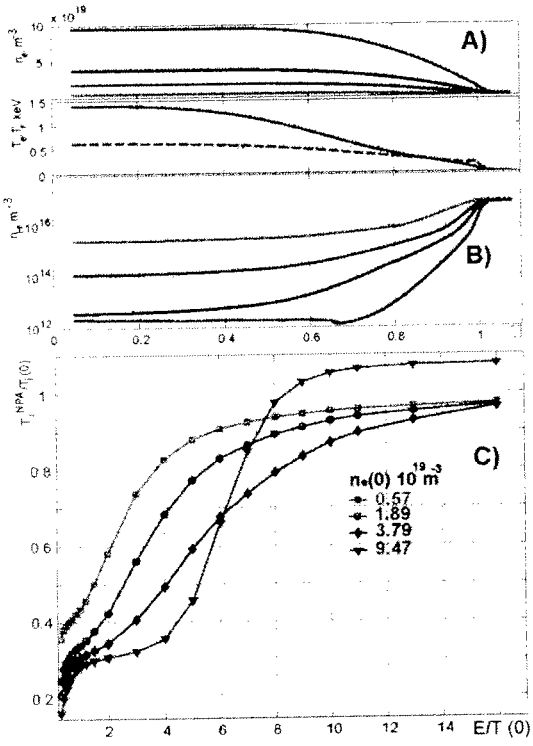

Fig.3: Plasma density scan. A) density, electron and ion temperature profiles; B) neutral density; C) $T_i^{NPA}/T_i(0)$ ratios.

CX spectrum response to plasma parameters. A quasi-experimental method is used to study response of CX spectrum on plasma parameters. In this method we calculate $J(E)$, F_{dc}^{NPA}, $T_i^{NPA}(E)$ for some chosen profiles of plasma parameters ($n_e(\rho)$, $T_e(\rho)$ and $T_i(\rho)$) and boundary condition (neutral molecular pressure outside plasma). It was found that "CX-spectrum" is very sensitive to the central ion temperature ($T_i(0)$ see fig.2(B)). For "passive" NPA measurements, an ion temperature (T_i^{NPA}) calculated on a fitted "NPA CX-spectrum" (fig.2(C)) is lower the actual central ion temperature ($T_i(0)$), except for high density plasmas where the recombination term in neutral density dominates (fig.3). For the NPA energy range $4\text{-}7\ T_i(0)$ the $T_i^{NPA}/T_i(0)$ ratio ranges from 0.5 to 0.9, increasing with decreasing plasma density and/or the ion temperature peaking factor. The $T_i^{NPA}/T_i(0)$ ratio strongly depends on the line integral of the plasma density (fig.3). The high energy tail of the CX-spectrum is dominated by plasma central region, and low energy part by the plasma edge (fig.4). This separation is stronger for high plasma density. The response of $T_i^{NPA}(E)/T_i(0)$ ratio to plasma density peaking, ion end electron temperature profiles for NPA energy ($E>3\ T_i(0)$) is less then 10% for the considered TCV experimental conditions.

T_i profile recovery for TCV plasmas. We use the following iteration procedure to recover a T_i profile from the NPA measurement: firstly, the neutral density profile was calculated by KN1D code from the experimental electron temperature and density profiles and an empirical approximation for ion temperature profile based on the NPA measurement. The ion temperature profile parameters were recovered from a minimisation of discrepancy functional (Ψ) between the model and experimental spectra. Ψ characterises the "goodness-of-fit" of the model:

$$\Psi = \left\langle \left| \ln\left(F_{dc}^{NPA}(E_k)\right) / \ln\left(F_{dc}^{calc}(E_k, T_i(\rho))\right) - 1 \right| \right\rangle_k , \quad (5)$$

where index k runs over all experimental energy points, F_{dc}^{calc} is the model function calculated according (1) for experimental ($n_e(z)$ and $T_e(z)$) and $n_a(z)$ from neutral transport code). A recovered ion temperature profile was used for the new neutral density profile of the next iteration. 2-3 iterations were usually sufficient to obtain a stable solution.

An example of T_i recovery is shown in fig.5. Recovered profiles are in a good agreement with carbon (C^{IV}) T_i profiles measured by CXRS technique. The discrepancy

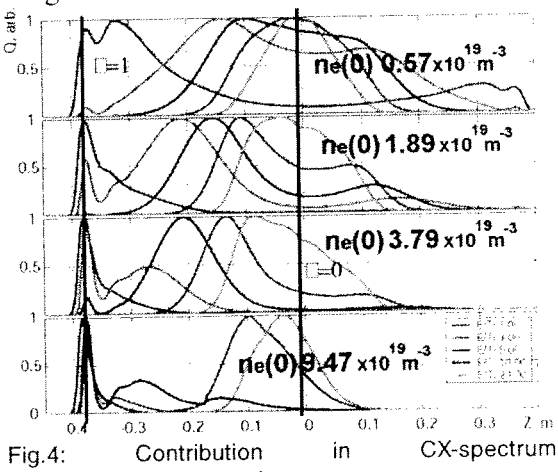

Fig.4: Contribution in CX-spectrum ($n_a \cdot n_i \cdot f_i \cdot \langle \sigma_{cx}(v_{ai}) \cdot v_{ai} \rangle \cdot \gamma_{att}$). Red – E=$T_i$(0); cyan – E=20$T_i$(0). See fig.3(A) for input profiles.

function (Ψ) has strong dependence on central ion temperature, $T_i(0)$ and can usually be recovered with accuracy of ~10% (fig.6). We expect errors for edge temperature ($T_i(\rho=1)$) and peaking (kTi)) in the range of 30-70%.

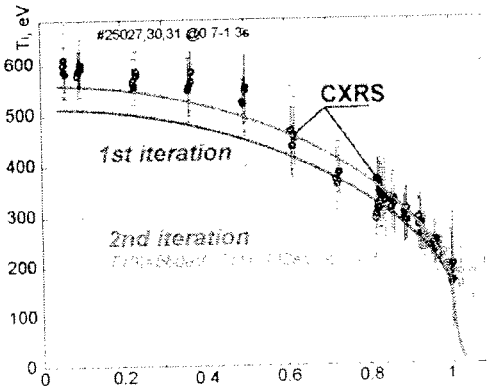

Fig.5: Ion temperature profiles, recovered from NPA measurement and CXRS.

Conclusions and discussion.

- A method of ion temperature profile determination from NPA CX measurement has been developed.
- For the ohmic phases of TCV plasma discharges, without neutral beam (DNBI) injection, $T_i^D(\rho)$ profiles are in a good agreement with CXRS measurements of carbon impurity temperature $T_i^{CVI}(\rho)$.
- A flexible computed algorithms for $T_i(\rho)$ recovery has been constructed.
- KN1D (Kinetic Transport Algorithm for Atomic Molecular Hydrogen) has been adopted for TCV.

The algorithm for T_i profile recovery was developed assuming a Maxwellian ion energy distribution function. A non-Maxwellian ion energy distributions (with a significant fraction of suprathermal ions) has been observed in low density TCV discharges with ECH. In such discharges a high-energy tail of CX spectrum is dominated by suprathermal ions [6].

An important limitation of described method is in the registration statistics of neutrals with energies high than $10T_i(0)$. The approximation of homogeneous neutral hydrogen molecule pressure outside plasma is not sufficient for some plasma discharges with limiter configuration. A 2-D space neutral transport calculation is required to provide a better answer to this question.

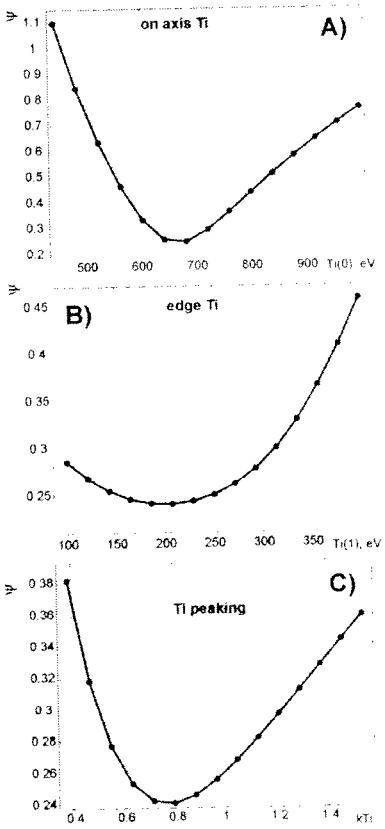

Fig.6: Dependences of discrepancy functional on parameters of ion temperature profile.

1. V.V.Afrosimov et al., *Sov. Phys. - Tech. Phys.* **20**(1), (1975) 33 http://www.ioffe.rssi.ru/ACPL/npd/npa01.htm
2. T.P.Goodman et al., Proc. 19th IAEA Fusion Energy Conf., Lyon, France, 2002 (IAEA, Vienna, 2002), CD-ROM file OV/4-2.
3. B.LaBombard, "KN1D", PSFC Research Report: PSFC/RR-01-03, MIT, Cambridge (2001)
4. P.Bosshard et al., 29th EPS Conf. PPCF, Montreux, ECA **26B** (2002) P-4.120.
5. A. Karpushov et al., 29th EPS Conf. PPCF, Montreux, ECA **26B** (2002) P-4.119.
6. A.N.Karpushov et al., 30th EPS Conf. CFPP, St. Petersburg, ECA **27A** (2003) , P-3.123.
7. I.Condrea et al., 29th EPS Conf. PPCF, Montreux, ECA **26B** (2002), P-2.079.
8. V.V.Afrosimov and A.I.Kislyakov: *Neutral Particle Diagnostics of Plasma*, International School of Plasma Physics, Varenna, Italy, Sept. 1982, p.289-310
9. D.Reiter, "The EIRENE Code User Manual", http://www.eirene.de/

This work was partly supported by the Swiss National Science Foundation.

Drift-Free Equilibrium Reconstruction Using Magnetic Probes

J.B. Lister, F. Saint-Laurent[2], Ph. Moreau[2], V. Dokouka[3], R.R. Khayrutdinov[3], V.E. Lukash[4]

Centre de Recherches en Physique des Plasmas, EPFL,
Association EURATOM-Confédération Suisse, 1015 Lausanne, Switzerland
[2]DRFC, Association Euratom-CEA, 13108 Saint-Paul-lez-Durance, France
[3]TRINITI, Moscow Region, Russia
[4]RRC Kurchatov Institute, Moscow, Russia

Introduction: Two sources of magnetic diagnostic drift have been well documented, namely electronic input offset of the integrators, since the fields and fluxes are time-integrals of the voltages from the physical probes, and radiation induced or thermoelectric emf due to neutron bombardment of the mineral insulated cables between the probes and the integrators. Tore Supra has recently demonstrated an additional effect, not previously taken into consideration, which is slight rotation of the magnetic probes by thermo-mechanical distortion during 300 second pulses absorbing more than 1GJ into the plasma, resulting in time-dependent pick-up of the toroidal magnetic field. The Tore Supra control system tracks these offsets and displaces the last closed flux surface from its reference location. This new effect of long high-power pulses has the properties of a drift, generating a slowly evolving unmeasured offset to the integrated magnetic signals. For this reason, we have decided to take another look at methods of reconstructing an offset-free equilibrium from magnetic diagnostics, whereas most proposed approaches to drift compensation rely on non-magnetic, non-integrated measurements of plasma emission or reflectometry. We note that a similar approach was tested on HT-7 [1] using the induction in the Poloidal Field (PF) coils as the sole measurement of the radial position, modulating in a similar way. Although this present work uses magnetic diagnostics, we are extending this idea to include the vertical position and the deformation of highly shaped plasmas.

Auto-calibration principle: An equilibrium flux surface plot shows that if we marginally displace an equilibrium, the change to the flux-loop signals depends on the curvature of the local flux surface at the loop. A loop which is placed at the tangency point for a given displacement direction will see no change, whereas either side will see a change of different sign. Modulating the position of the equilibrium in both directions, and the plasma current itself, therefore adds new information to that available from the probes for a static equilibrium. Modulating the equilibrium position is different from sweeping the probe position and does not directly give the local flux gradients. The changes of the PF coil currents, shell currents and deformation of the equilibrium itself must be taken into consideration. The changes to the signals are well modelled by a variety of linear and nonlinear models already extensively validated as part of plasma equilibrium control research. However, we can more easily use the tokamak itself to auto-calibrate the sensitivity, which is the first approach made in this paper. It is necessary to explicitly modulate the plasma current, since modulating the plasma radius modulates the current (and vice versa) and it is vital to separate these two effects.

The auto-calibration method proceeds step-wise, briefly summarised as follows for the particular case of TCV control and TCV diagnostics:

a) programme the reference waveforms so the plasma "wanders" over a range of interest;

b) modulate the geometry triplet [RI_p, ZI_p, I_p] (*RZI*) references at three frequencies;
c) run a full tokamak plasma discharge, or a full plasma simulation;
d) demodulate *RZI* using the three known frequencies, an offset and a drift, for short time-segments;
e) similarly demodulate all 76 magnetic diagnostics S_j (38 poloidal flux and 38 tangential poloidal field probes), to provide the 76*3 sensitivity matrix $Q_{jk}=dS_j/dRZI_k$;
f) identify the contributions of each element of *RZI* to the diagnostic modulation via an inversion of the *RZI* modulation triplet at the 3 frequencies in the same time-segments;
g) take all the time-segments and regress all 228 elements Q_{jk} to the mean values of [R,Z] in the time-segments to obtain an "auto-calibration" mapping M so that [R,Z] = $M(Q)$.

Auto-calibration test in TCV geometry: In a first test, we took the extreme case of the TCV tokamak, in which the PF coils are close to the probes and in which the vacuum field is spatially highly structured for strong plasma equilibrium shaping. The self-calibration method was tested on simulation data generated by the 1.5D simulation code DINA-CH [2] and the results were encouraging, demonstrating that the magnetic probe modulation response when the triplet *RZI* is modulated can be roughly linearised as a function of the plasma position with a potentially useful noise sensitivity.
A number of important details were identified this first attempt which led to a second simulation with slightly different modulation frequencies and amplitudes to obtain a more diagonal and better conditioned 3x3 *RZI* matrix:

a) We are extracting the modulation amplitudes of RZI at three frequencies and then inverting the modulation of the three geometrical variables, which is inconsistent, since the modulation response is itself a function of frequency; out of precaution, we use frequencies as close as possible for modulating R and Ip, which provide the main cross-coupling; if the response is in the 1/f regime, the integrated quantities are roughly constant as a function of frequency; the problem will lie in the lower frequencies;
b) Estimating the modulation of [R,Z] from probes with unknown offsets is justified by their corresponding Shafranov integrals being known to be linear in the magnetic diagnostic measurements;
c) A crucial point is the propagation of noise or errors onto the raw signals thereby to the modulation amplitudes and to the estimate of the position, which we discuss in more detail; in order to guarantee a reliable mapping M between the modulation sensitivity Q_{jk} and the plasma position, we found it necessary to add noise to the simulated raw diagnostic data, and also to generate a large number of samples. In this way, the structure of M was adapted automatically to realistic noise on all diagnostics.

Linear mapping M: The first step was to generate a linear mapping function M. The noise addition was preferred to relying on an SVD truncation to improve the conditioning. Figure 1 shows the quality of the mapping for 3 different noise levels used for generating the mapping and for polluting the data to be analysed. The noise level of the raw diagnostic signal was estimated and used to quantify the added diagnostic noise level The mapping M generated with no added noise is incapable of approximating the plasma position from the Q_{jk} estimated from noisy signals (top right). With 10% of the assumed diagnostic noise level,

the mapping M was reliable when reconstructing the noisier and noise-free data. With 100% of the assumed diagnostic noise level, the mapping becomes sensitive to noise.
The quality of reconstruction of R was inferior to the quality of reconstruction of Z. We attempted different fits to the position information, including cross-terms RZ and quadratic terms R^2. We have been unable to satisfactorily explain this difference. Potential causes include:

a) stronger coupling due to approximate poloidal flux conservation (but we tried several other combinations);
b) non-linearities during the inside-outside limiting of the plasma, although we found no increase in the residuals for the extrema in R;
c) small range of equilibria from which to extract the linearised dependence; this is inevitable due to the proximity of the separatrix to the wall.

Non-linear mapping to the R and Z positions: In view of this initially encouraging but ultimately disappointing result for finding a suitable linear mapping, we generated a simple non-linear mapping using a one hidden layer Multi-Layer Perceptron mapping which provides a universal mapping between two spaces, in this case the 228 modulation amplitudes to the single variable R or Z, a method previously used and described for the case of equilibrium mapping [3]. Using noise-free data led to a less noise sensitive map than the pseudo-inverse, due to the slow convergence to a solution with negligible improvement to the fit, seen in Fig.2. However, learning with itermediate noisy data still led to a better reconstruction of the very noisy data, and we assume to a good reconstruction of the noise-free data. The results are expressed in Table 1. The reconstruction is never performed on the learned data sample. Each condition is shown for a mapping generated with 2 and 4 neurons in the hidden layer.
The most realistic assumption is shown in bold face in the table, corresponding to 10% noise added to the learned data and 0% noise added to the measured data to be reconstructed. The resulting residuals are 1.0 to 1.3mm for R and Z respectively, obtained with 2 neurons in the hidden layer. The cases with 4 neurons suffer from over-learning with a number of examples too close to the number of free parameters in the mapping, already 559 with 2 neurons.

Learned noise level	Neurons	Reconstructed with 0% noise		Reconstructed with 10% noise		Reconstructed with 100% noise	
		R [mm]	Z [mm]	R [mm]	Z [mm]	R [mm]	Z [mm]
0%	2	0.88	1.07	2.3	2.4	16.7	20.5
	4	0.84	1.04	2.2	3.1	17.2	27.8
10%	2	**1.0**	**1.3**	1.3	1.8	7.4	11.0
	4	0.9	1.2	1.3	1.7	7.6	13.3
100%	2	2.4	5.2	2.4	5.1	5.1	8.4
	4	3.1	5.5	3.2	5.8	6.5	11.7

Table 1. Residuals using a 1-hidden layer neural network [mm]. Columns are the noise level in the reconstructed data and the rows refer to the noise level in the learned data.

Effect of changing the equilibrium: These results provide the basis for confidence that the position of a given equilibrium can be reliably estimated from the modulated components. The question of sensitivity of the mapping M to changes in beta and li has to be addressed and the simulations have already been run to be analysed in the near future.
Noise level in the measured signal and required modulation amplitude: We selected 0% noise on the data for testing the quality of the reconstruction. This is justified by the

reduction of the noise level for a given amplitude modulation by the square root of the modulation duration. The signal level is proportional to the modulation amplitude. We can therefore always increase the signal-to-noise level for a given tolerable amplitude by reducing the bandwidth of the new measurement. Since we are only trying to compensate drift, in principle extremely low frequency, this bandwidth will be extremely low. The modulation should be continuous stimulation, rather than pulsed stimulation, for the same reason, since the signal-to-noise of the modulated component varies as $\sigma \sim A\ \mathrm{sqrt}(\Delta t)$ where A is the amplitude of the modulation and Δt is the duration of the stimulation. Initial experiments have already been carried out on Tore Supra in a simplified form of the auto-calibration method, but the results illustrate the noise sensitivity and show clean demodulated strengths, but with fairly large modulation amplitude.

Application to ITER: Assuming superposition of the noise, the error on the modulation will diminish with the square-root of the demodulation window duration. The demodulation itself also improves by increasing the duration since the conditioning of the fit to the known frequencies improves as the number of complete cycles increases.

AC losses will increase linearly with the duration of the modulation and the coupling losses will increase with the square of the amplitude and the square of the frequency, $P_{AC} \sim A^2\ \omega^2 \Delta t \sim \sigma^2 \omega^2$. We assume that the modulation is sufficiently small that the hysteresis losses will be negligible. This relationship illustrates that the AC losses are minimised for a given signal-to-noise ratio by low modulation frequencies, but are independent of the mark to space ratio of the modulation, unlike the signal-to-noise ratio itself.

Model based calibration: An alternative approach, for the moment a gedanken approach, might be to take a validated plasma equilibrium response model for a given equilibrium, to calculate the closed loop responses of the diagnostics and position to any imposed voltage modulation $S_j(j\omega) = H(j\omega)\ U(j\omega)$ and to derive the same modulation sensitivities Q_{jk} for the nominal position. The response is then recalculated over a grid in [R,Z] and the same procedure followed by analogy. The fundamental approach can then be restated as finding combinations of the [R,Z] dependence of some of the transfer functions which are sensitive to [R,Z]. Considering the problem in this way illustrates some of the weaknesses and strengths. The first assumption is linearity of the diagnostic response, well established experimentally. The next assumption is that this linearity varies with position over short ranges, roughly a local linearisability of the Green's functions. On the negative side, when we divide by the position modulation, we are assuming rough independence of $H(j\omega)$ on $j\omega$, which applies carefully choosing the frequencies for a region in which the responses are flat or implying close frequencies.

Acknowledgements: This work was partly supported by the Fonds national suisse de la recherche scientifique.

References

[1] K.Nakamura, Z.I.Ji, B.Shun, P.QW.Qin, S.Itoh, K.Hanada, M.Sakamoto, E.Jotaki, M.Hasegawa, A.Iyomasa, S.Kawasaki, H.Nakashima, Fusion Engineering and Design 66-68, 767-770 (2003)

[2] Khayrutdinov R.R., Lister J.B., Dokouka V., Duval B.P., Favez J.-Y., Lukash V.E., Raju D., Proc. 30th EPS Conference on Controlled Fusion and Plasma Physics, St Petersburg, Russia, 2003, ECA Vol. 27A, P-3.163

[3] Lister J.B., Schnurrenberger H., Nucl. Fusion 31(7), 1291 - 1300 (1991)

Evolution of the DINA-CH tokamak full discharge simulator

V.E. Lukash[2], J.B. Lister, V. Dokouka[3], R.R. Khayrutdinov[3], B.P. Duval, J-M. Moret, J-F. Artaud[4], V. Baziuk[4], M. Cavinato[5]

Centre de Recherches en Physique des Plasmas, Association EURATOM-Confédération Suisse, EPFL, 1015 Lausanne, Switzerland
[2]RRC Kurchatov, Moscow, Russia
[3]TRINITI, Moscow Region, Russia
[4]DRFC, Association Euratom-CEA, 13108 Saint-Paul-lez-Durance, France
[5]Consorzio RFX, Associazione Euratom-Enea per la fusione, Padova, Italy

DINA-CH development path: Developing a full tokamak discharge simulator will be essential for ITER. The work carried out using the DINA-CH code, a version of DINA adapted to function in an open-architecture model using the Matlab Simulink environment, provides a test-bed for the future continued development of such a tool. In previous presentations, DINA-CH was demonstrated for plasma equilibrium response modelling in TCV, ITER and MAST, ECH/ECCD modelling in TCV. VDE modelling in TCV was validated in a previous DINA version. Following the initial work carried out using DINA, the control modelling of DINA was removed from the DINA source and implemented in the open-architecture SIMULINK environment. Heating sources were removed and similarly implemented. Finally, transport which had been modelled in DINA was also implemented as an external module. The principle of opening DINA up to interface to more existing devices and more simulation codes has given rise to DINA-CH, which simulates TCV, ITER, MAST and (most recently) ASDEX-UG, all using the same core executable module and the same interface.

Latest applications using DINA-CH: We have used DINA-CH to develop an auto-calibration of the plasma position in the presence of unknown diagnostic drifts in TCV, by modulating the plasma position and current, and allowing the plasma to drift around the [R,Z] plane. This work is fully described in an accompanying paper [1]. Since this simulation requires the dynamics of the plasma movement in the vessel, including the full control circuitry, only a code such as DINA-CH or TSC can be used.

We have now implemented a diagnostics toolbox [2] to simulate the functioning of diagnostics of the free-boundary evolution of a TCV tokamak discharge, implementing the

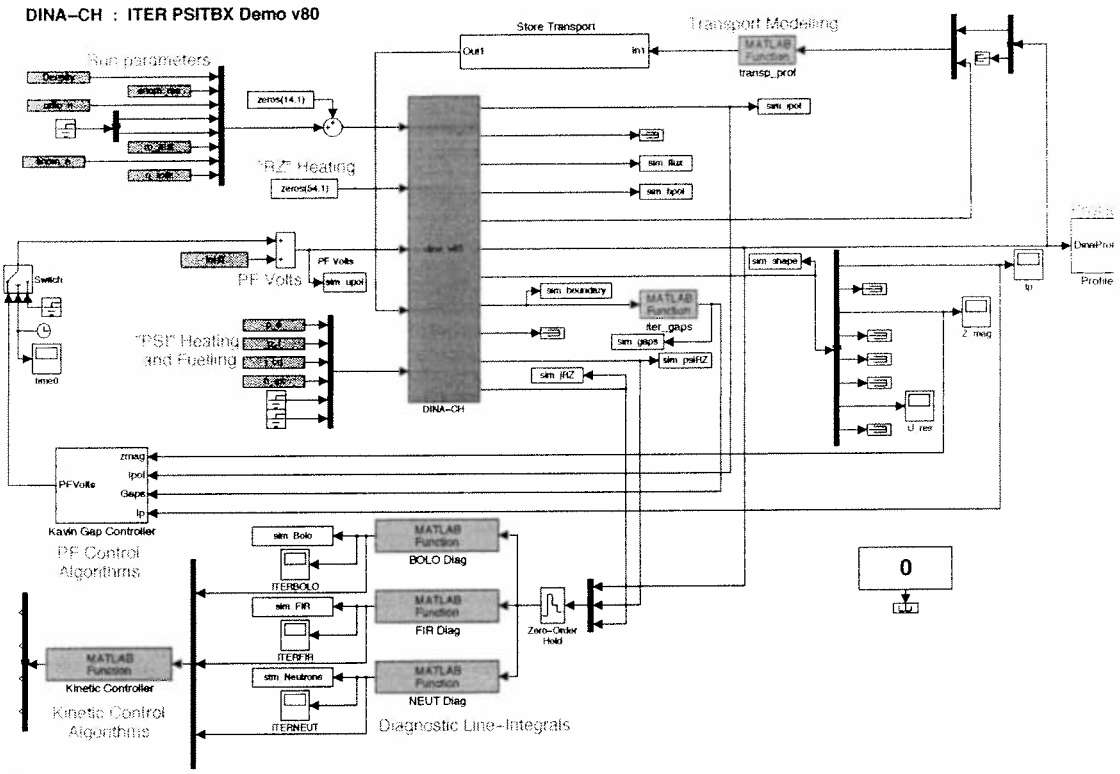

Fig.1 Implementation of the diagnostic toolbox (PSITBX) for simulating two diagnostics in the ITER tokamak.

MPX diagnostic and an interferometer. This step now brings us to the point where we can model the use of diagnostic information to generate kinetic control feedback loops. Figure 1 shows how this diagnostic toolbox is simply connected to the outputs of the DINA-CH code, namely the full profile information and the (R,Z) gridded values of the shifted poloidal flux, zero at the last closed flux surface and the (R,Z) gridded toroidal current. By passing an instruction to a general interface, describing the function of the kinetic parameters, the module returns the chord-by-chord line-integral of this quantity, corresponding to a large class of passive diagnostics. Examples of this function implemented for ITER are "ne" to simulate a FIR interferometer,"1e-44 * ne.^2 .* Te.^1.5" to crudely simulate the soft X-ray signal of a multi-wire proportional chamber. The evolution of the profile can be visualised, or acted upon in a feedback loop, during the simulation. The advantage of this toolbox is that it provides a unique definition of a diagnostic, being a set of chords (defined in a single

initialisation call) and a functional dependence on modelled parameters, of unlimited complexity). Full toroidal geometry and even non-axis3metry are handled by this toolbox which functions inside Matlab under the Linux and IBM AIX operating systems [2].

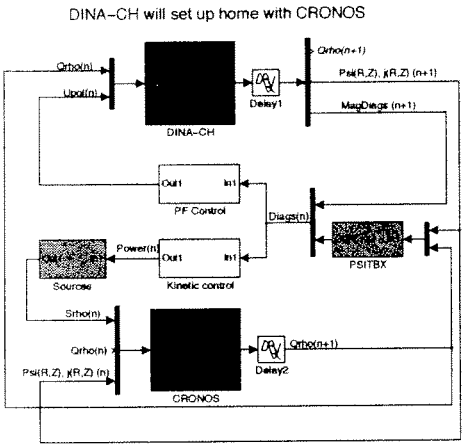

Fig.4 Illustration of the marriage of two solvers, avoiding the development of monolithic codes and drawing upon the strong features of each.

This interface was simply reproduced for ITER, emulating the bolometry diagnostic design and a schematic interferometer and neutron camera, illustrated in Fig.2. During the simulation, the diagnostic data are available as inputs to a kinetic control algorithm controlling the external power sources, shown in Fig.1. Figure 3 shows a time-slice of these ITER diagnostics during a full simulation.

Most recently, we have implemented the ASDEX-UG tokamak under DINA-CH, with a realistic model of the plasma position and current control and a primitive approximation of the plasma shape control algorithm. The aim is to study the recently reported ELM toggling results in an accompanying paper at this conference [3], reproducing the earlier TCV results [4].

Future orientation: The present strength of the DINA code resides in its extensive use and benchmarking for plasma equilibrium response modelling. The DINA-CH modular implementation in a graphical environment has shown considerable flexibility, once the details of a specific tokamak were removed from the core source, allowing all modelling to advance around a single code. This structure allowed the inclusion of additional heating for TCV, and transport modules to be specified externally as well. However, there remains a wealth of codes describing heating sources and transport available and it is pointless to try and redevelop these physics codes. It is essential to provide a simple method for allowing these codes, which generally function in a 1-D representation for transport and a 2-D representation for heating, to collaborate in full DINA-CH simulations.

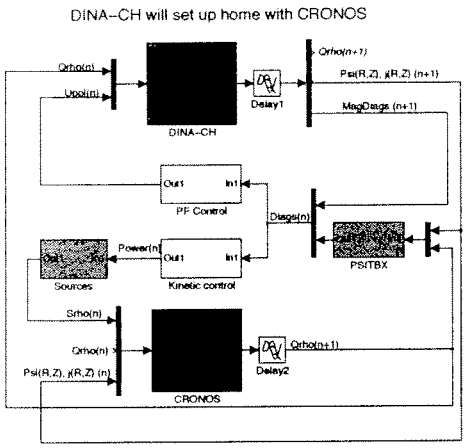

Fig.4 Illustration of the marriage of two solvers, avoiding the development of monolithic codes and drawing upon the strong features of each.

We are therefore presently providing the features to allow the DINA 1.5D solver to evolve in the environment of the Cronos code, and for the Cronos sources and transport modules to be evaluated within the DINA-CH environment, a marriage assisted by both codes already running under Matlab [5]. Modifications are already underway to provide the requisite information from one solver to the other. It is expected that fully integrated simulations of ITER combining the strengths of DINA-CH and Cronos will become available in the near future. Figure 4 illustrates the combination of the two solvers, including the integration of the PSITBX diagnostics package together with the modelling of the sources and the equilibrium and kinetic controllers. We expect this to become a powerful simulation platform, ideal for testing on existing tokamaks and for predictive modelling for ITER.

Acknowledgements: This work was partly supported by the fonds national Suisse de la recherche scientifique. Thanks are due to Henri Weisen, Yann Camenen and Christian Ingesson during the implementation of the ITER diagnostics.

References

[1] J.B. Lister et al., paper P2.144, this conference

[2] J-M. Moret, private communication http://crppwww.epfl.ch/~moret

[3] Y. Martin et al., paper P4.133, this conference

[4] A.W. Degeling et al., Plasma Physics and Controlled Fusion, 45, 1637 (2003)

[5] Cronos, CEA Cadarache, private communication

Initial TORPEX results of plasma production, confinement and fluctuation studies

Mark A. McGrath, A. Fasoli, B. Labit, S. Müller, M. Podestà, F.M. Poli, K. Schombourg

Centre de Recherches en Physique des Plasmas (CRPP),
Association EURATOM-Confédération Suisse,
École Polytechnique Fédérale de Lausanne (EFPL), 1015 Lausanne, Switzerland.

Experimental configuration

TORPEX (TORoidal Plasma EXperiment) [1, 2] is a toroidal device for basic plasma physics research, with major radius $R = 1$m; minor radius $a = 0.2$m; toroidal and vertical magnetic field, $B_{tor} < 0.1$T, $B_v < 5$mT. Plasmas are generated by a microwave power source that can deliver up to 50kW at a frequency $\nu_{RF} = 2.45$GHz, modulated with frequencies up to 20kHz, during a typical discharge length of 100ms. Plasmas with densities of $n \sim 10^{17}\text{m}^{-3}$, electron temperature $T_e \sim 5 \rightarrow 10$eV and plasma potential $\sim 10 \rightarrow 30$V, measured by electrostatic probes, are typical.

First experimental campaigns have focused on basic plasma production and confinement mechanisms as well as on the physics of fluctuations driven in the region of density and temperature gradients. The ultimate goal of this work is to improve understanding and control capability of plasma turbulence and related transport.
The plasma confinement is optimised by superimposing a small vertical component over the dominant toroidal magnetic field [3]. The spiral-shaped field lines allow particles to partially short-circuit the vertical electric field E_z driven by charge dependent ∇B and curvature drifts. Coulomb collisions limit this short-circuiting effect, allowing the formation of an equilibrium characterised by a finite value of E_z. The competition between two loss mechanisms, the radial $\mathbf{E} \times \mathbf{B}$ drift ($\propto B_z^{-2}$) and the direct particle loss at the intersection of the field lines with the vacuum vessel ($\propto |B_z|$), leads to an optimal value of B_z, for which the confinement time is maximum.

Plasma production

Plasmas are created by microwaves in the electron cyclotron (EC) range of frequencies injected in O-mode polarisation from the low field side (LFS). The ionisation process is initiated at the EC layer by electrons accelerated resonantly by the wave field. Once the plasma is formed, due to the low value of T_e, the injected waves are subject to weak single pass absorption at R_{EC}. The transmitted waves are reflected by the vessel walls and contain a mix of O- and X- polarisations. At the upper hybrid layer R_{UH}, the X-mode encounters a resonance, where the electric field can accelerate electrons to energies above the ionisation potential.

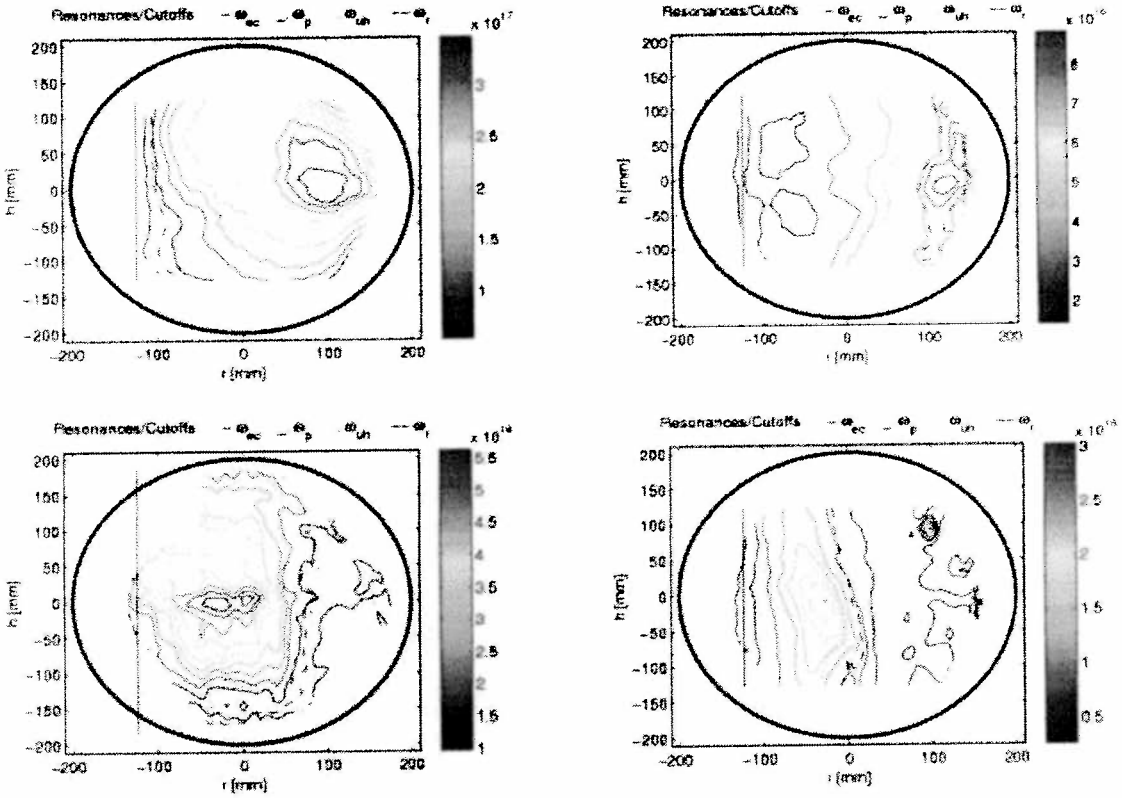

Figure 1: *Argon (left) & Hydrogen plasma density profiles, 10kW (top) & 500W*

As a consequence, the density is expected to increase at the UH layer. As ω_{UH} depends on n, the profile should extend from R_{EC} to R_{UH}, shifting to the LFS as the microwave power is increased. Such an effect is clearly observed both in Hydrogen and Argon plasmas, as shown in Figure 1. As the steady-state profile is the result of a balance between the plasma production and the mechanisms leading to an equilibrium, the maximum of the density does not necessarily peak at the UH layer, and may include over dense regions.

The over-dense region is observed to be wider in Argon plasmas, with a higher density and a more peaked profile, than in Hydrogen.

In order to assess the effect of absorption at ω_{UH}, experiments with modulated EC power were performed (square wave modulation at 600Hz, with a duty cycle of 33% and $P_{RF} = 1 \rightarrow 1.5$kW).

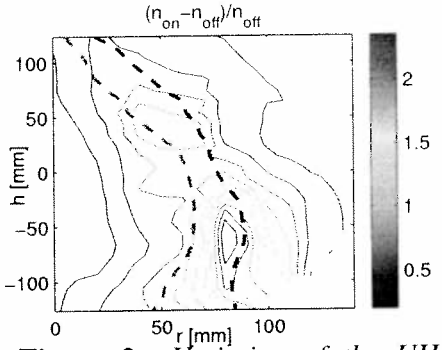

Figure 2: *Variation of the UH position during plasma modulation experiments (Green/red:low/high power)*

This allows the separation of the fast ionisation and absorption processes from the slower mechanisms that lead to the plasma equilibrium. Figure 2 shows that the increase in $n(r,h,t)$ caused by the increase in the EC power is localised at the UH layer, confirming the role of the UH resonance in the ionisation process.

In some experimental regimes, with relatively large toroidal field and microwave power, large oscillations with frequencies $6-12$kHz are observed in both the absorbed power (estimated from measurements of injected/reflected microwave power) and density (Figure 3). The two quantities appear strongly correlated, with relative phases and amplitudes of the density oscillations depending on the spatial location. The coupling between density and absorbed power may be mediated by the UH resonance, via the absorption and ionisation mechanisms discussed above: as the density is increased, the UH layer moves outward, absorbing the injected power at the plasma edge and preventing it from reaching the plasma core, where the density would then tend to decrease. The time scale for such decrease should be related to the characteristic time for the relaxation of the density at different locations. The measured oscillation periods are in fact observed to be of the same order of the estimated particle confinement time.

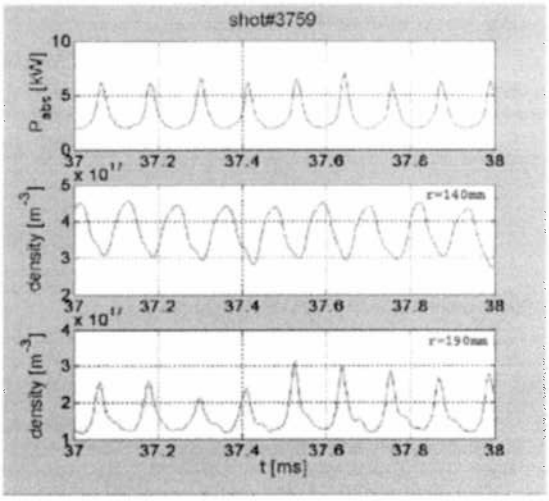

Figure 3: *Coupling between density and absorbed power*

Coherent modes & turbulent structures

Depending on the experimental conditions, low frequency (much lower than the ion cyclotron frequency) coherent modes and turbulent regimes have been observed in the spectra of density fluctuations (Figure 4). In Argon plasmas, modes with frequency $f = 8.34kHz$ and wave-number $k_\theta = 0.6cm^{-1}$ have been measured, propagating in the electron diamagnetic direction with a phase velocity $v_\theta = 860m/s$. This value is comparable with the drift velocity estimated from the background parameters, $1.1 \pm 0.4km/s$.

Due to the dependence of the phase velocity on the gradient length scale [4], and the measured value of the component of the wave-number along the toroidal direction ($k_{||} \ll k_\theta$), the modes can be identified as drift waves.

The Conditional Average Sampling technique [5], applied to data from Langmuir probes, has revealed the existence of structures in the density, propagat-

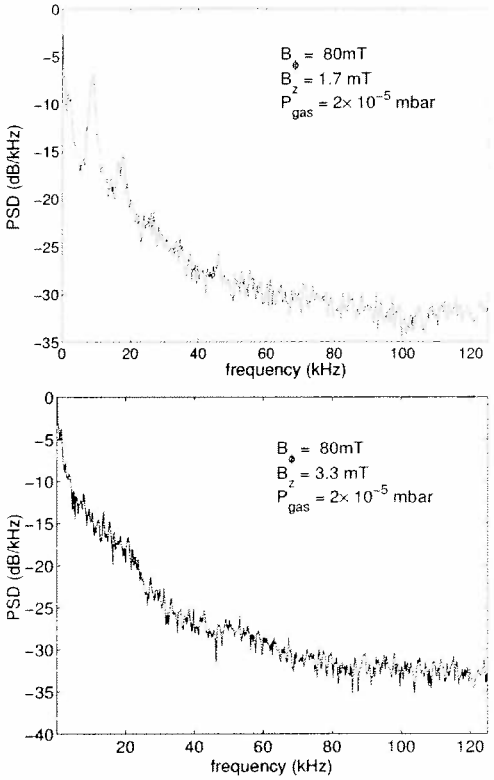

Figure 4: *Frequency spectra of density fluctuations in Argon plasma: coherent (top) and turbulent case (bottom)*

ing in the poloidal plane along the $\mathbf{E} \times \mathbf{B}$ direction with velocity $v \approx 500m/s$ (Figure 5).

Diagnostic plans

In order to characterise the plasma fluctuations and turbulent structures and to determine the physical mechanisms that lead to their formation, high spatial and temporal resolution diagnostics are needed. Several are envisaged for the next campaign.

For the measurement of density and potential fluctuations, a 92 tip Langmuir probe array covering the entire poloidal section has been designed and is under construction. The spatial resolution is about $\sim$ 3.5cm and has a high temporal resolution of 400kHz. A 3-tip Langmuir probe for detecting density and potential fluctuations with high temporal ($10MHz$) resolution will also be installed to measure the fluctuation-induced particle flux over a plane perpendicular to the toroidal magnetic field.

A study of the feasibility of optical imaging techniques has just been completed. Initial results from a fast photomultiplier detector coupled to an optical fibre, suggest that the photon levels are sufficient for different optical techniques. This will allow the use of a fast camera imaging system, 40 – 100k frames/sec, for observing the fluctuations in the visible light emission from neutrals due to T_e fluctuations. Possible extensions to velocity-dependent imaging techniques based on laser induced fluorescence are also envisaged.

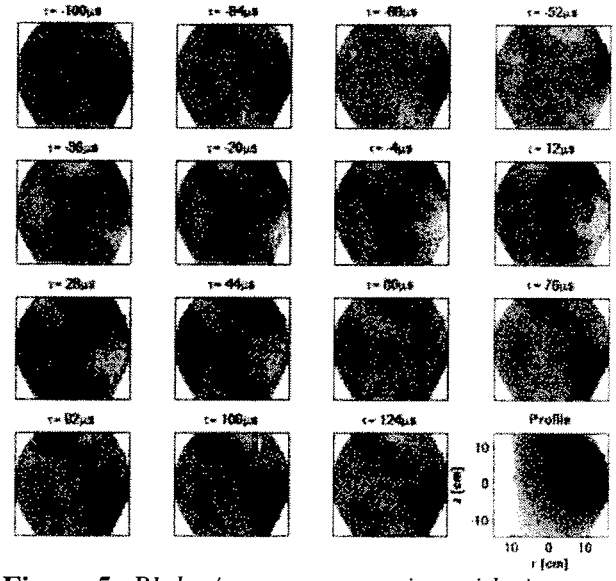

Figure 5: *Blobs / structures moving with time and their projection in the poloidal plane*

Acknowledgements

This work is partly funded by the "Fonds National Suisse pour la Recherche Scientifique." MMcG is supported by a EURATOM Marie Curie Fellowship.

References

[1] M. Podestà, A. Fasoli, *et al.*, in *Proceedings of the 30th EPS Conference on Controlled Fusion and Plasma Physics* (St. Petersburg, Russia, 2003).

[2] A. Fasoli, B. Labit, *et al.*, in *45th DPP meeting of the American Physical Society* (APS, Albuquerque, New Mexico, USA, 2003).

[3] S. Müller, A. Fasoli, *et al.*, Physical Review Letters (submitted to).

[4] F. Poli, A. Fasoli, *et al.*, in *45th DPP meeting of the American Physical Society* (APS, Albuquerque, New Mexico, USA, 2003).

[5] H. L. Pécseli and J. Trulsen, Physics of Fluids B **1**(8), 1616 (1989).

Comparison of the properties of quasi-isodynamic configurations for different numbers of periods

M.I. Mikhailov[1], W.A. Cooper[2], M.F. Heyn[3], M.Yu. Isaev[1], V.N. Kalyuzhnyj[4], S.V. Kasilov[4], W. Kernbichler[3], V.V. Nemov[4], C. Nührenberg[5], J. Nührenberg[5], M.A. Samitov[1], V.D. Shafranov[1], A.A. Skovoroda[1], A.A. Subbotin[1], K. Yamazaki[6], R. Zille[5]

[1] *Russian Research Centre "Kurchatov Institute", Moscow, Russia*

[2] *CRPP, Association Euratom-Confédération Suisse, EPFL, Lausanne, Switzerland*

[3] *Institut für Theoretische Physik, Technische Universität Graz, Graz, Austria*

[4] *IPP, NSC "Kharkov Institute of Physics and Technology", Kharkov, Ukraine*

[5] *Max-Planck-Institut für Plasmaphysik, IPP-EURATOM Association, Germany*

[6] *National Institute for Fusion Science, Oroshi-cho 322-6, Toki 509-5292, Japan*

Abstract

Properties of quasi-isodynamicity (qi)-optimized [1] configurations with poloidal direction of the contours of B on magnetic surfaces for different numbers of periods are discussed. It is shown that with increasing number of periods the stability- β limit increases and such good properties as long-time collisionless fast particles confinement, small neoclassical transport and small bootstrap current, can be maintained.

Introduction

In Ref. [1] it was shown that in stellarators with poloidal direction of the contours of B on magnetic surfaces good long-time collisionless confinement of fast particles can be achieved by approaching fulfilling of the qi condition for deeply to moderately trapped particles. This condition requires the contours of the second adiabatic invariant, $\mathcal{J} = \oint V_{||} dl$, to be constant on magnetic surfaces. In Ref. [2], by computational optimization of a six-period configuration with $< \beta >= 5\%$, the possibility was shown to satisfy the qi condition for all reflected particles. The configuration found was stable against Mercier and resistive-interchange modes and has a small effective ripple and bootstrap current [3,4]. Because of these attractive features of qi configurations it was interesting to study the possibility to increase the β value for the $N = 6$ system and to consider configurations of such type for larger and smaller numbers of periods. To clarify (at least partially) the dependencies of the properties of these systems on the number of periods, here the result of the optimization for $N = 3$, $N = 6$ and $N = 9$ configurations are presented. While the optimization is not fully completed yet, some characteristic features and dependencies of the configuration properties upon the number of periods are clearly seen.

Initial configuration and main goals of optimization

The optimizations were carried out on the NEC SX-5 supercomputers himiko (Germany) and prometeo (Switzerland) with the VMEC code [5] for equilibrium calculations, the JMC code [6] for the transition to magnetic (Boozer) coordinates and the MCT code [7] for direct calculation of particle drift orbits. As the starting point, the boundary magnetic surface of the $N = 6$ configuration optimized earlier [2] was used. The shapes of the cross-sections at the beginning and half of the period are similar to that of the stellarator W7-X [8]: the cross-section in the region of minimal B has triangular shape and that in the region of maximal B is been-shaped. The initial boundary magnetic surfaces for $N = 3$ and $N = 9$ configurations were constructed by changing the aspect ratio of the $N = 6$ configuration. For all three configurations the attempt was made

to find the stability- β limit while maintaining good collisionless confinement as well as small effective ripple and bootstrap current.

Initial runs showed that from the point of view of stability different values of β should be chosen for different numbers of periods. The optimization then was performed for the following β values: $<\beta>= 3.9\%$ for $N = 3$, $<\beta>= 8.9\%$ for $N = 6$ and $<\beta>= 10\%$ and $<\beta>= 15\%$ for $N = 9$. The stability- β limits found are close to, but do not coincide exactly with these choices. Because of such a strong dependence of the β limit on the number of periods, other properties of these configurations depend on the correlated triple aspect ratio, number of periods and β .

Some characteristic features of qi configurations and their dependencies on the number of periods

Characteristic geometry of the magnetic surfaces and value of mirror component

The 3D view of the qi-optimized configurations for small (N=3) moderate (N=6) and large (N=9) numbers of periods are shown in Fig. 1. The color here corresponds to the magnetic field strength on the boundary magnetic surface. It is seen that a significant mirror component of B is present in all configurations. The value of this component diminishes with increasing number of periods. Also, it is seen that for all cases the plasma columns are almost straight in the vicinity of B extrema. It is just the smallness of the magnetic axis curvature in the cross-sections with B extrema that permits to avoid the appearance of islands in the contours of B on magnetic surfaces and to close the contours of B poloidally. The deviation of the plasma column from the plane increases with diminishing the number of periods. In the table (see below) the aspect ratios and the ratios of B_{max}/B_{min} on boundary magnetic surfaces are shown for all three configurations.

Fig.1. Boundary magnetic surfaces of the optimized $N = 3$, $N = 6$ and $N = 9$ configurations. The color corresponds to the magnetic field strength on the boundary magnetic surfaces.

Effect of β value on particle confinement

During the optimization it was found that for configurations with larger number of periods (and higher β value) the collisionless confinement of fast particles is improved, at least for particles started at half of the plasma minor radius. This can be explained as follows. Because of the poloidal direction of the contours of B on magnetic surfaces in these configurations the reflected particles are restricted to the periods and the trajectories of their banana centers can be described by the contours of the second adiabatic

invariant. The value of $\mathcal{J}$ is a function of flux label and poloidal angle. In the ideal case of exact quasi-isodynamicity the poloidal variation of $\mathcal{J}$ should be zero. Computationally, it can be made small, but not exactly zero. Thus, the behavior of the contours of $\mathcal{J}$ does not only depend on its poloidal variation, but on its radial dependence, too. With increasing β , the radial dependence of $< \mathcal{J} >_\theta$ becomes larger because of the diamagnetic effect, so that even for significant poloidal variation of $\mathcal{J}$ it became possible to close its contours inside the plasma column. In spite of the small diamagnetic effect for the three-period configuration with $< \beta >= 3.9\%$, approaching qi here permits to improve the fast particle confinement significantly, too.

The results of direct calculations of collisionless α -particles losses are shown in the table. The calculations were made for power-plant type parameters ($B_0 = 5T, V = 1000m^3$). One thousand particles start at 1/2 of the minor plasma radius. The losses are shown for a time of flight $\tau = 1sec$.

Effective ripple in qi configurations

As a measure of the neoclassical transport in $1/\nu$ regime the value of effective ripples is used (see, e.g. Ref. [9]). The transport coefficients are proportional to $\epsilon_{effective}^{3/2}$ and inversely proportional to the square of large radius of the plasma column. The value of effective ripples is directly connected with the poloidal variation of the second adiabatic invariant. Diminishing the poloidal variation of $\mathcal{J}$ leads to diminishing the effective ripple. The radial dependence of $\mathcal{J}$ is not important for the effective ripple. One can note that – while in the ideal case of exact qi, when the second adiabatic invariant is constant on magnetic surfaces, there should be no particle losses and the effective ripple should equal zero, in the cases realized here a decorrelation is seen between collisionless losses and effective ripple: with increasing β the closure of $\mathcal{J}$ contours does not lead automatically to small effective ripple. Thus, for a large number of periods and large β values an additional optimization to diminish the effective ripple was performed. As a result, for all configurations the values of effective ripple were made small enough. The characteristic values of $\epsilon_{effective}^{3/2}$ for 1/2 of the plasma minor radius are shown in the table.

Bootstrap current in qi configurations

Because of the poloidal direction of the contours of B on magnetic surfaces, the radial shifts of trapped particle orbit portions with the same direction of parallel velocity change sign as the particle drifts poloidally. This leads to the possibility of small bootstrap current in the configurations considered here. Indeed, by optimization it has been shown that the structural factor of bootstrap current can be made much smaller here than in configurations with axial or helical direction of the contours of B on magnetic surfaces. The values of the factor of the bootstrap current for 1/2 of the plasma minor radius are shown in the table. The characteristic values of this factor for systems with axial or helical direction of the contours of B are of the order of 5-10.

Stability properties of qi configurations

For all cases there were no problems to stabilize Mercier and resistive-interchange modes by optimization. The stabilization of these modes does not lead automatically to ballooning modes stability. Additional optimization toward ballooning-mode stability was carried out for several values of the parameters θ_0, ζ_0 of the ballooning-mode equation. In addition, for the configurations with $N = 6$ and $N = 9$ the investigation of the global-mode stability by the CAS-3D code [10] was performed. The results are

shown in the table. For the three-period configuration the table shows the stability limit for ballooning modes. The corresponding calculations of global-mode stability will be made in the future. It is worth mentioning here that for the $N = 9$ configuration optimized toward collisionless particle confinement and ballooning-mode stability only, the effective ripple then turning out significantly larger, the global-mode stability limit was found to be significantly higher, $< \beta >= 14.5\%$. Further attempts are required to elucidate the possibility to increase the β limit for $N = 9$ configuration.

Table. Comparison of the configuration properties for different number of periods

N \ Property	A	B_{max}/B_{min}	Losses	β limit	$\epsilon^{3/2}$	G_{BC}	ι range
N=3	6.8	2.9	100	3.9%	0.002	0.7	0.67 - 0.71
N=6	12	1.8	0	8.4%	0.0012	0.05	0.86 - 1.0
N=9	24	1.5	0	10.5%	0.002	0.1	1.56 - 1.73

Conclusions It is shown by qi optimization of configurations with small, moderate and large number of periods that configurations of qi type can be realized in this range of numbers of periods. Approaching qi permits to find configurations with good confinement of fast particles, small neoclassical transport and small bootstrap current. It is shown that for these configurations increasing the number of periods leads to increasing the MHD stability limit with simultaneous maintaining small bootstrap current, in contrast to systems with quasi-helical or quasi-axial symmetry.

Acknowledgement This work was supported by the Russian-Germany agreement WTZ-RUS-01/581, by the Russian Federation President program on support of leading scientific schools, Grant No 2024.2003.2, by the Russian Fund for Basic Research, Grant No 03-02-16768, by the Fonds National Suisse de la Recherche Scientifique, Euratom, by the Association EURATOM-OEAW and by the Austrian Academy of Sciences.

References

[1] Gori S., Lotz W. and Nührenberg J. 1996 *Theory of Fusion Plasmas (International School of Plasma Physics)* (Bologna: SIF) p. 335

[2] Mikhailov M.I., Shafranov V.D., Subbotin A.A et al *Nuclear Fusion* **42** 2002 p. L23.

[3] A.A. Subbotin, W.A. Cooper, M.I. Mikhailov et al, "Elimination of the Bootstrap Current Factor in Stellarators with Poloidally Closed Contours of the Magnetic Field Strength", report on 30th EPS Conference, St.-Petersburg, Russia, 2003.

[4] W. Anthony Cooper, S.Ferrando i Margalet, S.J. Allfrey, et al *Plasma Phys. Control. Fusion* **44** (2002) B357-B373.

[5] Hirshman S.P. and Betancourt O., J. of Comput. Physics **96** (1991) 99.

[6] Nührenberg J., Zille R., Theory of Fusion Plasmas (Varenna 1987), Editrice Compositori, Bologna (1988) 3.

[7] Fowler R.H., Rome J.A., Lyon J.F., Phys. Fluids **28** (1985) 338.

[8] Lotz W., Nührenberg J., Schwab C., in Plasma Phys. and Contr. Nuclear Fusion Res. 1990 (Proc. 13th Int. Conf., Washington 1990), **2**, IAEA, Vienna (1991)603.

[9] V. Nemov, S. Kasilov, W. Kernbichler, M. Heyn, *Phys. Plasma*, **6**, (1999) 4622.

[10] C. Schwab, *Phys. Fluids B*, **5** (1993) 3195

Magnetic Diagnostics of Non-Rotating Magnetic Island in LHD

Y. Narushima[1], N. Ohyabu[1], S. Sakakibara[1], K.Y. Watanabe[1], T. Yamaguchi[2], H. Yamada[1], K.Narihara[1], I.Yamada[1], T.Morisaki[1], S.Inagaki[1], Y.Nagayama[1], A.Komori[1] and LHD exp. group[1]
W.A.Cooper[3]

[1] *National Institute for Fusion Science, Toki, Gifu 509-5292, Japan*

[2] *Dep. of Fusion Science, Graduate Univ. for Advanced Studies, Toki, Gifu 509-5292, Japan*

[3] *CRPP Association Euratom / Confederartion Suisse, EPFL, 1015 Lausanne, Switzerland*

1.Introduction

Magnetic islands sometimes play key roles in toroidal plasma confinement from the viewpoint of Magneto-Hydro Dynamics (MHD) stability. In Tokamaks, for example, a seed island triggers a neoclassical tearing mode, and its growth leads to serious deterioration of the confinement. On the other hand, it is possible that the island flattens the pressure profile at the resonance surface, contributing to the stabilization of the pressure-driven resonant MHD mode. In the Large Helical Device (LHD), the perturbed field $\tilde{b}_0$ produced by the external perturbed coils [1] can produce a magnetic island in the vacuum field. The seed island grows or reduces without rotation during the plasma discharge. The width, w, of the island is indicated by the flattening of the electron temperature profile measured by Thomson scattering. In LHD the profile only can be obtained at one toroidal position and therefore gives limited knowledge of the structure of the island.

The width w is related to the perturbed field [2]

$$w^2=C(\tilde{b}_0+\tilde{b}_1)/B_t \qquad (1)$$

here C, $\tilde{b}_1$ and B_t are a constant, perturbed field during the plasma discharge and the toroidal field, respectively. For $\tilde{b}_1=0$ and $\tilde{b}_0 \neq 0$, the width w is equal to that of the vacuum island ($w=w_{vac}$). The magnetic diagnostics measuring the profile of $\tilde{b}_1$ is an effective method to find the structure of the magnetic island.

2.Experimental setup

The toroidal array of magnetic flux loops is set at the outer ports in LHD as shown in Fig.1. Each flux loop has N=10 turns wound at the ports whose cross-sections are around $S\approx 1.2\text{m}^2$ and have a total cross-section of about $NS=12\text{m}^2$,which leads to enough electromotive force voltage to detect the slow (few 100ms) and weak (few Gauss) change of the magnetic field.

The shapes of the flux loops at the toroidal angles $\phi=-162, -54, 54, 90$, and 162 are planar (coloured line in Fig.1) that we use here and the other ones are 3-dimensinal (dotted line in Fig.1). During a plasma discharge these loops can detect the perturbed magnetic flux Φ^R which originates from the growth and reduction of the width of the island. The detected magnetic fluxes Φ^Rs are normalized by the total cross section NS to $\tilde{b}_1$ whose component is in the major radial direction. The 4-pairs of perturbation coils placed at the top and bottom of LHD around $\phi=\pm 90$[deg] (solid line in Fig.1) produce the static perturbation field $\tilde{b}_0$ having an $m/n=1/1$ mode which produces a seed island whose O(X)-point stays at the outer board side at $\phi=90(-90)$[deg] in this study. A Thomson scattering system measures the T_e profile at $\phi=-18$[deg]. The w is estimated as the inner flattening width of the T_e profile as shown in Fig3(a)(c).

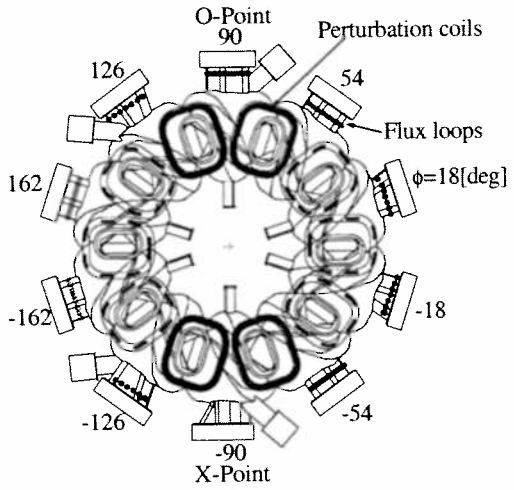

Fig.1 Top view of the vacuum vessel of LHD
Toroidal angle ϕ is defined $-180<\phi<180$[deg]

3. Experimental results and discussion

The typical discharge with a seed island ($w_{vac}\approx 150$[mm]) produced by the perturbed field $\tilde{b}_0$ is shown in Fig.2, in which the island width w grows from 150 to 200[mm] as shown in Fig.2(d). The magnetic field $\tilde{b}_1$ varies with time (Fig.2 (e)). Each colour corresponds to that of the flux loops in Fig.1. The $\tilde{b}_1$ at $\phi=-162$ and 162[deg] reduces to $\tilde{b}_1\approx -0.8$[Gauss]. On the other hand, the $\tilde{b}_1$ at $\phi=54$[deg] increases to $\tilde{b}_1\approx 0.8$[Gauss].

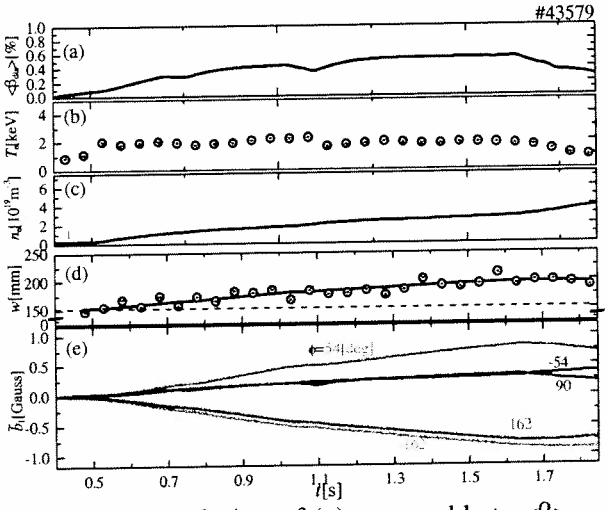

Fig.2 Time evolution of (a)averaged beta $<\beta>_{dia}$ (b)electron temperature at centre T_e (c)averaged electron density n_e (d)island width w (e)perturbed field $\tilde{b}_1$

The T_e and $\tilde{b}_1$ profiles at $t=0.48$ and 1.73[s] are shown in Fig.3. At $t=0.48$[s], Fig3(a) shows that the island width does

not change and is almost same as the seed island width. The flux loops detect zero field $\tilde{b}_1$ as shown in Fig3(b). At t=1.73[s], the island width becomes w=200[mm] (Fig3(c)) and the finite field $\tilde{b}_1$ appears as shown in Fig3(d). The fitting curve $\tilde{b}_1(\phi)=\tilde{b}_1{}^{n=1}\cos(\phi-\phi_{n=1})$ well expresses the $\tilde{b}_1$ profile, which has the dominant toroidal mode n=1. Here, $\tilde{b}_1{}^{n=1}$ and $\phi_{n=1}$ are the maximum amplitude and its toroidal angle respectively. Figure4 shows the time trace of the $\tilde{b}_1{}^{n=1}$ and $\phi_{n=1}$. The amplitude increases from $\tilde{b}_1{}^{n=1}$=0 to 0.9[Gauss] (Fig.4(a)) and the angle does not change from around $\phi_{n=1}$=0 during the plasma discharge(Fig.4(b)). These results mean that the magnetic island width increases with time and does not rotate, and the position of O(X)-point stays at inner (outer) board side at $\phi=-90$[deg].

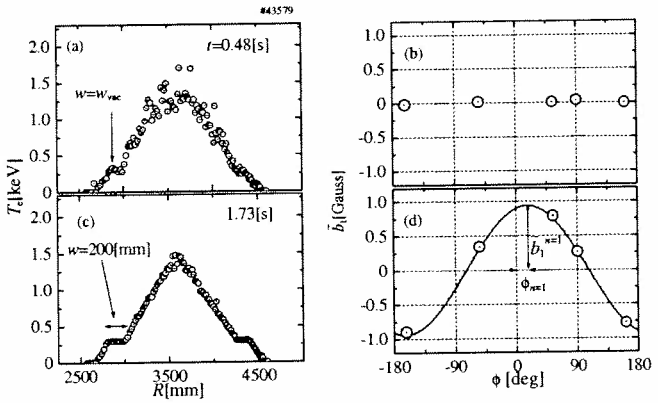

Fig.3 T_e and $\tilde{b}_1$ profile at (a)(b) t=0.48[s], (c)(d) 1.73[s]

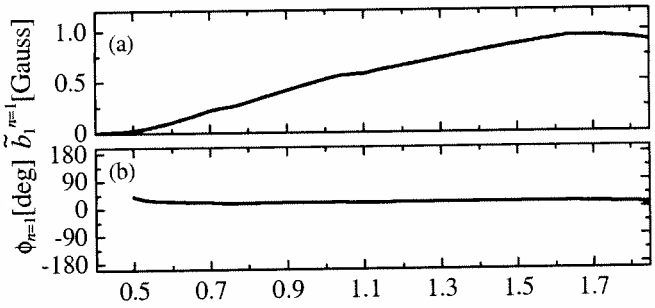

Fig.4 Time trace of (a) $\tilde{b}_1{}^{n=1}$ and (b) $\phi_{n=1}$

The profile of $\tilde{b}_1$ with the toroidal mode n=1 indicates that the change of the magnetic island width during a discharge also has the n=1 mode component. These results depend on the assumption that the profile of $\tilde{b}_1$ is due to the structure of the island with the m/n=1/1 component. The amplitude $\tilde{b}_1{}^{n=1}$ estimates the width w by using Eq (1) that can be rewritten as follows

$$w=(\alpha(\tilde{b}_1{}^{n=1}/B_t)+w_{vac}{}^2)^{0.5} \qquad (2)$$

The calibration between w and $\tilde{b}_1{}^{n=1}/B_t$ provides the coefficient α for the island enlargement cases ($w \geqq w_{vac}$). As a result, the magnetic diagnostics can estimate the island

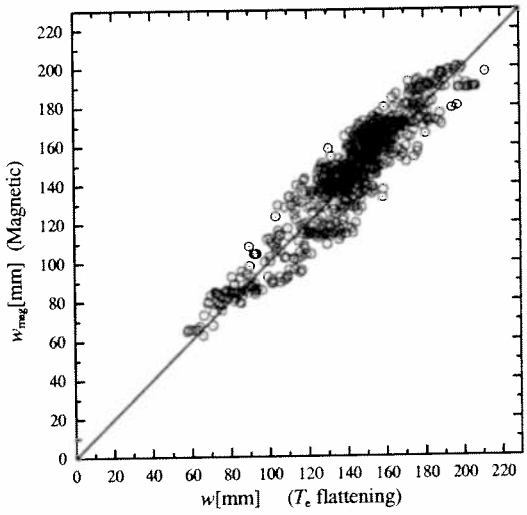

Fig.5 Relationship between w_{mag} and w

width w_{mag}. Figure5 shows the relationship between w and w_{mag}. The solid line in Fig2(d) is the time trace of w_{mag} derived from $\tilde{b}_1$, which can fit the w. These results show that this magnetic loop with large NS can be used to estimate the structure of the non-rotating magnetic island.

For the island reduction or disappearance ($0<w<w_{vac}$, in other words, healing [3,4]), finite $\tilde{b}_1$ can be detected even though a seed island exists. Figure 6 shows the T_e and $\tilde{b}_1$ profiles for the island disappearance case with w_{vac}=114[mm]. The flattening does not appear (Fig6(a)) and finite $\tilde{b}_1^{n=1}$ is indicated and $\phi_{n=1}$ shifts by 180[deg] from the increasing case shown in Fig3(d).

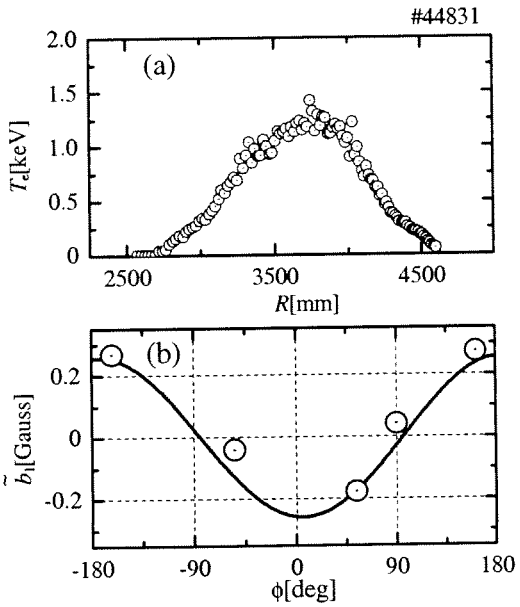

Fig.6 T_e and $\tilde{b}_1$ profile for the island reduction plasma

This result means that some kinds of current layer inside plasma produce $\tilde{b}_1$ that suppresses the seed island in the LHD. We are studying what kind of structure the current layer has.

4. Summary

We carry out the magnetic diagnostics of non-rotational magnetic island in LHD. The finite magnetic field appears with a change of the magnetic island width. Magnetic diagnostics can estimate the structure of an island. Even in the disappearance of a magnetic island, a finite magnetic field appears. Further study is intended to reveal the formation mechanism of the current layer producing $\tilde{b}_1$ which affects the behaviour of the magnetic island.

Acknowledgement

This study was supported by a Grant-in-Aid for Young Scientists (B)(No.15760627) from the Ministry of Education, Culture, Sports, Science and Technology of Japan.

References

[1] T. Morisaki et al., Fusion Engineering and Design. **65**, 475 (2003)

[2] A. H. Boozer, Phys. Fluids **27**, 2055 (1984)

[3] K. Narihara et al., Physical Review Letter **87**, 135002 (2001)

[4] N. Ohyabu et al., Physical Review Letter **88**, 055005 (2002)

3rd Harmonic ECH on TCV using Vertically Launched 118GHz Radiation

L. Porte, S. Alberti, G. Arnoux, T.P. Goodman, M.A. Henderson, J-P. Hogge

Centre de Recherches en Physique des Plasmas, Association EURATOM – Confédération Suisse, EPFL, CH-1015 Lausanne, Switzerland

ABSTRACT

The TCV electron cyclotron resonance heating (ECRH) system has been upgraded with the addition of three 118GHz, 500kW gyrotrons. They are designed to heat at the 2nd harmonic (n=3) of the cyclotron resonance using extraordinary mode (X-mode) radiation. Vertical launch geometry is used to maximize the path length along the resonance. The plasma facing mirror is on the top of the machine. Real-time control of the poloidal launch angle has been installed and is being commissioned. The X3 system enables the heating of high density ($\leq 1.1\times10^{20}$ m^{-3}) plasma. Attempts have been made to heat the core plasma of H-mode discharges on TCV. This paper will briefly describe the X3 heating system and the real-time mirror control system. Initial results from the heating of H-mode will be presented

THE X3 HEATING SYSTEM

The entire X3 system is described by J.P. Hogge et al [1]. Three gyrotrons operate at 118 GHz and each radiate ≈480 kW. A matching optics unit (MOU) is used to set the polarisation and ellipticity of the gyrotron beam. The output, from each gyrotron, is transmitted to the tokamak or a calibrated load along ≈40m of evacuated corrugated waveguide. Each gyrotron has its own transmission line. The three separate waveguides converge on a single launch mirror that has a focal length of 700mm and is made of copper. The beam waist radius in the plasma is ≈3cm. The mirror can be translated, between shots along a major radius between 800mm and 965mm and can be rotated poloidally, during a shot, in the range 40° to 50°.

REAL-TIME CONTROL OF THE LAUNCHER MIRROR

The optimum electron density for X3 absorption is $\approx 7.1\times10^{19}$ m^{-3}. The absorption is a very sensitive function of the electron density. During X3 heating, plasma profiles of density and temperature change altering respectively the absorption plus refraction and the position of the absorption maximum. The launch mirror must be controlled, in real time, to accommodate this. A real time control system has been designed and implemented for this

purpose. Feed-back control of the poloidal launch angle is achieved using an error signal obtained by measuring the plasma response (centrally viewing SXR camera) to a small sinusoidal oscillation imposed on the launch mirror. A controller based on this perturbation method has been implemented. Figure 3a shows a schematic of the controller and while Figure 3b shows the error, phase and plasma response signals to the mirror perturbation imposed on a linear ramp of the mirror poloidal angle. This experiment was done in an 'open loop configuration. Closed loop have been started.

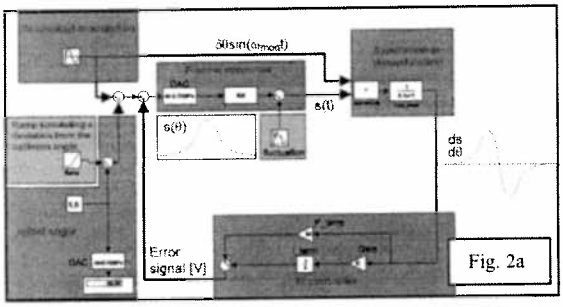

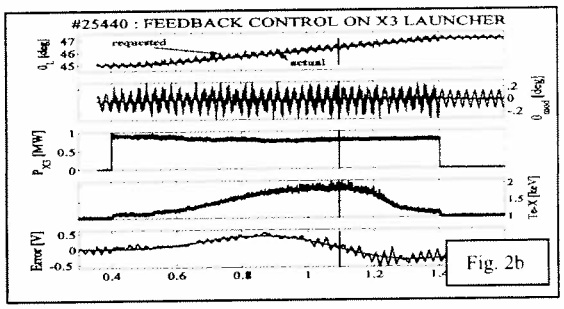

Figure 2a schematic diagram of the principle of operation of the real time mirror control system. A sinusoidal perturbation is applied to the mirror angle that causes a perturbation to the plasma response (central viewing SXR signal; TeX). This plasma perturbation is used to extract a phase signal that is zero when the mirror angle is at its optimal position. Figure 2b shows the plasma to a linear sweep of the mirror angle with the perturbation imposed upon it. The phase of the plasma response is zero at the optimal angle (peak of TeX).

FAST ELECTRON PHYSICS AND X3

X3 absorption can be higher than predicted by thermal plasma theory (at TCV the linear ray-tracing code TORAY-GA). Diamagnetic loop (DML) measurements [2] show that 100% X3 absorption can be achieved in cases where TORAY-GA predicts substantially less. Fast electrons play a significant role in X3 absorption. By sweeping the poloidal angle of the X3 launch mirror from the high field side (50°) to the low field side (40°) one, in effect, uses the relativistic line broadening to probe separately the response of fast electrons and thermal electrons. In this way it might be possible to use X3 absorption measurements as a tool for diagnosing fast electrons. Initial, proof of principle, experiments have been performed to test this idea. Using DML measurements (the *thermal + non-thermal* plasma response), electron temperature measurements from SXR signals (thermal plasma response) and ECE measurements (the fast electron response) it has been possible to separate the fast electron and thermal plasma responses. Experiments continue to examine the role of fast electrons in X3 absorption and to test the feasibility of using X3 absorption measurements to diagnose fast electrons.

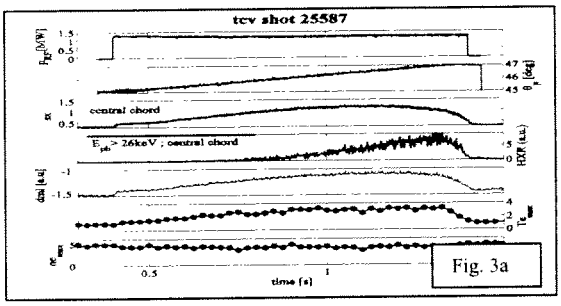

Fig. 3a

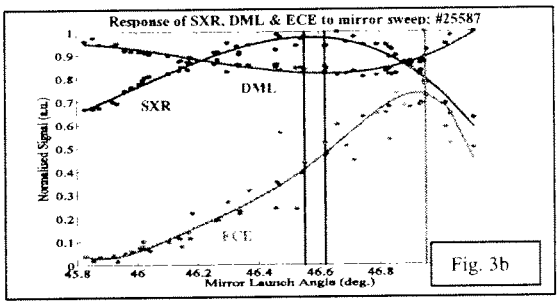

Fig. 3b

Figure 3a: overview of shot #25587 showing the X3 power gate (top), the poloidal angle of the launcher mirror, a central SXR signal, photon count (non-thermal response), the diamagnetic loop signal and the electron temperature and density. Figure 3b: the response of a central viewing SXR camera (thermal response), the diamagnetic loop (total plasma energy) and an ECE channel (non-thermal response). It is clear that as the mirror is swept from the high angle (fast-electrons) to low angle (thermal electrons) the thermal and non-thermal components can be excited separately. The total plasma response (DML) exhibits a peak shifted away from the thermal plasma peak showing, again, that fast electrons play an important role in X3 absorption.

H-MODE AND X3 HEATING

Efforts to heat H-mode have focussed on using X3 to heat quasi-stationary ELMy H-modes and to provoke the L- to H-mode transition using X3 heating. It is to be noted that the ELM type on TCV is still a subject for debate [3].

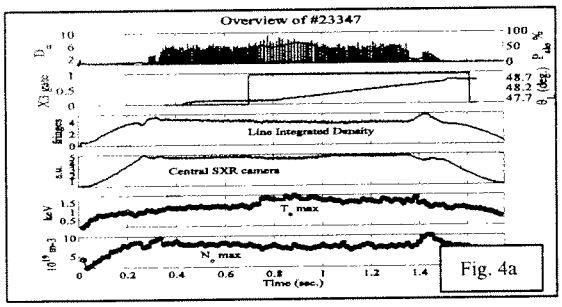

Fig. 4a

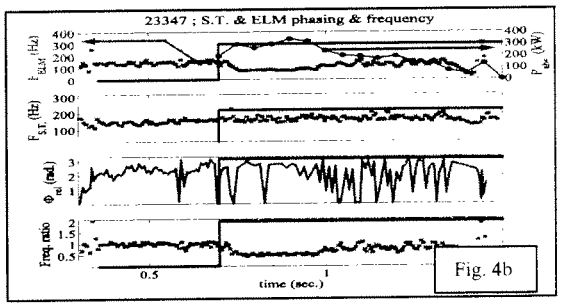

Fig. 4b

Figure 4a: Overview of shot #23347 showing the D_α with the coupled X3 power, the mirror launch angle and the power gate, the line integrated density, the maximum electron temperature and the maximum electron density. Figure 3b shows the ELM/SAWTOOTH frequency and phasing for #23347. Once the coupled power exceeds ≈200kW the ELM frequency drops to precisely one half the sawtooth frequency with a phase closed to but less than π; the ELMs *precede* the closest, in time, sawtooth. While the X3 coupled power <200kW and in the ohmic case the ELM frequency was very close to the sawtooth frequency. The ELMs precede the closest sawtooth in time.

ELMs and sawteeth on TCV are strongly coupled [4]. Experiments have been performed to examine the effect of core additional heating on this coupling. By heating an ELMy H-mode with X3 coupled power <400kW it was possible to maintain the ELMy H-mode. At coupled power <200kW the ELM/sawtooth relationship remained the same as in the ohmic case. However, at X3 coupled power >200kW the relationship changed. On a time scale similar to the energy confinement time, the ELM frequency dropped to one half the sawtooth frequency and the phase came close to locking (see Figure 3b). The ELMs still preceded the sawteeth. This observation is unexplained.

It has been possible to induce the L- to H-mode transition in ohmic L-mode discharges close to the transition threshold. These discharges have all transited directly into an ELM free H-

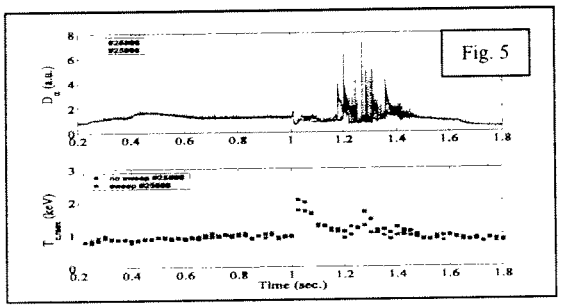

mode with a consequent uncontrolled rise in electron density and coupled power loss due to refraction. Attempts have been made to combat the refraction by sweeping the launcher mirror angle. This has had some success in increasing the electron temperature and prolonging the H-mode phase. Figure 5 compares two discharges one without a mirror sweep (#25866; red) and the other with (#25868; blue). #25868 achieves higher electron temperature in the first H-mode phase (2keV compared to 1.8keV) and transits into a second ELM-free H-mode phase after the back transition. The mirror sweep reduced the effects of the density rise in the ELM free H-mode.

CONCLUSIONS

Experiments have begun to exploit the capabilities of the X3 additional heating system on TCV. It has proven necessary to incorporate a real time control system on the poloidal launch angle of the launch mirror. The real time controller is being commissioned. Experiments have been performed to examine the effect of moderate power X3 heating on the ELM/sawtooth phasing in TCV H-modes and it has proven possible to phase lock the ELMs and sawteeth at coupled X3 power >200kW. It has been possible to provoke the L- to H-mode transition using X3 but to control the H-mode thereafter and to maintain X3 power coupling has proven difficult due to the uncontrolled density rise in ELM free H-mode. Work continues to address this problem.

REFERENCES

[1] J-P. Hogget et al; 'Preliminary Results with Top Launch 3rd Harmonic X-mode Electron Cyclotron Heating in the TCV tokamak'; Nuc. Fus. 43 (2003) 1353 - 1360

[2] G. Arnoux et al; 'Absorption Properties of X3 Top Launch ECH on TCV'; to be submitted to the Proceeding of EC-13, Niznhy Novgorod, May 2004.

[3] L. Porte et al; 'Third Harmonic X-mode Electron Cyclotron Resonance Heating on TCV using Top Launch'; Proceedings of the 19th IAEA Fusion Energy Conference, Lyon France 14th – 19th October 2002. Paper EX/P5-15

[4] Y. Martin et al; 'Search for Determinism in ELM Time Series in TCV'; PPCF **44** (2002) A373-A382

Results of Integrated Optimization of N=9 Quasi-isodynamic stellarator

V.D. Shafranov[1], W.A. Cooper[2], M.F. Heyn[3], M.Yu. Isaev[1], V.N. Kalyuzhnyj[4], S.V. Kasilov[4], W. Kernbichler[3], M.I. Mikhailov[1], V.V. Nemov[4], C. Nührenberg[5], J. Nührenberg[5], M.A. Samitov[1], A.A. Skovoroda[1], A.A. Subbotin[1], R. Zille[5]

[1] *Russian Research Centre "Kurchatov Institute", Moscow, Russia*
[2] *CRPP, Association Euratom-Confédération Suisse, EPFL, Lausanne, Switzerland*
[3] *Institut für Theoretische Physik, Technische Universität Graz, Graz, Austria*
[4] *IPP, NSC "Kharkov Institute of Physics and Technology", Kharkov, Ukraine*
[5] *Max-Planck-Institut für Plasmaphysik, IPP-EURATOM Association, Germany*

Abstract It has been demonstrated earlier that in quasi-isodynamic (qi) stellarators [1] with poloidally closed contours of the magnetic field strength on the magnetic surfaces good long-time collisionless confinement of α-particles can be achieved, simultaneously with the stability of Mercier- and resistive-modes, for different numbers of system periods (see, e.g. [2-4]). It was shown also, that the effective-ripple factor, $\epsilon^{3/2}$, which characterizes the neoclassical transport in the $1/\nu$ regime, and the structural factor G_b of bootstrap current can be made small in configurations of this type.

It is interesting to find the configuration in which all criteria of the improvement would be satisfied simultaneously. In the present paper preliminary results are presented of an integrated optimization of the $N = 9$ qi configuration.

Introduction As was shown earlier, the quasi-isodynamic configurations with poloidal direction of lines $B=$ constant on magnetic surfaces [1] possess such good properties as improved collisionless confinement of fast particle, small neoclassical transport and small bootstrap current. The value of the stability β limit in the configurations of such type depends on the number of periods and aspect ratio. By numerical optimization it was shown that a tendency exists of increasing β limit with increasing number of periods [2-4]. In the present report preliminary results of an integrated optimization toward quasi-isodynamicity (qi) are presented for a configuration with comparatively large number of periods, $N = 9$. Here the term "integrated" means that the penalty function is in particular weighting fast- particle confinement, stability requirements and the requirement of $\epsilon^{3/2}$ and G_b to be small.

Results of optimization The optimization was carried out on the NEC SX-5 super-computers himiko (Germany) and prometeo (Switzerland) with the VMEC code [5] for equilibrium calculations, the JMC code [6] for the transition to magnetic (Boozer) coordinates and the MCT code [7] for direct calculation of particle drift orbits. In addition, the global-mode stability of the optimized configurations was investigated by the CAS-3D code [8].

Results of initial optimization of particle confinement and local-mode stability

The optimization was performed for a configuration with $< \beta >= 10\%$. In the first step the requirements of improved α-particle confinement and local (Mercier, resistive-interchange and ballooning)-mode stability was imposed. As a result, a configuration was found in which all collisionless α particles started at $1/2$ of the minor plasma radius were confined for a long time (there were no losses during the considered time of 1 sec for power-plant type parameters, $B_0 = 5T, V = 1000m^3$, α-particle energy $3.5MeV$). The

stability investigation by the CAS-3D code has shown that the plasma is stable against global modes up to $< \beta >= 14.5\%$. In contrast to the previously considered $N = 6$ configuration with $< \beta >= 5\%$, a significant improvement of fast-particle confinement does not lead automatically to small effective ripple. The characteristic value of effective ripple was found to be $\epsilon^{3/2} = 2 \cdot 10^{-2}$. A possible cause is that for a large value of β due to the diamagnetic effect and corresponding strong radial dependence of the second adiabatic invariant, $< \mathcal{J} >_\theta = < \oint V_{||} dl >_\theta$, the improvement of fast-particle confinement becomes possible even for a considerable poloidal variation of $\mathcal{J}$.

Results of integrated optimization

To diminish the effective ripple and bootstrap current an additional optimization was performed with a corresponding target function. The $<\beta>$ value was chosen to be 11%.

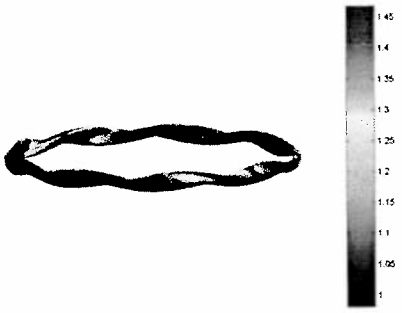

Fig. 1. Boundary magnetic surface of the optimized configuration also showing the magnetic topography. The colors define the range of the magnetic field strength.

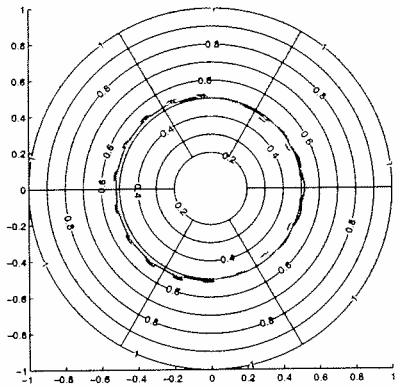

Fig. 2. Particle drift trajectory in the optimized qi configuration. The colors define the range of the particle parallel velocity (red – positive, blue – negative).

Fig. 1 shows the 3D view of the optimized configuration. The colors here define the magnetic field strength on the boundary magnetic surface. It is seen that the plasma column is almost straight in the regions of B extrema. Because of this structure of B, the reflected particles are trapped inside one plasma period, so that the banana size of trapped particles is quite small. Fig. 2 shows the projection of an α-particle drift trajectory in coordinates (s, θ_B), where s is normalized toroidal flux, θ_B poloidal Boozer coordinate. The colors here define the particle parallel velocity (red color corresponds to maximal (positive) value of $V_{||}$ and blue color corresponds to its minimal (negative) value. It is seen that on the outward part of the plasma column the particle with positive $V_{||}$ is shifted to smaller plasma column minor radius while on the inward part the same parallel velocity leads to a particle shift outward. Thus, the bootstrap current in qi configurations appears adjustable to be nearly vanishing.

The behavior of the contours of B at 1/2 of the plasma minor radius is shown in Fig.3. Fig.4 shows the cross-sections of the plasma column in the beginning, 1/4 and 1/2 of a plasma period and the profiles of some flux functions.

The contours of the second adiabatic invariant, that describe the drift of banana centers, are shown in Fig. 5 for a set of particle pitch angles (i.e. for a set of values of $B_{reflect}$). It is seen that these contours are well closed inside the plasma column for all pitch angles. As a consequence, the collisionless confinement of α-particles is good. Fig. 6 shows the α-particle collisionless losses in the optimized configuration as a function

of the time of flight. The particles are started at 2/3 of plasma minor radius (there are no losses of the particles started at 1/2 of the minor radius during the considered time). The calculations are performed for a power-plant type device.

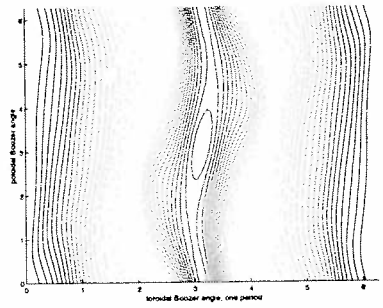

Fig. 3. Contours of B on the magnetic surface with $s = 0.25$ for the optimized configuration.

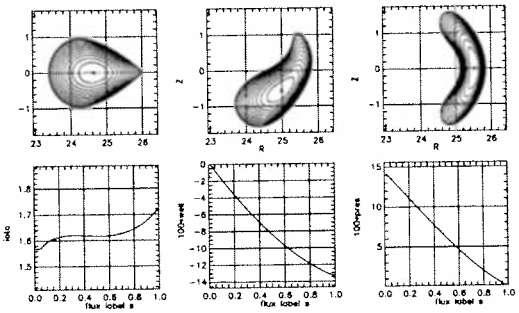

Fig. 4. Cross-sections of optimized configuration for $< \beta >= 11\%$.

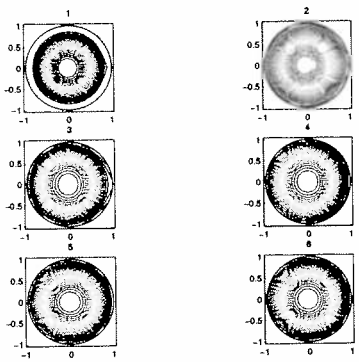

Fig. 5. Contours of the second adiabatic invariant in polar representation ($\sqrt{s}$, poloidal angle θ_B, where s is normalized toriodal flux) for a set of increasing $B_{reflect}$; 1 – corresponds to deeply trapped, 6 – to barely reflected orbits.

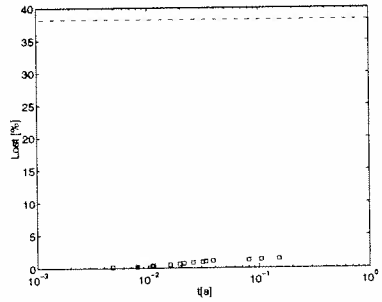

Fig. 6. Collisionless α-particle confinement in the optimized configuration as a function of the time of flight. Particles are started at $s_{start} = 0.44$ (2/3 of plasma minor radius), the dashed line shows the fraction of the reflected particles.

Fig. 7 shows the radial profile of effective ripple in the optimized configuration. The radial dependence of the structural factor of bootstrap current is shown in Fig.8.

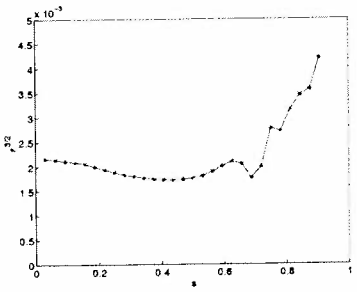

Fig. 7. Radial dependence of effective ripple for optimized configuration.

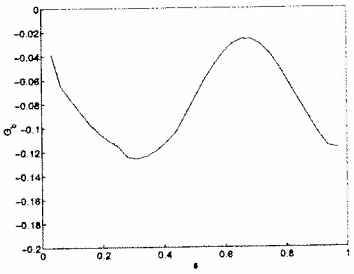

Fig. 8. Radial dependence of structural factor of bootstrap current for optimized configuration.

The stability properties of Mercier and resistive-interchange modes are shown in Fig. 9. Fig. 10 shows the contours of the local-ballooning-mode eigenvalue as a function of free parameters of the ballooning-mode equation, θ_0, ζ_0, for the magnetic surface with $s = 0.6$. Blue color corresponds to negative values (stable), red color corresponds to positive values. It is seen that two line-like regions of instability exist. The stability

of global modes was investigated by the CAS-3D code [8]. Preliminary results (not all families of the disturbances were checked) show that global modes (poloidal node-number is $M = 33$) are stable up to $< \beta >= 10.5\%$.

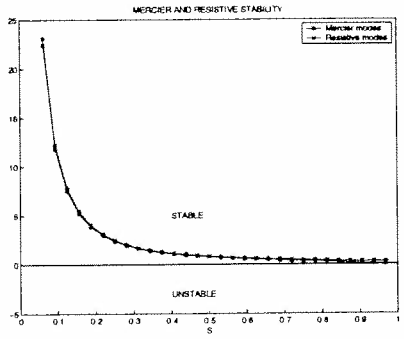

Fig. 9. Mercier and resistive-interchange mode stability of optimized configuration.

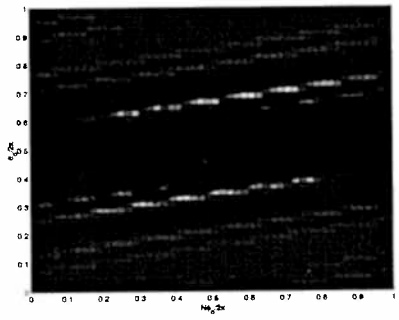

Fig. 10. Contours of ballooning-mode eigenvalue as a function of free parameters of ballooning equation θ_0, ζ_0 for the magnetic surface $s = 0.6$.

Conclusions It is shown by optimization of quasi-isodynamic configurations with comparatively large number of periods and aspect ratio that the simultaneous fulfillment of the conditions of excellent collisionless fast-particle confinement, small neoclassical transport (small effective ripple), small bootstrap current and ideal-mode stability for a comparatively high value of $< \beta >$ can be achieved. It is worth emphasizing that in contrast to other configurations with improved fast-particle confinement, such as quasi-helically or quasi-axially symmetric ones, here the possibility of almost zero bootstrap current can be realized, so that there should be no problem with kink and disruption instabilities.

Acknowledgement This work was supported by the Russian-Germany agreement WTZ-RUS-01/581, by the Russian Federation President program on support of leading scientific schools, Grant No 2024.2003.2, by the Russian Fund for Basic Research, Grant No 03-02-16768, by the Fonds National Suisse de la Recherche Scientifique, Euratom, by the Association EURATOM-OEAW and by the Austrian Academy of Sciences.

References

[1] Gori S., Lotz W. and Nührenberg J. 1996 *Theory of Fusion Plasmas (International School of Plasma Physics)* (Bologna: SIF) p. 335.

[2] Mikhailov M.I., Shafranov V.D., Subbotin A.A et al *Nuclear Fusion* **42** 2002 p. L23.

[3] Shafranov V.D., Cooper W.A., Isaev M.Yu. et al "Optimized Poloidal Pseudosymmetry for Toroidal Systems", report on 30th EPS Conference, St.-Petersburg, Russia, 2003, *ECA Vol.27A, P-4.16.*

[4] M.A. Samitov, W.A. Cooper, M.Yu. Isaev et al, "Quasi-Isodynamic Configuration with Small Number of Periods", Report on Toki Conference, Dec. 2003, Toki, Japan, submitted to Journal of Plasma and Fusion Research SERIES, 2004.

[5] Hirshman S.P. and Betancourt O., J. of Comput. Physics **96** (1991) 99.

[6] Nührenberg J., Zille R., Theory of Fusion Plasmas (Varenna 1987), Editrice Compositori, Bologna (1988) 3.

[7] Fowler R.H., Rome J.A., Lyon J.F., Phys. Fluids **28** (1985) 338.

[8] C. Schwab, *Phys. Fluids B*, **5** (1993) 3195.

Equilibrium and Stability for the ARIES Compact Stellerator Reactor

A.D. Turnbull[1], L.L. Lao[1], W.A. Cooper[2], G.Y. Fu[2], P. Garabedian[3], L.P. Ku[2], and M.C. Zarnstorff[2]

[1]*General Atomics, P.O. Box 85608, San Diego, California 92186-5608, USA*
[2]*Princeton Plasma Physics Laboratory, Princeton, New Jersey, USA*
[3]*Courant Institute, New York University, New York, New York, USA*

Equilibrium and ideal magnetohydrodynamic (MHD) stability studies are reported for Compact Stellarator (ARIES-CS) reactor design equilibria based on a scaled three-period NCSX configuration and a two-period quasi-axisymmetric variant, the MHH2 stellarator. With a stabilizing shell at about twice the minor radius, robustly stable equilibria up to β=6% are achievable. Recent experiments raise questions as to the applicability of linear MHD stability in stellarators since the predicted stability limits appear to be significantly exceeded. A context for interpreting this question, consistent with tokamak experience, is discussed; both the equilibria and nonlinear consequences need to be more carefully considered. Nonlinear stability is analyzed by computing solutions with highly resolved discontinuities to effectively simulate current sheets and islands. This yields β limits in better agreement with measured values.

I. Linear Ideal MHD Stability Limits

A first step in evaluating the prospects for any proposed fusion experiment is to determine reference equilibria and test the linear stability properties. For an equilibrium based on a scaled-up three-period NCSX configuration with β = 4.1% and A = 4.47, the linear MHD stability was determined using the TERPSICHORE [1] code. The stability results for this equilibrium are restricted to a range of external conformal conducting walls between a_w = 1.7 and 2.7 times the minor radius of the plasma. For the wall in this range, the plasma is stable.

A sequence of higher β equilibria was then constructed with the volume, average major radius, average minor radius, and vacuum toroidal field held fixed as β was increased through uniformly scaling the pressure profile. Also, the calculation was a fixed boundary calculation. The major change in the equilibria is that the magnetic axis shifts outward by about 5% as β increases. This sequence was then tested for ideal stability. With a conformal stabilizing shell at twice the plasma minor radius, robustly stable equilibria up to 6% are achievable. The computed growth rates were sensitive to mesh size but the stability boundaries were unchanged.

A two-period variant, the MHH2 stellarator, with good quasi-axisymmetry comparable to that in a tokamak with toroidal ripple, which has some engineering advantages, was also considered. This can be generated by a set of only eight moderately twisted modular coils; a fixed-boundary MHH2 equilibrium was reproduced with β = 4.52%. Figure 1 shows a comparison with the three-field period equilibrium. The main shape difference is the lower

order shaping near $N_{fp}\phi \sim 180$ deg. The rotational transform profiles, however, are very different; for MHH2, the ι profile monotonically decreases over most of the minor radius, increasing again only near the edge. For the three field period equilibrium, the converse is true.

A series of increasing β MHH2 equilibria was then constructed with $\langle\beta\rangle = 4.52\%$, 5.71%, and 6.92% as for the previous case. The ι profile was adjusted to force the average current density to vanish as β increases; the bootstrap current was not self consistently calculated. These equilibria were tested for ideal MHD stability. The Mercier criterion indicates stability at all surfaces up to β=5%. The TERPSICHORE studies find the growth rates are small and insensitive to wall position. They remain small up to β=6.9% indicating marginal stability to free boundary modes.

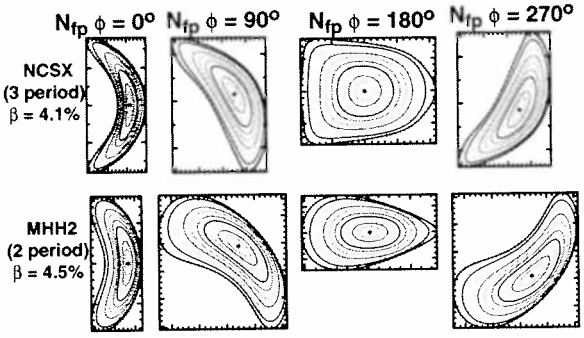

Fig. 1. Comparison of the three- and two-period candidate equilibria at four toroidal cross sections.

II. Stellarator β Limits

W7-AS and LHD have exceeded predicted β limits by significant margins; the calculated local limits of less than 2% were exceeded, with β reaching above 3% in both devices. Stellarator designs that are based on optimizing against linear ideal MHD stability are therefore questionable. There are two possible resolutions based on experience with tokamak stability limits. First, the discharge equilibria are not necessarily those used in the stability predictions. Second, the nonlinear consequences of linearly unstable ideal modes need to be understood; heuristically, internal modes surrounded by a fairly robustly stable outer shell can be expected to be benign and not limit β directly.

A. Equilibrium Questions. Experience with tokamaks has shown in recent years that the ι (or q) profile is not necessarily what theoretical arguments suggest it should be. It is important to use actual reconstructed discharge equilibria and test the sensitivity of stability predictions to profile and boundary variations within the experimental errors [2]. Reducing these errors is crucial to obtaining unambiguous predictions. Critical parameters are the last closed flux surface, the q and pressure gradient profiles, and the bootstrap current, especially at the edge. Considerable success has been achieved in demonstrating the quantitative validity of ideal limits, mode structures and growth rates, when these are properly accounted for [2].

For stellarators, experimental measurements of the pressure and ι profiles at finite β, like those in large tokamaks, are needed to pin down the apparent violation of predicted stability limits. For example, the bootstrap current is often assumed negligible but may not necessarily be so. Even the nested surfaces assumption may not be the case in stellarator discharges.

B. Nonlinear Stability Consequences. Experience with tokamaks has also shown that some predicted ideal limits can be violated but that the nonlinear consequences do not

directly limit β or lead to disruptions. Examples are sawteeth and ELMs. Also, local Mercier, and even ballooning stability, are generally considered ignorable when unstable only over a small region. This is fairly well understood intuitively but the same understanding is not yet available for stellarators.

For stellarators, there are good experimental and theoretical justifications for ignoring local stability. For global modes, the nonlinear consequences need to be examined on a case-by-case basis. Nonlinear stability can be analyzed by computing weak solutions for 3-D equilibria, with discontinuities to simulate current sheets and island. The key is to accurately resolve the discontinuities by ensuring that the ideal equations are in conservative form.

The MHD equations describing force balance can be put in conservation form: $\nabla\cdot \mathbf{T} = 0$, $\nabla\cdot \mathbf{B} = 0$ where the Maxwell stress tensor $\mathbf{T} = \mathbf{B}\,\mathbf{B} - (B^2/2 + p)\,\mathbf{I}$. Finite difference equations that respect the conservation form telescope into an approximate statement of force balance over the boundary when summed over a test volume: $\iint \mathbf{T}\cdot d\mathbf{S} = 0$. In a simplified example using Burgers equation as a model problem for an RFP in a slab, $x \in (1,+1)$: $2\Psi_x \Psi_{xx} = \left(\Psi_x^2\right)_x = \eta\Psi_{xxx}$, subject to boundary conditions $\Psi(-1) = \Psi(-1) = 0$, and $\Psi_x(-1) = 0$, a conservative difference scheme: $(\Psi_{n+1} - \Psi_n)^2 - (\Psi_n - \Psi_{n-1})^2 = \eta(\Psi_{n+2} - 3\Psi_{n+1} + 3\Psi_n - \Psi_{n-1})$ imposes force balance in the limit where $\eta = 0$, across the discontinuity at $x = 0$, so that the solution reduces to $\Psi = 1 - |x|$. However, a non- conservative finite difference scheme defined with an additional diffusive term, $\varepsilon(\Psi_{n+1} - 2\Psi_n + \Psi_{n-1})^2$, added to the left hand side, diverges when η is much smaller than the mesh size $\varepsilon \neq 0$. When $\eta \sim \varepsilon$, force balance is not maintained by a non-conservative scheme; this is exhibited numerically by inequality of the slopes on the two sides of the limiting solution $\Psi = 1 - |x|$. which characterize the magnetic field on opposite sides of a current sheet and simulates a chain of magnetic islands.

The NSTAB [4] equilibrium and stability code applies the MHD variational principle to compute weak solutions of the conservation form of the dynamical equations. Solutions are represented in terms of Clebsch Potentials. The code computes fixed boundary 3-D equilibria and nonlinear stability is tested by applying a mountain-pass theorem that requires a search for multiple or bifurcated equilibria. The code utilizes a finite difference scheme based on the above discussion that captures discontinuities with unusually fine resolution.

III. Discussion

It is significant that both the ARIES-CS equilibria have linear ideal MHD β limits above 5% since the evidence from experiments suggests that these may be lower limits. To resolve the question of the meaning of these limits requires high quality equilibrium reconstructions and stability calculations using the experimental equilibria to determine which limits are really being violated. Then, robust nonlinear calculations are needed to obtain an intuitive feel for the consequences of the instabilities predicted. This is not yet at hand and consequently, it is not clear at present how valuable linear MHD stability predictions using nested flux sur-

face equilibria really are; they might, in fact, be quite misleading. Free boundary non-nested equilibria, and/or nonlinear stability studies may be needed to obtain meaningful predictions.

The existence of a nested flux surface equilibrium can be considered as either an equilibrium problem or a stability problem; unstable equilibria with nested surfaces will evolve to non-nested surfaces with lower energy if physically possible. Equilibrium codes can therefore be considered stability codes, since an equilibrium computed under certain constraints must be stable unless those numerically imposed constraints can be avoided by a physically valid motion. NSTAB makes use of this to determine nonlinear stability when bifurcated equilibria exist. The code does impose nested flux surfaces but permits well-resolved discontinuities to simulate islands. The major constraint imposed, is the fixed boundary; NSTAB can only guarantee guarantee stability to internal global modes.

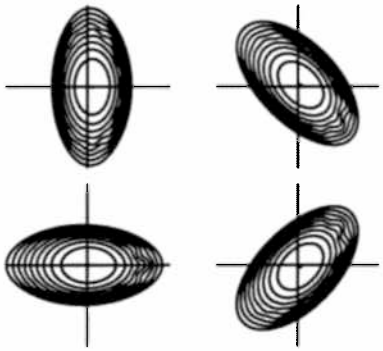

Fig. 2. Poincare map of the flux surfaces at four cross sections over one field period of a bifurcated LHD equilibrium at $\beta = 0.04$. For a broad pressure profile $p = p_0(1 - s^2)$, this solution developed a ballooning mode but remained marginally stable.

From a theoretical and numerical point of view, the first step then in resolving the questions formulated here, is to compare linear and nonlinear predictions and to compare both against experiments. The nonlinear stability test in NSTAB yields beta limits that are in substantial agreement with measured values; the calculations show that LHD is marginally stable at the largest values of β achieved and there is similar agreement for W7-AS.

IV. Conclusions

This work shows that one can obtain linear ideal MHD β limits for a compact stellarator reactor of order of 6%. Future cork will examine the sensitivity of the linear β limits for the two configurations to profile and shape variations. These are linear stability limits and there are questions as to their relevance. In the longer term, these questions need to be resolved by examining the stability of actual reconstructed discharge equilibria with measured ι and pressure, and the sensitivity to profile and boundary variations. Additional discrepancies should be resolved by nonlinear studies and routine comparisons with observations. This will entail repeating the nonlinear calculations for the ARIES-CS equilibria by searching for bifurcated equilibria as described in Section II.B. The correlation of computations with observations was, in fact, exploited to design the two field period MHH2 stellarator.

This work has been supported by the U.S.Department of Energy under DE-AC03-98ER54411, DE-AC02-76CH03073, and DE- FG02-86ER53223.

[1] A. Ardelea, W.A. Cooper, and L. Villard, Plasma Phys. Control. Fusion **40** (1998) 1679.

[2] A.D. Turnbull, D.P. Brennan, M.S. Chu, *et al.*, Nucl. Fusion **42** (2002) 917.

[3] P.R. Garabedian, Plasma Phys. Control. Fusion **39** (1997) B129.

Shear, temperature gradient and collisionality dependences of particle pinches in JET

H. Weisen, A. Zabolotsky, C. Giroud[1], H. Leggate[1], K.-D. Zastrow[1], C. Angioni[2], J. Weiland[3], X. Garbet[4], L. Zabeo[4], D. Mazon[4], I. Furno[5] and JET-EFDA contributors

Centre de Recherches en Physique des Plasmas, Association EURATOM - Confédération Suisse, EPFL, 1015 Lausanne, Switzerland
[1)]UKAEA, Abingdon, UK [2)]IPP Garching, Germany [3)]Chalmers University, Göteborg, Sweden [4)]CEA DRFC, Cadarache, France [5)]LANL, Los Alamos, USA

Abstract: The peakedness of density profiles in L-modes and in H-modes exhibits remarkably different behaviour. The former scales with overall plasma shear in accordance with Turbulent EquiPartition (TEP) theory ($n_{e0}/\langle n_e\rangle \sim 1.5 l_i$), independently of collisionality. On the other hand, peaking in H-modes depends on collisionality, with $n_{e0}/\langle n_e\rangle$ increasing from ~ 1.2 at $\nu_{eff}=1$ to $n_{e0}/\langle n_e\rangle \sim 1.6$ at the collisionality of the ITER reference H-mode, $\nu_{eff}\approx 0.1$. H-mode density profiles show no shear dependence, except for $\nu_{eff}\leq 0.2$. Evidence for L_{Te}, L_{Ti} or ρ^* dependences has been obtained neither in L nor in H-modes. Carbon density profiles from CXS are always less peaked than electron density profiles.

1. Experimental evidence

The peakedness of the density profile in source-free MHD-quiescent L-mode plasmas with off-axis lower hybrid current drive (LHCD) at power levels up to 3.6MW decreases with decreasing peaking of the current profile. For these discharges, which include normal and reversed magnetic shear plasmas (as determined by polarimetry), the relationship can be expressed as $n_{e0}/\langle n_e\rangle \cong 1.6 l_i$, where l_i is the normalised internal inductance (fig.1). These experiments, which were previously reported in [1], have been reanalysed with density inversions using the more accurate SVD-I method, which adopts as base functions the *topos* provided by an biorthogonal decomposition of a sequence of ~50 Thomson scattering profiles [2]. Density profiles remain monotonically peaked at negative shear. The density profiles remain peaked at zero loop voltage and negligible core particle source, as determined using the neutral transport code KN1D [3], confirming investigations in fully current driven discharges in Tore Supra [4] and TCV [5]. The peaking of the temperature profiles and of the current profiles are largely uncorrelated in this dataset, allowing an experimental distinction between their effects on the density profile. No dependence on L_{Te} was found. These discharges have

been analysed with respect to microinstabilities with the gyrokinetic code GS2 [6]. The main result is that the sign of the mode frequency is very sensitive to input parameters. We interpret this as an indication that the discharges are in a mixed ITG/TEM regime, where thermodiffusion is expected to be weak [7]. Fig. 2 shows that the peaking factor is independent of the theoretically important effective collisionality defined as $\nu_{eff} = \nu^*_{ei}/\omega_{De} \sim 3(m_i/m_e)^{1/2}\varepsilon^{3/2}\nu^*_{ei}/q$ and evaluated at mid-radius, assuming $k_\theta\rho=1/3$. The figure also shows that the carbon density profile from charge exchange spectroscopy (CXS) is significantly less peaked than the electron density profile. We have extended the study to a variety of NBI and ICRH L-modes with a similar results, $n_{e0}/\langle n_e\rangle \approx 1.4 l_i$ and no discernible collisionality dependence.

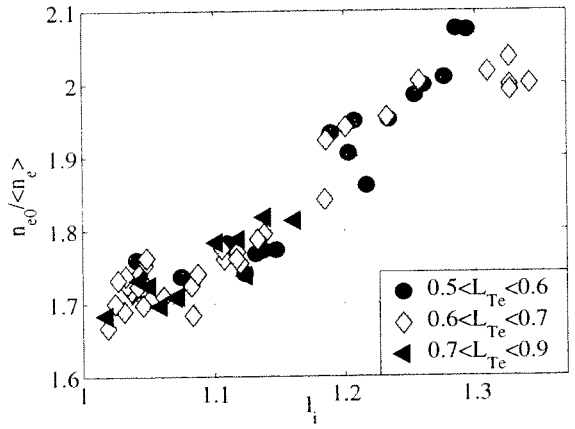

Fig. 1. Density peaking in LHCD L-modes versus internal inductance, resolved by electron temperature gradient length.

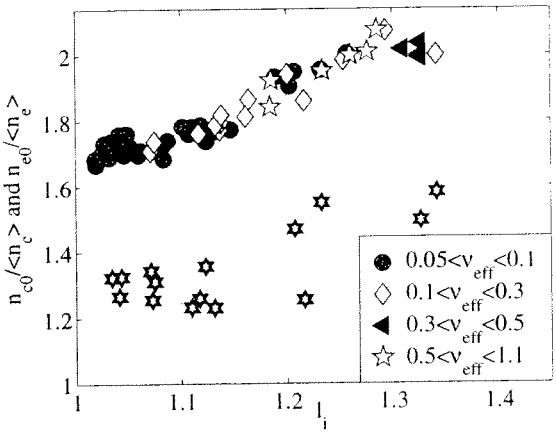

Fig. 2. Same, resolved by effective collisionality at r/a=0.5. In black, peaking factor of carbon impurities.

The behaviour of H-modes is in stark contrast to the above, fig.3, with a clear collisionality dependence and no l_i dependence, except for $\nu_{eff} \leq 0.2$. There is also no dependence of peaking on $\langle n_e\rangle$, nor on P_{icrh}/P_{aux}, P_{nbi}/P_{aux}, β_N, L_{Te}, or L_{Ti}. Fig.3 is a confirmation of an earlier observation on ASDEX-upgrade [8]. The collisionalities obtained on JET extend to below those expected for the ITER reference H-mode. The peaking is slightly higher (by ~0.1) at $\nu_{eff} \sim 0.2$ in JET than in [8] when the evaluation of ν_{eff} is based on a flat Z_{eff} derived from visible Bremstrahlung. JET and ASDEX results are however brought into agreement when using the lower and hollow Z_{eff} profiles measured by CXS. The agreement suggests an extrapolation to ITER. Since both β and shear in ITER are within the parameter range of current experiments, such an extrapolation will depend on the scaling with ρ^*. The data in Fig. 4 are resolved by ρ^*, showing that for any ν_{eff} interval considered, there is no significant ρ^* dependence other than due to ν_{eff}. In Fig.5 we plot the data in terms of $R/L_{ne} = R\nabla n_e/n_e$ at

mid-radius, resolved by R/L_{Te}, showing that there is also no direct evidence for thermodiffusion. Hence, assuming otherwise similar (non-ignited) conditions, we expect for ITER $n_{e0}/\langle n_e\rangle \approx 1.6\pm0.2$ at $\nu_{eff}\approx 0.1$, corresponding to $R/L_{ne} \cong 4 \mp 1.3$ at mid-radius.

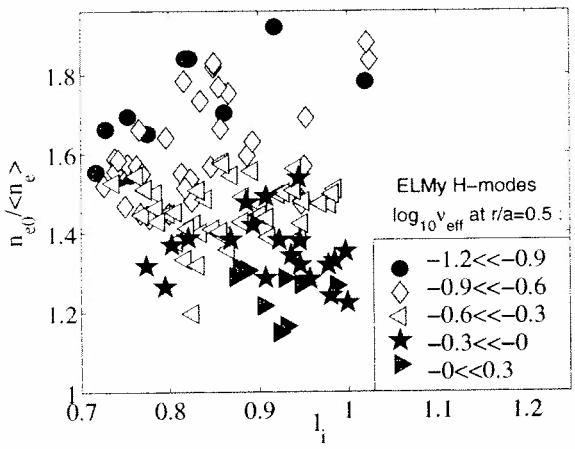

Fig. 3 Peaking factor in H-mode versus ν_{eff}. Symbols: classes of internal inductance.

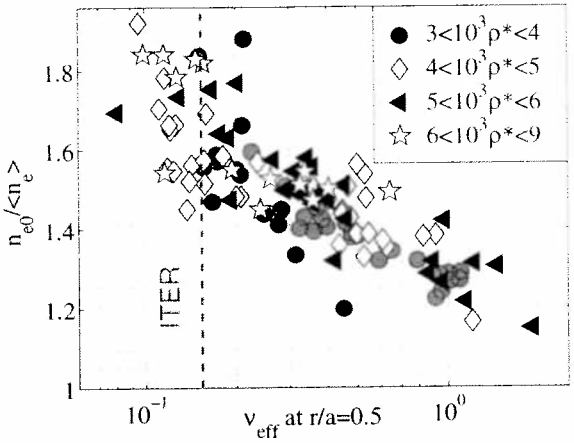

Fig. 4. Same, resolved by normalised Larmor radius ρ^*. Vertical line : ITER reference H-mode.

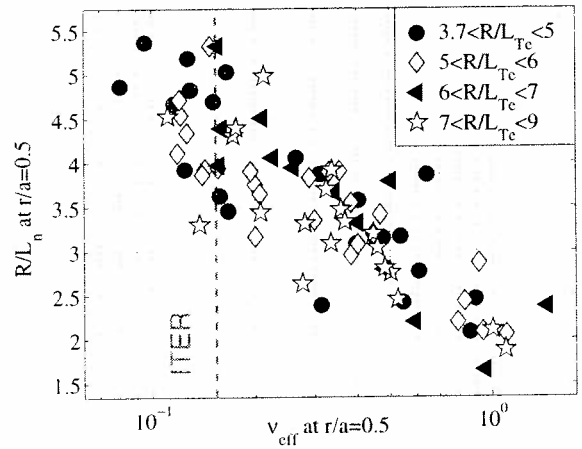

Fig. 5 Normalised density gradient at r/a=0.5, resolved by temperature gradient (H-mode).

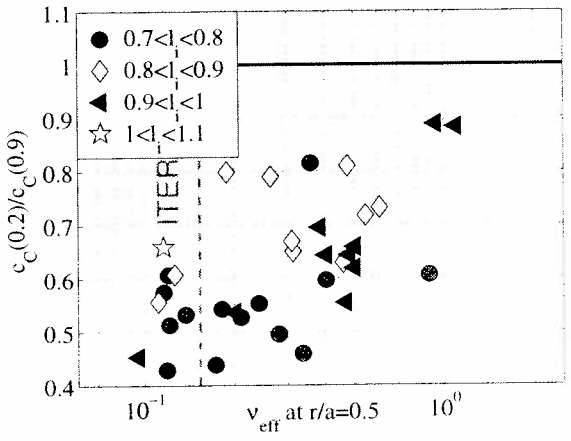

Fig. 6 Ratio of carbon concentrations near the edge and in the plasma core (H-mode).

2. Discussion.

Such strong peaking raises concerns about impurity accumulation in the core. CXS measurements show, that for light impurities, this is not the case. Carbon density profiles are close to flat at any collisionality in H-mode, resulting, for the lowest collisionalities, in hollow Z_{eff} profiles, Fig. 6. This may be due to neoclassical ion temperature gradient screening, as well as to anomalous effects. Simulations using the Weiland model show that an initially flat Z_{eff} profile in H-mode evolves into a hollow one, purely as an effect of anomalous transport. However the issue of heavy impurities will require further investigation.

In Fig.7 we plot the cumulated, normalised number of particles N, versus the poloidal

flux for the LHCD L-modes and for H-modes. Normal shear L-modes (black) and low collisionality H-modes (red and yellow) are remarkably close to the TEP behaviour expected from purely diffusive transport of trapped electrons in poloidal flux space, i.e $dN/d\Psi$ constant over most of the cross section [9]. Higher collisionality H-modes, reversed shear L-modes and plasmas with strong central electron heating ([10], not in fig.7) depart from TEP.

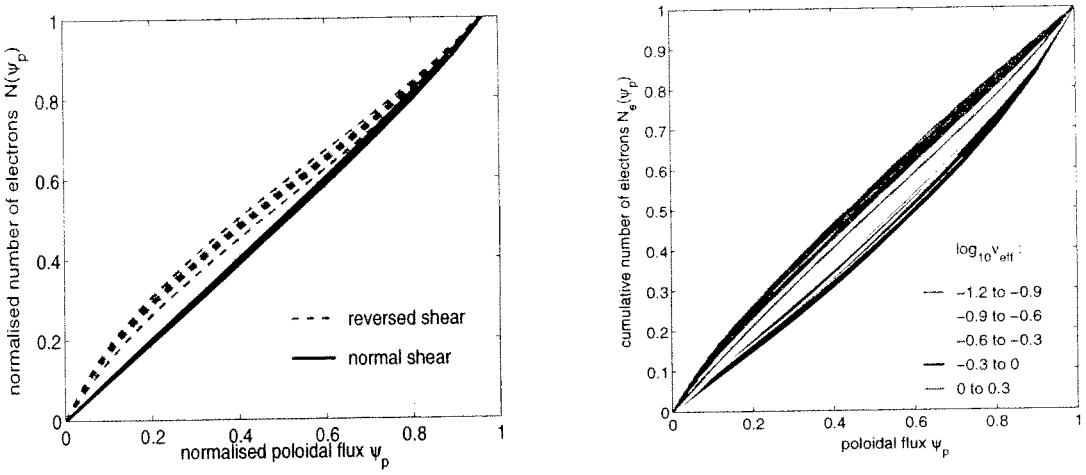

Fig. 7 Comparison of density profiles with TEP. left: LHCD L-modes. right: H-modes.

The density profile resulting from a combination of trapped and passing particle transport was discussed in [9]. We conjecture that a density profile directly reflecting trapped electron transport may also be consistent with a virtual absence of anomalous passing electron transport, consistently with the TEP assumption of conservation of the second invariant (enclosed toroidal flux for passing particles), i.e. passing electrons arriving at any location would do so by collisional detrapping only. The absence of l_i dependence for ν_{eff} in H-modes at $\nu_{eff}>0.2$ and the ν_{eff} independence of peaking in L-modes is a puzzling paradox, hinting at basic differences in the underlying turbulence. A plausible interpretation may be that L-modes are near the ITG/TEM stability boundary, with little or no thermodiffusion. Plasmas with density flattening due to central electron heating may be driven well into the TEM domain, experiencing outward thermodiffusion [7], whilst H-modes at $\nu_{eff}>0.2$ are in the ITG domain [8]. H-modes at $\nu_{eff}<0.2$ may be peaked enough to destabilise TEM. If so, $n_{e0}/\langle n_e\rangle$ in ITER may be reduced by the strong α heating, to below the level observed in JET at $\nu_{eff}\sim 0.1$.

References

[1] H. Weisen et al, *PPCF* **46** (2004) 751
[2] I. Furno et al, (2004), *submitted to PPCF*
[3] B. Labombard **PSFC-RR-01-03** (2001)
[4] G.T. Hoang, et al, *PRL* **90** (2003) 155002
[5] A. Zabolotsky, et al, *PPCF* **45** (2003) 735
[6] M. Kotschenreuther et al, *Comput. Phys. Commun.* **88** (1995) 128
[7] C. Angioni et al, *NF* **44** (2004) 827
[8] C. Angioni et al, *PRL* **90** (2003) 205003
[9] D.R. Baker et al, *NF* **40** (2000) 1003
[10] X. Garbet et al, *EPS* **31** (2004) invited

MHD activity in EC-heated TCV plasmas with eITBs

G. Zhuang, A. Scarabosio, R. Behn, Y. Camenen, T.P. Goodman, M.A. Henderson, I. Klimanov, A. Martynov, O. Sauter, H. Weisen and TCV team
Centre de Recherches en Physique des Plasmas,
Association EURATOM-Confédération Suisse, EPFL, CH-1015 Lausanne, Switzerland

Scenarios leading to the formation of internal transport barriers (ITBs) are of interest for tokamak operation since they permit to obtain large bootstrap current fractions and considerable improvement in energy confinement [1]. In the case of dominating electron heating - e.g. by ECRH - the electron ITBs (eITBs) are influenced by the shape of the current density profile and the formation of q-profiles with reversed shear. In the TCV tokamak, combined application of ECH and ECCD (using up to six gyrotrons at 82.7GHz, 0.5MW each) has been used to form eITBs and improvements in energy confinement up to a factor of 6 above RLW scaling have been obtained [2]. However, current profile shaping and strong additional heating may lead to MHD activity with important consequences on performance and steady-state operation. During ITB experiments on TCV under various conditions, several types of MHD activities have been observed. In the following, their basic features will be described and the influence on plasma performance will be discussed.

For the studies presented here the MHD activity has been measured using sets of magnetic probes to record magnetic field perturbations and sets of detector arrays to record the plasma emission in the soft X-ray range (SXR). The magnetic probes are arranged in a toroidal array (16 probes) and a poloidal array (38 probes) permitting us to identify toroidal and poloidal mode numbers up to n=4 and m=8, respectively. The viewing chords of the X-ray detectors cover the poloidal cross section and permit tomographic reconstruction of the emissivity profiles. The signals from fans of chords have been analyzed to identify MHD activity in the central region of the plasma.

During eITB scenarios on TCV two basic types of MHD activities have been observed: tearing modes (TM) and kink-like modes at low m/n rational q-surfaces. The latter show the signature of periodic relaxation oscillations (PROs) with sawtooth-like features in the SXR signals. The tearing modes cause slowly oscillating perturbations (3-6kHz on TCV) of the fields measured by the magnetic probes.

In general, tearing modes (TMs) are associated with the appearance of magnetic islands at rational q-surfaces and are driven by current and pressure gradients. In our cases, the tearing modes are localized near q=m/n=2/1 and/or 3/1 surfaces outside the eITB in the region of positive magnetic shear. At the mode onset the values of β_N range from 0.6 to 1.4

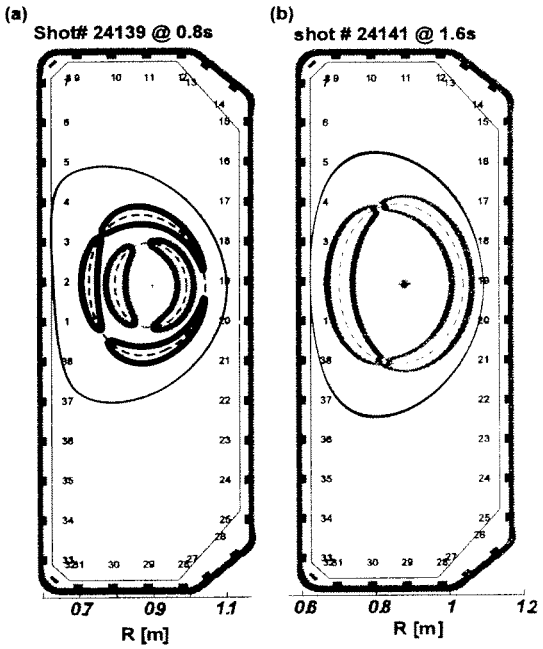

Fig.1 Magnetic islands reconstructed from the magnetic perturbation data. (a) m/n= 3/1 (blue) and 2/1 (red) modes (coupled); (b) single 2/1 (red) mode.

and the collisionality ν_{e^*} varies from 0.003 to 0.01. Neither the double tearing mode nor the 3/2 mode have been observed. The magnetic islands as shown in Fig. 1 have been reconstructed from magnetic perturbation measurements using a model described in [3]. TCV #24139 (Fig.1a) is an example of a case where a 3/1 mode coexists with a 2/1 mode and both modes are coupled and rotate together, while in #24141 (Fig.1b) only the 2/1 island is present. The poloidal mode number m and the width of the magnetic island have been obtained from analysis of SXR data. The results from magnetic signals and SXR emissivity are in reasonable agreement.

The evolution of the saturated island size for the 3/1 and 2/1 modes respectively, is shown in Fig. 2. The island width of the 3/1 mode $w_{3/1}$ in #24139 increased during the current ramp up although β_p decreased. This implies the bootstrap current contribution to the mode is not important. In #24141, the width of the 2/1 mode $w_{2/1}$ changes in proportion to β_p (see. Fig. 2b). This linear dependence is expected for a typical neoclassical tearing mode (NTM). Detailed investigations showed that this 2/1 mode develops from a seed island, this does not seem to be the case for the 3/1 mode in #24139. The growth rate and saturation of the 3/1 mode island widths for #24139 have been calculated using the Rutherford equation in its form for classical TMs. It is found that the measured growth time scale τ_{tear} ~ 3ms would lead to an unrealistic value of the instability parameter ($\Delta' r_s$ ~75). Obviously, pure resistive tearing mode theory is not sufficient to explain this behaviour and mode coupling or other effects have to be included in the simulation to match the experimental time scale.

The influence on global confinement caused by the tearing mode is shown in Fig. 3 for # 24139. As the coupled 3/1 and 2/1 modes build up at 0.556s (see Fig. 3b), the global confinement (referred to RLW scaling) degrades significantly from 3.5 to 2.5, the eITB strength (identified by ρ_{*T}, according to

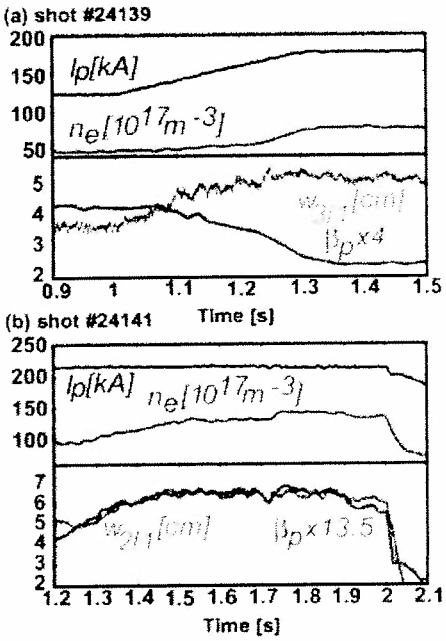

Fig. 2 Evolution of plasma current I_p, averaged density n_e, saturated magnetic island width $w_{m/n}$ and poloidal beta β_p for shots 24139 (a) and 24141 (b), respectively.

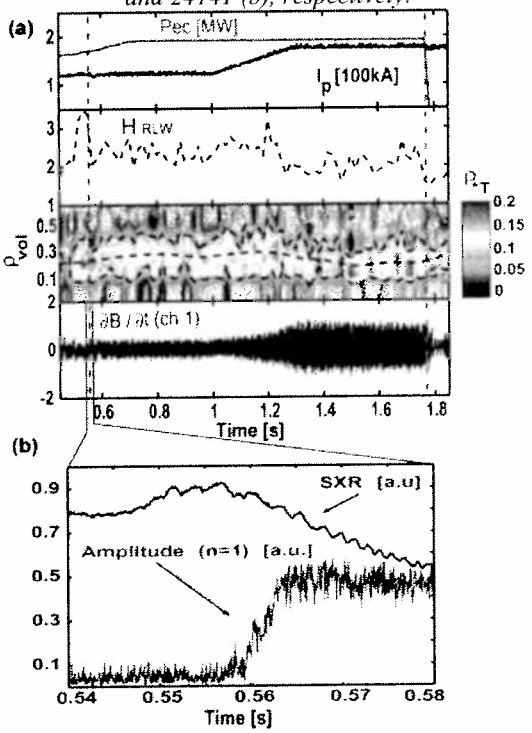

Fig. 3 (a) Evolution of I_p(blue), P_{ec} (red), the confinement H_{RLW}, the eITB strength ρ_{*T} (contour plot), and the mode amplitude (magnetic probe) for #24139; (b) The SXR signals and mode amplitude at time of drop in H_{RLW} (0.556s).

Tresset [4]) decreases but the radius of the weaken eITB stays at the same location even in the ramp-up phase of heating power. The growth of the mode amplitude is correlated with a gradual decrease of the SXR signal, indicating that the presence of the TMs is responsible for the degradation of the ITB and the energy confinement. As the mode amplitude increases further, the averaged H_{RLW} drops from 2.5 to 2 and the ρ_v radius of ITB shrinks from 0.3 to 0.2, which means that the high confinement phase is lost.

Apart from tearing modes, fast collapse events and PROs have been observed. The PROs show sawtooth-like signature with an inversion radius located close to the q=2 magnetic surface and a longer period than that of ordinary sawteeth. The PROs have been identified as kink modes driven by high local pressure gradients or by a global beta limit.

A paradigm of PROs is shown in Fig.4 for # 24696, and compared with a quiescent case (#24698). Both shots have quite similar plasma parameters except for the higher density and lower additional heating power of #24698. As seen from the SXR signals, the MHD activity in #24696 started at t=0.81s with a fast crash event (2/1 mode) which stabilized at 0.88s. Then PROs appeared with regular oscillations at a period of 16ms and stayed until the central EC heating power was turned off. Fig.4 shows that the degradation of the global confinement and the influence on the eITB introduced by PROs are much less pronounced than in the case of a TM. The averaged H_{RLW} of #24696 is ~2.5 and almost the same as that of #24698 (~2.6).

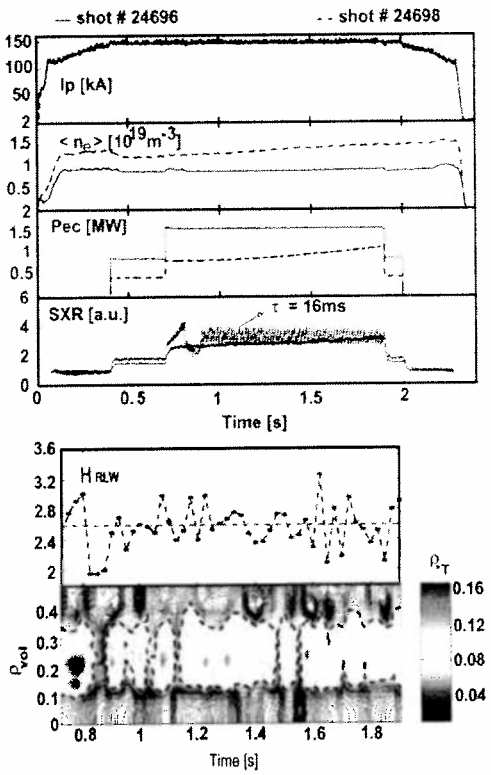

Fig. 4 ***Top****: PROs as seen in SXR signal for shot # 24696, in comparison with quiescent case shot #24698.* ***Bottom****: The confinement and eITB behaviour during the phase with PROs of shot #24696.*

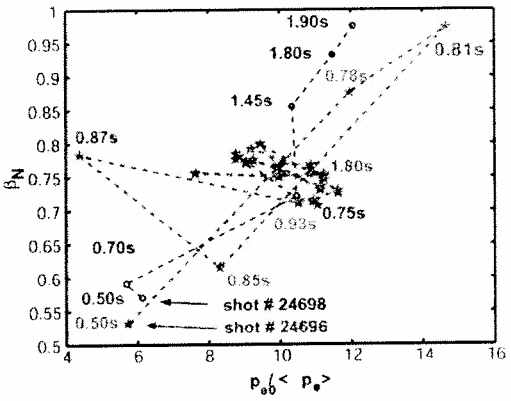

Fig. 5, Evolution of the experimental β_N and pressure peaking factor for shots #24696 (blue) and #24698 (red), respectively. In shot #24696, at 0.81s, the mode occurred leading to a rapid drop in β_N and peaking factor.

The evolution of the experimental β_N and pressure peaking factors ($P_{e0}/<P_e>$), as shown in Fig. 5, shows the difference between both shots. The peaking factor and β_N start to increase when the heating power is turned on. At 0.81s the peaking factor of #24696 reaches an extremely high value ~15 and causes a rapid collapse in the pressure

profile and a large decrease in β_N. Due to the lower EC power the peaking factor of #24698 never reaches this limit.

For #24696 central counter ECCD is preceded by off-axis ECH, which results in broad temperature (T_e) profiles. However, after the injection of EC power (0.7MW) into the centre, T_e and pressure (P_e) become strongly peaked. The large pressure gradients, together with a broadened q profile (low magnetic shear), destabilize the ideal MHD modes. To compare and illustrate the effects of different heating scenarios, another example (TCV #23612) with different timing and deposition location of the EC power has been chosen (see fig.6). In case of #23612 off-axis ECH is deposited slightly inside the q=2 surface. At the same time (0.4s) central counter-ECCD begins with a power ramp reaching full power of 1.5MW at 0.7s. The T_e profiles evolve slowly and lead to a change of the current density profile on a resistive time scale. This can be inferred from the change in plasma internal inductance l_i. Increasing the central power injection causes the central T_e to rise, but the peaking of the pressure profiles does not exceed 12. During the whole heating phase a small amplitude mode is present, but does not degrade the performance, and the radius of the ITB stays near ρ_v=0.35. Therefore, good confinement (H_{RLW} ~ 4-4.5) is obtained at a rather high β_N ~ 1.4 (as indicated in Fig. 7).

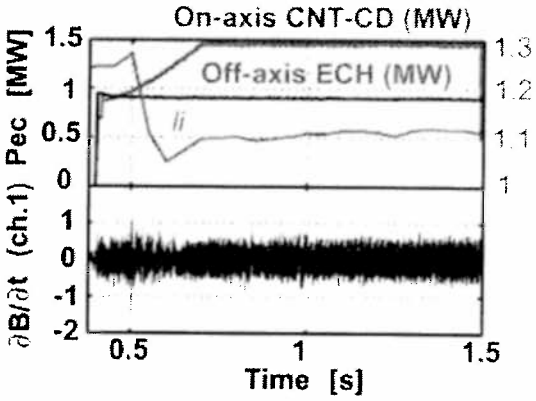

Fig. 6 The timing of EC power injection, plasma inductance l_i and MHD activities for shots 23612.

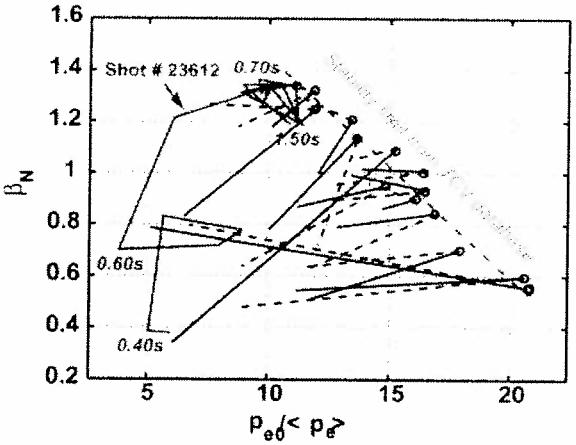

Fig. 7 The evolution of β_N and pressure profile peaking factors for a series of shots from the TCV database. In red the evolution for #23612 with the highest β_N. The symbol ('o') marks the onset of the MHD activity at the largest $P_{e0}/<P_e>$.
solid line: phase without MHD activity just before onset (~50ms);
dashed line: phase with MHD activity after onset (~50ms);
Magenta dashed-dotted line: experimental stability limit.

In general, the achievable β_N in tokamaks is limited by MHD instabilities driven by pressure gradients. As can be seen from these examples of EC heated plasmas with ITBs, attempting to reach higher β_N by increasing the heating power will not be successful unless too strong peaking of the pressure profiles can be avoided (see Fig. 7). Careful optimisations of EC power level and deposition location are necessary to achieve this goal.

[1] J.W. Connor, et al, *Nucl. Fusion* 44 (2004) R1-R49
[2] R. Behn, et al, *Proc. 30th EPS conf. On controlled Fusion and plasma Physics*, St. Petersburg, 2003, P3.208
[3] H. Reimerdes, Ph. D. thesis, *MHD stability limits in the TCV tokamak*, 2001, EPFL, Lausanne, Switzerland.
[4] G. Tresset, et al, *Nucl. Fusion* 42(2002) 520

This work was partly supported by the Swiss National Science Foundation.